UCLouvain

FACULTE DES SCIENCES

Faculté des sciences

Development of solid polymer electrolytes based on dioxazaborocane vitrimers

Author: Thibault Pecheur

Supervisor: Pr. Charles-André Fustin

Readers: Pr. Evelyne van Ruymbeke

Pr. Jean-François Gohy

Pr. Alexandru Vlad

Academic year 2025-2026

Master [120] en science chimique, à finalité approfondie

Acknowledgments

First of all, I would like to sincerely thank Professor Charles-André Fustin for welcoming me into his research group. Thank you for your guidance, scientific advice, and for taking the time to review and correct this thesis.

I would also like to warmly thank my supervisor, Swetha Karingal Veedu. Thank you for dedicating part of your PhD time to introducing me to this research topic. Your availability, patience, advice, and support throughout this project were greatly appreciated.

I am also grateful to the members of my jury, Professors Evelyne van Ruymbeke, Jean-François Gohy, and Alexandru Vlad, for taking the time to read and evaluate this master thesis.

My sincere thanks also go to Alain Jancart for the NMR training, Pascal Van Velthem for the thermal analysis training, and Naïma Sallem for the rheology training. Their expertise and willingness to share their knowledge greatly contributed to this work.

I would also like to thank Oriane Froment for her help with conductivity measurements and Alexandru Boborodea for his valuable advice on rheology.

Finally, I would like to thank all the members of B2: Fabio, Charlène, Garance, Alban, Jihad, Alvaro, Arya, Matteo, Lobnan, Zakariae, Yinghui, Zhenni, Qing, and Kejie. Thank you for the discussions, advice, and for creating a welcoming and enjoyable working environment.

Abstract

The increasing demand for safer, more sustainable, and higher-performance energy storage systems has driven the development of solid-state batteries. In this context, solid polymer electrolytes represent a promising alternative to conventional liquid electrolytes, particularly for lithium metal batteries. However, achieving a suitable balance between ionic conductivity, mechanical properties and safety remains a major challenge. Vitrimers, a class of covalent adaptable networks capable of undergoing bond-exchange reactions while maintaining their crosslinked structure, offer an attractive strategy for overcoming these limitations.

This work investigates the development of vitrimer-based solid polymer electrolytes using dioxazaborocane dynamic boronic ester chemistry. PEGMA-based networks containing dynamic crosslinkers, with or without dioxazaborocane dangling groups, were synthesized by UV-initiated free-radical photopolymerization. The materials were characterized through rheological and electrochemical measurements to evaluate their suitability as solid vitrimer electrolytes.

The synthesized networks exhibited typical vitrimer characteristics, including stress relaxation, temperature-dependent network rearrangement, and self-healing behavior. The influence of network composition and lithium salt incorporation on both the dynamic properties and ionic transport was investigated. Promising ionic conductivities were obtained, with $8.1*10^{-5}$ $S.cm^{-1}$ at 60 °C, placing these materials within the upper range commonly reported for vitrimer electrolytes.

Overall, the developed dioxazaborocane-based vitrimer electrolytes showed promising properties, combining vitrimer behavior, thermal stability, self-healing capability, and competitive ionic conductivity. These results highlight their potential as solid polymer electrolytes for lithium batteries.

Table of contents

List of figures

List of tables and equations

List of abbreviations

Abbreviation	Definition
a_T	Horizontal shift factor
CANs	Covalent adaptable networks
DB	Dioxaborolane
DMF	Dimethylformamide
DSC	Differential scanning calorimetry
DZ	Dioxazaborocane
EIS	Electrochemical impedance spectroscopy
EO	Ethylene oxide
EVs	Electric vehicles
FTIR	Fourier transform infrared spectroscopy
G'	Storage modulus
G''	Loss modulus
GPC	Gel permeation chromatography
LMP	Lithium metal polymer
LIBs	Lithium-ion batteries
Li-ion	Lithium-ion
$LiBF_4$	Lithium tetrafluoroborate
$LiPF_6$	Lithium hexafluorophosphate
LITFSI	Lithium bis(trifluoromethanesulfonyl)imide
LMB	Lithium metal batteries
NMR	Nuclear magnetic resonance
PEGA	Poly(ethylene glycol) acrylate
PEGMA	Poly(ethylene glycol) methacrylate
PEO	Polyethylene oxide
SHE	Standard hydrogen electrode
SEI	Solid electrolyte interphase
SPE	Solid polymer electrolytes
SSEs	Solid-state electrolytes
TFSI	Bis(trifluoromethanesulfonyl)imide
TGA	Thermogravimetric analysis
THF	Tetrahydrofuran
T_g	Glass transition temperature
Tm	Melting temperature
TTS	Time–temperature superposition
T_v	Topology freezing temperature
t_{Li+}	Lithium transference number
UV	Ultraviolet
VFT	Vogel–Fulcher–Tammann
WLF	Williams–Landel–Ferry
wt%	Weight percentage

Notes

In this work, the terms anode and cathode are used to refer to the negative and positive electrodes, respectively. This specification is necessary because anode and cathode are reversed between charging and discharging processes.

All electrochemical potentials will be reported with respect to the Li/Li^+ redox couple (−3.04 V vs. the standard hydrogen electrode (SHE))

1. Context

Solar panel and wind turbines are often described as the future for energy production. They offer renewable and low-carbon alternatives to fossil fuels, and their global deployment has increased rapidly over the past decades. However, these systems are inherently intermittent, as they depend on weather conditions, which leads to fluctuation between electricity demand and production. To overcome this limitation, the storage of electrical energy is essential.

Large-scale storage technologies such as pumped hydroelectric storage currently play a significant role in energy storage (over 90% of the global energy storage). This method is based on the conversion between electrical and gravitational potential energy. It remains the most widely deployed energy storage solution worldwide due to its maturity and large capacity, typically in the range of several gigawatt-hours (GWh). However, its geographical constraints and environmental impact limit its expansion, thereby reinforcing the need for alternative storage technologies such as batteries.[1, 2]

Another sector contributing to the growing demand for energy storage is portable and transportable applications, driven by the increasing demand for small electronic devices such as smartphones, laptops, and electric tools, as well as the rapid expansion of electric vehicles (EVs). The transition to electric mobility plays a key role in reducing greenhouse gas emissions and improving air quality, particularly in urban areas where air pollution remains a significant concern. For both EVs and portable electronic devices, lithium-ion batteries (LIBs) are currently the most widely used energy storage systems, due to their high energy density, relatively long cycle life, and good efficiency.[3, 4]

The rapid expansion of lithium-ion battery technologies has also increased the demand for critical raw materials such as lithium, cobalt, nickel, and manganese, which are commonly used in commercial cathode materials. While these elements contribute to high electrochemical performance and energy density, their extraction and processing raise important environmental, economic, and geopolitical concerns. At the same time, as the demand for energy storage technologies continues to increase, improving the performance, safety, lifetime, and sustainability of batteries has become a major technological challenge. Current lithium-ion batteries still face several limitations, including safety concerns associated with flammable liquid electrolytes, limited recyclability, and performance degradation over time. Therefore, developing safer, more durable and more sustainable batteries is an important objective for future energy storage technologies.[5]

2. Theoretical background

2.1. Li-ion batteries

2.1.1. Structure of Li-ion batteries

Lithium-ion (Li-ion) batteries consist of two electrodes separated by an electrolyte and connected through an external electrical circuit (Figure 1). The electrodes act as host materials capable of reversibly inserting and extracting Li^+ ions within their structures. Each electrode is characterized by a distinct electrochemical potential, which reflects its thermodynamic tendency to accept or release lithium ions.

During battery operation, lithium ions move from one electrode to the other under the driving force of potential difference, while electrons simultaneously flow through the external circuit to power the intended device. Ion transport occurs through the electrolyte, which is typically a liquid medium ensuring ionic conductivity. To prevent direct physical and electrical contact between the electrodes, and thus avoid internal short circuits, a porous separator is placed between them within the electrolyte.[6]

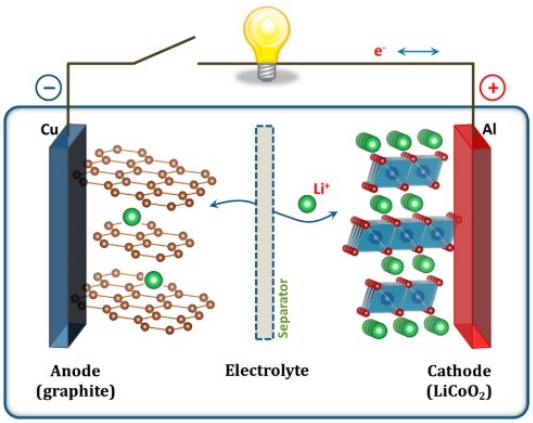

Figure 1 Structure of a Li-ion battery.[6]

2.1.2. Electrolyte and lithium salt

The design of an electrolyte is a complex task that requires balancing several key properties. It must, first, enable efficient Li^+ ion transport between the electrodes. It must remain electronically insulating to ensure that electrons flow through the external circuit rather than within the cell. The electrolyte must be stable across the battery electrochemical window to prevent decomposition and gas production. Other important considerations include its melting and boiling points, toxicity, and chemical compatibility with the other cell components, such as the electrodes, current collectors, and separator.[7]

To date, most commercial electrolytes are based on organic solvents containing a dissolved lithium salt. These systems typically consist of mixtures of carbonate organic solvents (e.g. dimethyl carbonate and ethylene carbonate), which offer a well-balanced combination of properties, including high lithium salt solubility, suitable viscosity, a broad operating temperature range, chemical inertness toward other components, and stability over a wide potential window.[7]

For the lithium salt, the choice of anion is crucial, as it must ensure high solubility as well as adequate electrochemical and thermal stability. Weak interactions between the lithium cation and the anion are generally favored to enhance salt dissociation and ion mobility. Larger anions are often advantageous. The anion also plays a key role in the formation of the solid electrolyte interphase (SEI), which directly impacts battery stability and lifetime. Since no single salt optimizes all these parameters, practical systems rely on a trade-off between them. For example, lithium hexafluorophosphate ($LiPF_6$) is widely used due to its overall balanced performance despite limited thermal stability, while salts such as lithium tetrafluoroborate ($LiBF_4$) and lithium bis(trifluoromethanesulfonyl)imide (LiTFSI) are investigated for their improved stability and/or ionic conductivity under specific conditions.[8]

2.1.3. Anode

To increase battery performance, new electrode materials with higher capacity and better voltage need to be found. For negative electrode material, most commercial batteries rely on graphite, hard or soft carbon technology (LiC_6, 372 $mAh.g^{-1}$). These materials work with an intercalation mechanism. Due to low Van Der Waals force between the graphene layers, Li^+ ions can intercalate between the layers. These materials have interesting electrochemical potential but not the best capacity. They are used thanks to their structure stability (small volume change) as well as cycling stability.[9]

$$C_6 + Li^+ + e^- \leftrightarrow LiC_6$$

Equation 1 Graphite lithiation equilibrium

Other material such as silicon ($Li_{15}Si_4$, 3579 $mAh.g^{-1}$) or metal alloys (Li_3Al_2, 1490 $mAh.g^{-1}$) offers higher capacity, but they suffer from low cycling stability due to large volume changes during charge/discharge (Figure 2). This may result in mechanical destruction of electrode material.[10]

In recent years, research has focused on a lithium metal anode, which has a low voltage and high capacity, but has practical problems. This specific anode will be discussed later in this work.

2.1.4. Cathode

Current commercial cathode material for Li-ion batteries relies on two materials: $LiFePO_4$ (LFP) and $LiNiMnCoO_2$ (NMC). LFP cathodes possess a moderate capacity (150 $mAh.g^{-1}$), however, they have other interesting characteristics: very low cost, environmental safety and long cycling efficiency. NMC cathodes, on the other hand, offer higher capacity (170 $mAh.g^{-1}$). Nickel rich NMCs can reach 210 $mAh.g^{-1}$ but suffer from lower stability. Other cathode materials are available ($LiCoO_2$, $LiNiCoAlO_2$, V_2O_5,…) (Figure 2) but they suffer from different drawbacks: low voltage, low capacity or low stability.[11]

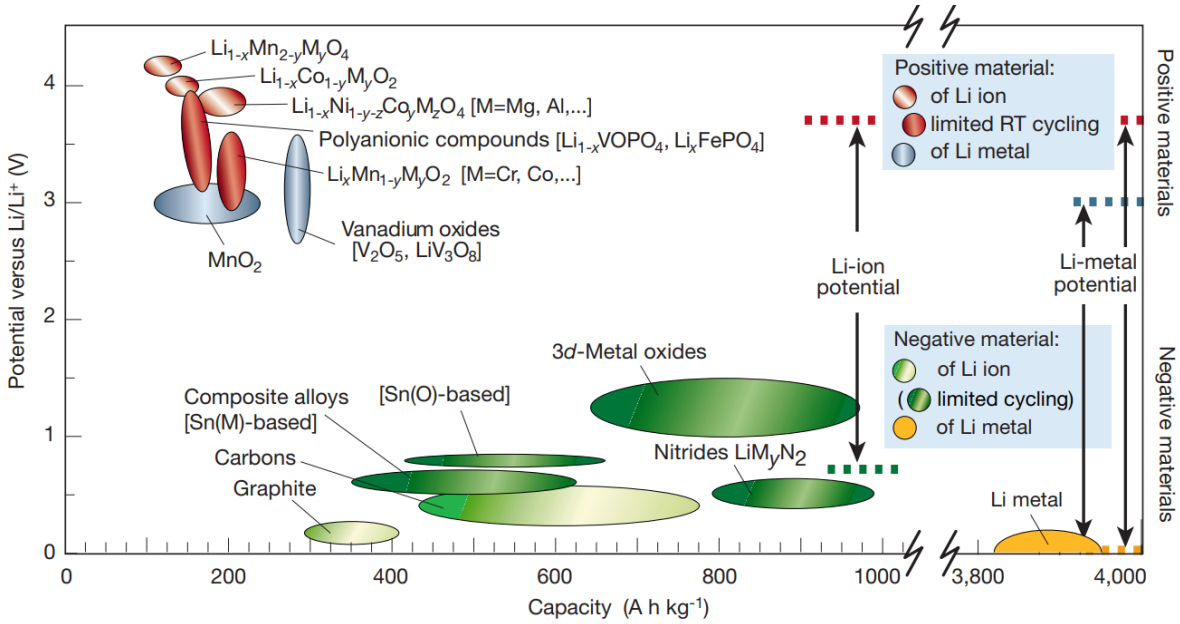

Figure 2 Voltage vs capacity for positive (red and blue) and negative (green and yellow) electrode materials.[12]

2.1.5. Performance and limitations

Battery performances are often defined by their amount of energy per mass or volume ($Wh.kg^{-1}$) or ($Wh.L^{-1}$) depending on the aimed application. This quantity of energy is the product of C, the specific capacity or volumetric capacity ($Ah.kg^{-1}$ or $Ah.L^{-1}$) and V, the potential difference between the electrodes (V) (Equation 2).

$$E\ (Wh.kg^{-1}) = C\ (Ah.kg^{-1}) \times V\ (V)$$

Equation 2 Relationship between energy density, specific capacity, and cell voltage.

The capacity is the ability of the material to store Li^+ ions per mass or volume. A high capacity comes from a high ability to absorb/release ions without losing stability. The cell voltage

originates from the difference in chemical potential between the two electrodes and is therefore strongly dependent on their chemistry. During discharge, Li^+ moves from the anode, where it is less stable, to the cathode, where it is more stable. This difference in stability provides the driving force for electron flow through the external circuit and therefore determines the battery voltage.[12, 13]

Although battery performance is commonly described by its energy density and power density, several other criteria must be considered when evaluating a battery technology. Safety is an important factor: battery malfunction can lead to fire, explosions, and the release of toxic materials in the environment. Rechargeable batteries also need to perform enough cycles without losing efficiency. With time and cycles, batteries undergo different stresses: mechanical stresses, temperature changes and electrochemical reactions. These effects can shorten battery life or reduce their overall performance. Other aspects such as raw materials need to be considered: their availability, their cost, their impact on the environment (extraction, carbon emission, water consumption).[5] Other new generation systems, such as Na-ion, Li-Sulphur and Li-air batteries are currently under research, but they will not be developed in this work.[14]

In this work, different aspects of batteries will be studied for higher performances and better safety. Especially, systems with a lithium metal anode and a solid polymer electrolyte.

2.1.6. Lithium metal anode and lithium dendrites

Lithium metal is often described as an optimal material for negative electrode due to its characteristics: high theoretical capacity (3860 $mAh.g^{-1}$), low electrochemical potential (-3.04 V vs SHE) and low density (0.53 $g.cm^{-3}$). However, despite these advantages, lithium metal has not yet achieved large-scale industrial deployment, mainly due to the formation and growth of dendrites during repeated cycling.

After several plating and stripping cycles, little needle-like structures appear on the Li metal surface. These dendritic lithium structures can progressively penetrate the electrolyte and the separator, eventually reaching the positive electrode. That leads to an internal short circuit, rapid heat generation and a significant risk of thermal runaway, fire, or explosion (Figure 3).[15]

In addition to safety issues, dendrite formation also compromises coulombic efficiency. Lithium dendrites are typically long and fragile, they can easily fracture during stripping. Once electrically disconnected from the electrode, these isolated lithium fragments, “dead lithium”, remain trapped in the electrolyte and can no longer participate in electrochemical reactions. This irreversible loss of active lithium leads to a gradual decrease in coulombic efficiency and capacity fading over time.[16]

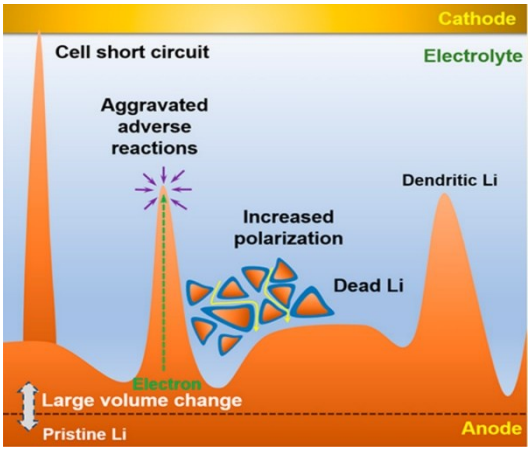

Figure 3 Dendrites effects for lithium metal batteries.[17]

Dendrite nucleation and growth are strongly dependent on both temperature and current density. At low temperature, the diffusion coefficient of Li^+ in the electrolyte decreases, resulting in an enhanced concentration polarization near the electrode surface. This transport limitation promotes a non-uniform lithium deposition and accelerates dendritic growth. Similarly, high current densities increase dendrite formation.[18] With these pronounced dependences of dendrite formation on temperature and current density, developing effective strategies to slow down or suppress dendrite growth is essential for lithium metal batteries (LMB), particularly under practical operating conditions such as room temperature and fast-charging regimes.

2.1.7. Polymer electrolytes

As mentioned earlier, most commercial systems employ liquid electrolytes, typically composed of mixtures of cyclic and linear organic carbonates, combined with lithium salt such as $LiPF_6$ or LiTFSI. While these organic liquid electrolytes offer high ionic conductivity and good electrochemical performance, they also present significant safety drawbacks, as any electrolyte leakage can expose the highly toxic and flammable liquid components.

To overcome the limitations associated with liquid electrolytes, extensive research has been dedicated to the development of solid-state electrolytes (SSEs). SSEs possess a high thermal stability, good stability with lithium metal electrodes and a higher resistance to Li dendrite growth. They can be broadly classified into two main categories: polymer electrolytes and inorganic electrolytes. Inorganic electrolytes, which consist of ceramic materials based on sulfides and oxides, will not be addressed in this work.[19]

For solid polymer electrolytes (SPEs), the transport of lithium ions mainly relies on the presence of poly(ethylene oxide) (PEO). The oxygen atom of the ether functions incorporated in these polymers exhibit a strong coordination with Li^+ ions. This promotes the dissolution of Li salts within the polymer. Li^+ ion transport occurs via two complementary mechanisms: intrachain

hopping along a PEO chain and interchain hopping between adjacent polymer chains. These mechanisms collectively enable the movement of ions through the polymer (Figure 4).[20]

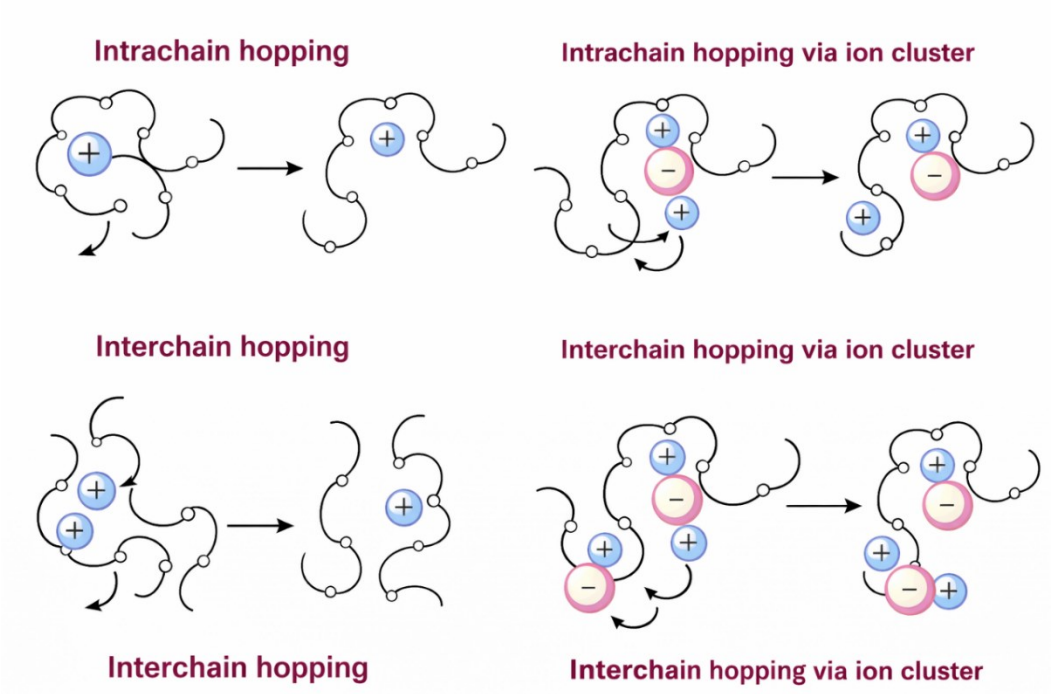

Figure 4 Proposed mechanism of ion transport in PEO.[20]

Poly(ethylene oxide) is a semi-crystalline polymer. The amorphous phase plays the major role in Li^+ transport as it provides higher segmental mobility than the crystalline domains. The crystalline regions restrict chain dynamics, thereby limiting interchain ion hopping and reducing overall ionic conductivity. Applications below 60 °C, corresponding to the melting temperature (T_m) of PEO, remain challenging due to insufficient conductivity. Therefore, polymer electrolytes are often designed using materials with low melting temperatures or amorphous polymers with low glass transition temperatures ($T_{g)}$ in order to maximize segmental mobility and ionic conductivity.[20]

Among the various polymers incorporating ethylene oxide (EO) units, poly(ethylene glycol) methyl ether methacrylate (PEGMA) comb polymers (Figure 5) emerge as particularly promising candidates for SPE. As conventional (PEO)-based systems, PEGMA facilitates lithium salt dissolution and dissociation. In addition, its comb-like architecture, characterized by flexible side chains, significantly reduces crystallinity and enhances side chain segmental mobility. PEGMA with approximately 9 EO repeating units appears to provide an optimal balance between ion solvation and side chain mobility.[21] PEGMA also demonstrates improved electrochemical stability compared to poly(ethylene glycol) acrylate (PEGA), as it avoids redox reactions associated with the hydrogen atoms in the α-position relative to the carbonyl group.[22]

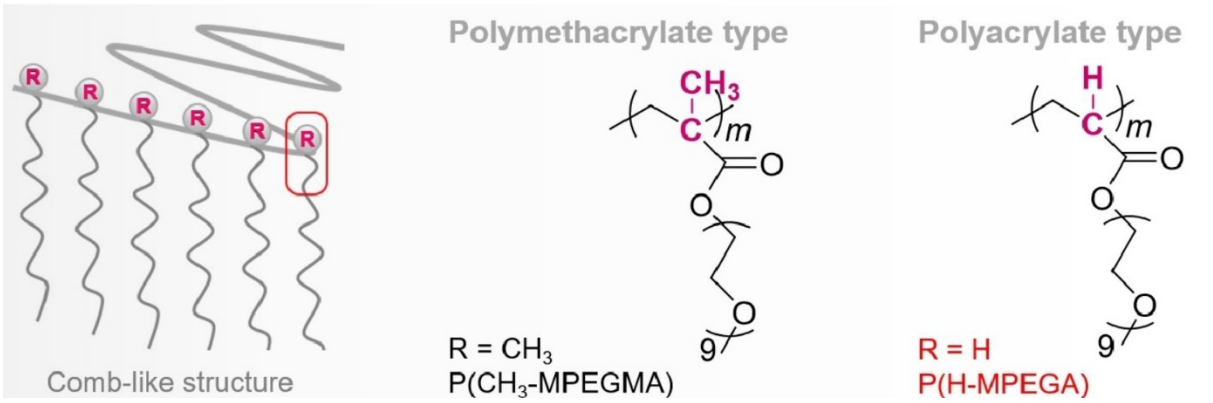

Figure 5 PEGMA and PEGA comb-like structure.[22]

2.1.8. Application: Blue Solutions' batteries and Bluecar

Polymer electrolytes combined with lithium metal electrodes are often presented in the scientific literature as a prospective solution for next-generation batteries with a development limited to small-scale laboratory research.[23] However, this technology has already been implemented at an industrial level and is commercially available for use in electric vehicles, including cars and buses. These vehicles are produced by Bluebus, with battery production carried out by Blue Solutions. Since 2012, the French company has been selling electric cars and buses powered by lithium metal batteries employing polymer electrolytes.[24]

The Bluecar is a compact four-seat, three-door electric vehicle specifically designed for urban mobility and car-sharing services. Introduced in 2011, the vehicle offered a driving range of approximately 250 km under urban conditions, which was reasonable at the time but later became limited compared to newer lithium-ion electric vehicles.[24] The battery operated at elevated temperature to ensure sufficient ionic conductivity of the polymer electrolyte, which imposed additional thermal management requirements. Production of the Bluecar was stopped in 2018. Since then, the company has shifted its focus toward electric buses powered by improved lithium metal polymer (LMP) batteries, offering up to 320 km of autonomy and approximately 5 hours for a full charge.[25]

The electrolyte developed by Blue Solutions is based on a diblock copolymer architecture. One block consists of (PEO), which serves for the transport of lithium ions through the polymer electrolyte, as described above. The second block is a polyanionic polymer incorporating TFSI groups covalently attached to the polymer backbone (poly(TFSI)).[26] This architecture is designed to immobilize the anionic species while maintaining Li^+ ion mobility (Figure 6).

The lithium transference number (t_{Li+}) is defined as the fraction of the total ionic current carried by lithium ions. In conventional polymer electrolytes, both lithium cations and counter-anions contribute to charge transport, resulting in relatively low t_{Li+} values. By covalently binding the TFSI

anions to the polymer chain, their mobility is strongly reduced, and charge transport becomes predominantly cationic. This electrolyte exhibits a lithium transference number close to one. High lithium transference numbers have been shown to reduce concentration polarization during battery cycling, thereby improving cell performance and limiting dendrite growth at the lithium metal interface.[27, 28] Using this approach, Blue Solutions reports electrolytes combining a lithium transference number close to 1, with good mechanical properties, sufficient ionic conductivity, and strong resistance to dendritic growth.[26, 29]

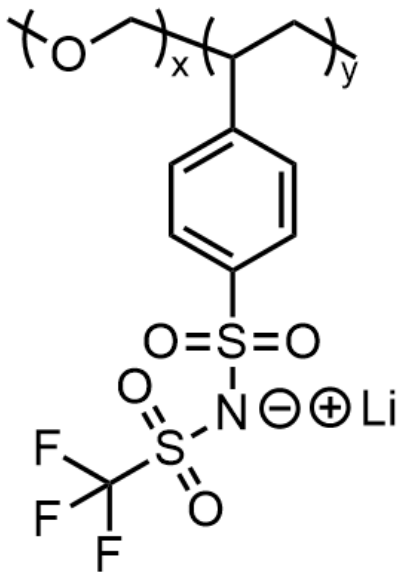

Figure 6 Chemical structure of the PEO-b-poly(styrene-TFSI-Li) electrolyte developed by Blue Solutions.[26]

2.2. Vitrimers

2.2.1. Thermosets and thermoplastics

Polymers can be classified into two main families: thermoplastic and thermoset polymers, which differ in both structure and properties. Thermoplastics are made of linear or branched chains held together by weak intermolecular interactions. They soften when heated and harden upon cooling, allowing them to be reshaped multiple times without significant chemical change. Thermoplastics are easy to recycle and reprocess. In contrast, thermosets are formed through chemical reactions that create a rigid, crosslinked three-dimensional network. This structure makes them mechanically strong and thermally stable but prevents them from melting or being reprocessed once formed. When exposed to high temperatures, thermosets tend to degrade rather than flow.[30]

At the end of their life cycle, thermoset materials pose a significant environmental challenge due to their non-reprocessable crosslinked structure. A large proportion of thermoset wastes are still disposed in landfills, where they accumulate because they are neither biodegradable nor easily recyclable. This practice is increasingly restricted by environmental regulations, particularly in Europe, which encourage more sustainable waste management strategies.

Alternative end-of-life options include incineration, which allows energy recovery but generates greenhouse gas emissions and does not enable material valorization. Mechanical recycling enables the reuse of ground thermoset wastes as fillers, but the resulting materials exhibit lower performances. Chemical recycling can recover valuable components such as monomers or reinforcing fibers, but it often requires complex processes and chemical inputs. Despite these methods, no universally efficient and economically viable solution has yet been established for thermoset wastes.[31]

2.2.2. Covalent adaptable networks

To address the intrinsic recyclability limitations of thermosets, researchers have shifted their focus toward the development of novel polymer systems rather than improving existing recycling methods. In this context, a new class of materials has emerged, combining the advantageous mechanical properties of thermosets, arising from crosslinked polymer networks, with the reprocessability of thermoplastics.

These materials are based on an innovative design of the crosslinked network, in which traditional permanent covalent networks are replaced by covalent adaptable networks (CANs). In such systems, the crosslinks are not irreversibly fixed but are chemically designed to be dynamic. As a result, the network can undergo reversible transformations, including bond cleavage, reformation, or exchange reactions, depending on the chosen chemistry and operating conditions. This dynamic behavior enables reshaping, self-healing, and recycling of the material without

significantly compromising its structural integrity, thereby offering a promising strategy to reconcile performance and sustainability in polymer design.[32]

Covalent adaptable networks are divided into two categories depending on their exchange mechanism: associative or dissociative. In an associative mechanism, a new bond is formed before the old one is cleaved. This behavior is observed in several dynamic chemistries commonly used in CANs, such as transesterification reactions, boronic ester exchange, and vinylogous urethane exchange. In a dissociative mechanism, the opposite occurs: a bond is first cleaved and only subsequently reformed. Typical examples include Diels–Alder adducts and alkoxyamine linkages (Figure 7). This fundamental distinction has important implications for the evolution of the crosslink density. Associative networks preserve a constant crosslink density during rearrangement, whereas dissociative networks exhibit a variable crosslink density, depending on external parameters such as temperature or chemical environment.[33] Due to the variable crosslink densities, dissociative CANs have been less studied than associative CANs, since variations in mechanical properties during processing can be limiting for certain applications.

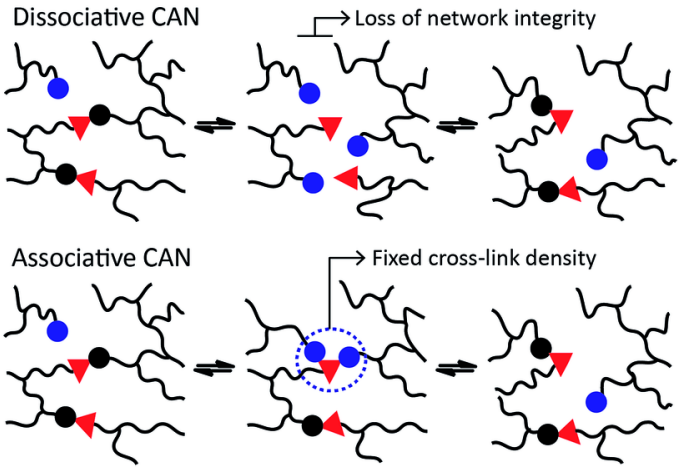

Figure 7 Dissociative and associative mechanism of covalent adaptable network.[33]

In this study, we will focus on associative covalent adaptable networks, also known as vitrimers.

2.2.3. Vitrimers

Vitrimer materials constitute a distinct class of polymer networks that combine features traditionally associated with thermosets and thermoplastics, while also exhibiting unique dynamic properties. Like thermosets, vitrimers possess a permanently crosslinked three-dimensional network, which gives them high mechanical stability and excellent resistance to chemical degradation. They are also generally insoluble in common solvents.[34]

Vitrimers also share several characteristics with thermoplastics, they can be reprocessed and reshaped upon heating. Their viscoelastic behavior is strongly temperature-dependent, allowing them to soften and flow under appropriate thermal conditions. This combination of rigidity at ambient temperature and processability at elevated temperature makes them highly versatile materials.

The most distinctive aspect of vitrimers lies in their associative mechanism. They contain dynamic covalent bonds that can undergo exchange reactions without altering the overall network connectivity, enabling topological rearrangements while preserving the integrity of the polymer structure. Thus, vitrimers exhibit stress relaxation, reprocessability, recyclability, and even self-healing capabilities, properties that are not typically observed in classical thermosets.[30, 33]

2.2.4. Topology freezing temperature

For polymer materials, the glass transition temperature is one of the most important thermal properties. Below T_g, polymer chains have very limited mobility and the material behaves as a rigid and brittle glassy solid. Above T_g, segmental motions of the polymer chains become possible, leading to a transition to a softer and more flexible rubbery state. In conventional thermosets, this transition only affects the mobility of the polymer chains, while the permanent crosslinked network remains intact. Thermosets exhibit a rubbery plateau above T_g and do not flow even at elevated temperatures.

In vitrimers, the situation is more complex because the material contains dynamic covalent bonds capable of exchanging while maintaining a constant crosslink density. In addition to T_g, vitrimers exhibit a second characteristic temperature called the topology freezing temperature (T_v). T_v is defined as the temperature at which the bond exchange reactions become too slow to allow network rearrangement on the experimental timescale. This transition is conventionally chosen at the point where the viscosity of 10^{12} Pa.s is reached. Below T_v, the network topology is frozen, and the material behaves similarly to a conventional thermoset. Above T_v, the exchange reactions become sufficiently fast to enable continuous network rearrangement, allowing the material to flow while remaining permanently crosslinked.[34]

The relative positions of T_g and T_v determine the thermomechanical behavior of a vitrimer (Figure 8). When T_v is higher than T_g (Figure 8 A), the material first undergoes the classical glass-to-rubber transition at T_g. Between T_g and T_v, it behaves as an elastomer because the polymer chains are mobile, but the network topology remains frozen. Above T_v, bond exchange reactions become rapid enough to allow macroscopic flow, and the vitrimer behaves as a viscoelastic liquid. In contrast, if T_v is lower than T_g (Figure 8 B), the glass transition becomes the dominant factor controlling the material behavior, as the exchange reactions are already active before significant chain mobility is reached. Therefore, both T_g and T_v must be considered to fully understand the thermal and rheological properties of vitrimer materials.[33, 34]

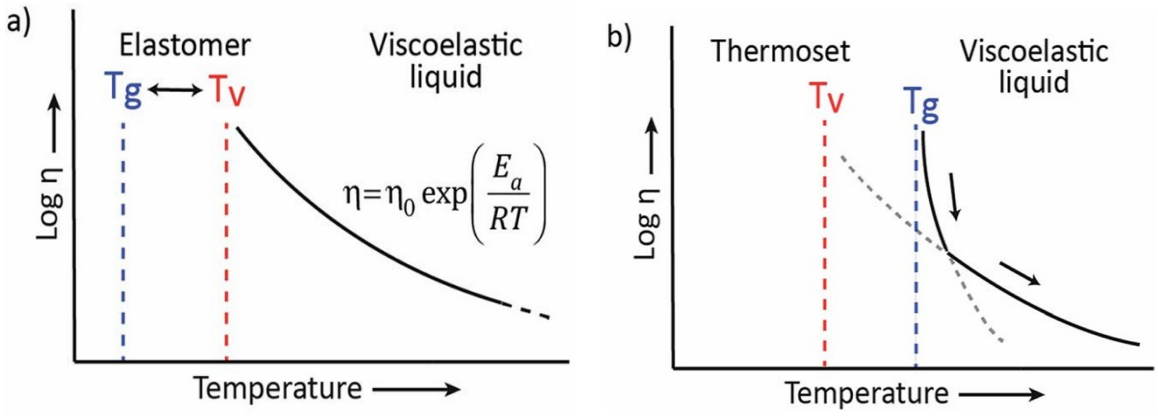

Figure 8 Graph of viscosity as a function of temperature for vitrimers with a) T_g, lower than T_v and b) T_v, lower than T_g.[33]

2.2.5. Vitrimer synthesis

Different strategies can be employed to introduce dynamic bonds into a polymer network. They can be divided into two general approaches: the polymerization of multifunctional monomers and the crosslinking of thermoplastics. In the first approach, vitrimers are obtained by polymerizing multifunctional monomers. The dynamic covalent bonds can either be formed during the polymerization (Figure 9 A) or already be present in the monomers (Figure 9 B and C). The advantage of this technique is the formation of the network in a one-step reaction. However, the dynamic bond chemistry needs to be compatible with the polymerization technique. Removing trapped unreacted material and impurities from the vitrimer is also difficult with this technique.

In the second approach, thermoplastics are crosslinked to introduce dynamic covalent bonds. If the polymer already contains suitable functional groups, it can be directly crosslinked using multifunctional agents (Figure 9 D and E). Otherwise, an additional functionalization step is required to introduce reactive sites on the thermoplastic before crosslinking (Figure 9 F). This route offers flexibility in the choice of polymer matrix, dynamic chemistry and reaction conditions.

In this work, we will focus on the polymerization of multifunctional monomers, and especially with a difunctionalized monomer containing the dynamic bond (Figure 9 C). [34]

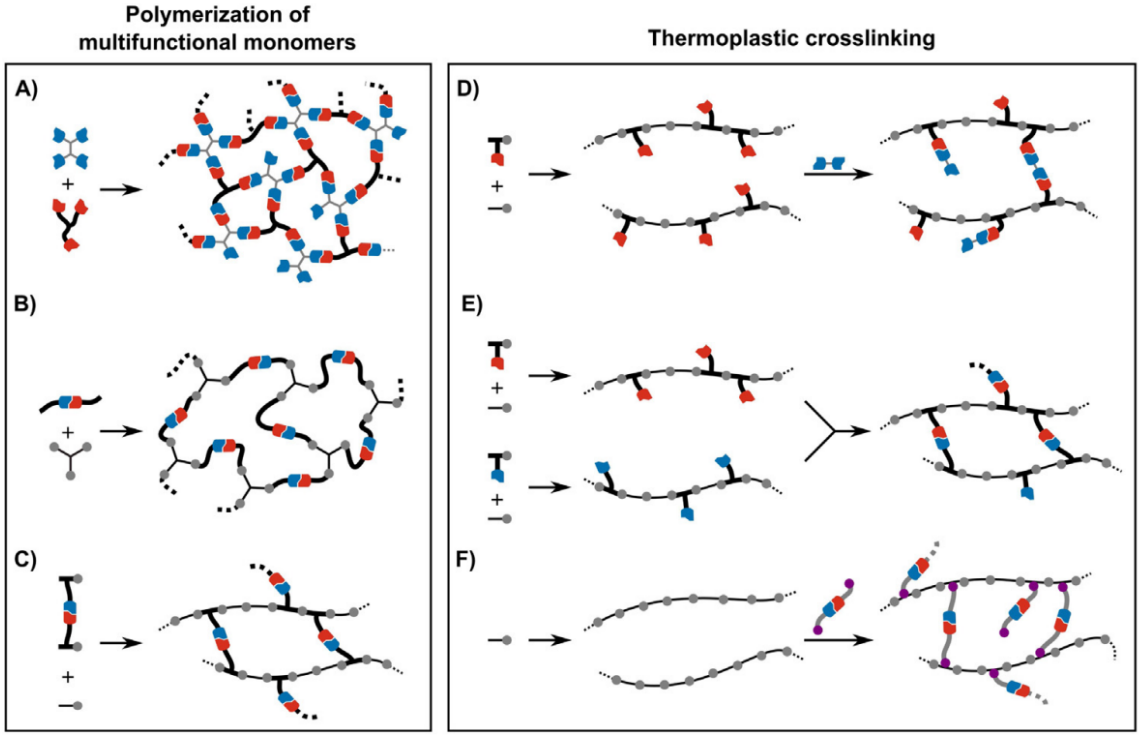

Figure 9 Main strategies used to prepare vitrimer networks through polymerization of multifunctional monomers and thermoplastic crosslinking.[34]

2.2.6. Dioxaborolane vs Dioxazaborocane (DB vs DZ)

This work will focus on the study of boronic ester vitrimers, especially dioxaborolane (DB) and dioxazaborocane (DZ). DB boronic esters have been extensively studied in polymer literature as dynamic covalent crosslinking bonds. Usually, these dynamic crosslinks react through a transesterification mechanism, but in absence of nucleophilic catalyst, water or alcohol, boronic esters react through a metathesis mechanism (Figure 10).[35] The metathesis of dioxaborolane bonds has been demonstrated to facilitate rapid and thermally stable bond exchange.[36]

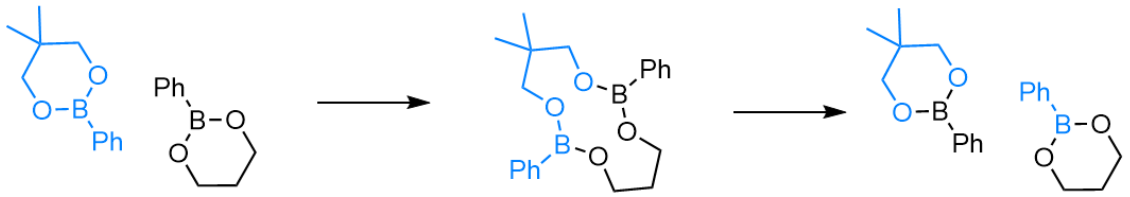

Figure 10 Boronic ester metathesis mechanism.[35]

Although DB-based vitrimers exhibit satisfactory dynamic properties, specific applications demand enhancements in both hydrolytic stability and exchange kinetics. One of the primary limitations of DB boronic ester linkages is their susceptibility to hydrolysis in the presence of moisture, which can compromise network integrity and long-term performances. To address this, researchers have pursued chemical strategies that reduce the electrophilicity of the boron center by completing its octet through intramolecular coordination with a Lewis base, typically a nitrogen donor, which forms a dative N→B bond.[37]

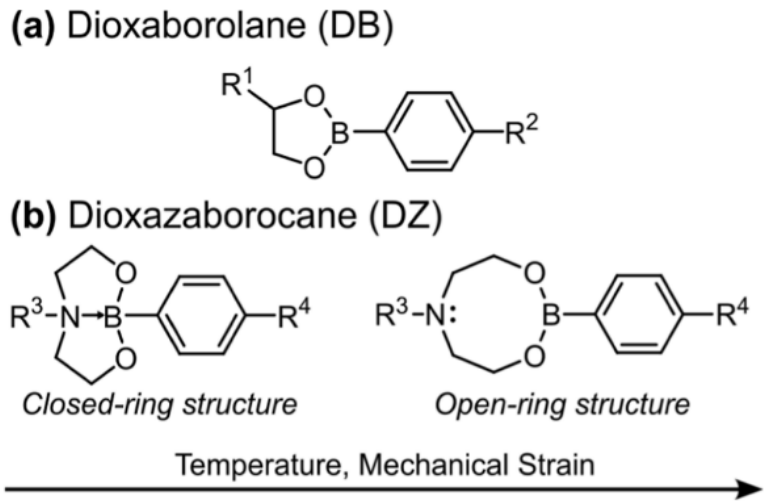

Figure 11 a) Chemical structure of a dioxaborolane.(b) Chemical structure of a dioxazaborocane as function of temperature and mechanical strain. [38]

At lower temperatures, the N→B bond forms a stable tetracoordinated boron species, which reduces the susceptibility of the boronic ester to hydrolysis. This coordinated structure also decreases the reactivity of boronic esters toward metathesis under ambient conditions, which is opposite to the targeted optimization. However, when the temperature increases, the N→B interaction becomes weaker, allowing the coordinated bond to open. In this open form, the boron atom becomes more accessible and reactive toward the exchange reactions that enable network rearrangement (Figure 11). Thus, the material can remain stable against water at normal conditions but still exhibit dynamic behavior at elevated temperatures.[38]

2.3. Vitrimer electrolyte

Polymer electrolytes and vitrimer materials have each been introduced with their key advantages. The combination of these two concepts will now be discussed by considering vitrimer-based electrolytes and the benefits they may offer compared to classical polymer electrolytes.

2.3.1. Properties

In traditional polymer electrolytes, ionic transport only relies on segmental motion within a static network. Permanent crosslinks restrict chain mobility and can significantly limit ion transport. Increasing the crosslinking density generally improves mechanical properties but restricts chain mobility, leading to lower ionic conductivity and reduced interfacial contact with the electrodes. This trade-off between mechanical robustness and ion transport remains one of the main challenges in polymer electrolyte design.

Vitrimer electrolytes offer a promising strategy to address this limitation. In addition to the classical segmental motion mechanism, the dynamic bond exchange reactions continuously rearrange the polymer network while maintaining the overall crosslinked structure. These rearrangements can facilitate ion transport by increasing local chain mobility. Ionic conduction in vitrimer electrolytes comes from a combination of segmental motion and network dynamics. However, the respective contribution of these two mechanisms remains poorly understood and is still the subject of ongoing research.[39]

Beyond conductivity, the dynamic nature of vitrimer networks provides several advantages for battery applications. Network rearrangements and flow behavior improve the contact between the electrolyte and the electrodes by allowing the material to adapt to volume changes during cycling and to dissipate mechanical stresses. Vitrimer electrolytes can also exhibit self-healing and reprocessability, enabling the repair of mechanical defects and the recycling or reshaping of the material without significant loss of performance. These properties make vitrimers attractive candidates for safer, more durable, and more sustainable battery technologies. [40, 41]

Despite their promising characteristics, vitrimer electrolytes remain an emerging research field. Several challenges still need to be addressed, including achieving high ionic conductivity below 60°C, optimizing the balance between conductivity and mechanical strength, and improving long-term electrochemical stability. The influence of network dynamics on ion transport is not yet fully understood. Future developments will also require the exploration of new dynamic chemistries and network architectures, as only a limited number of exchange mechanisms have been investigated in battery applications so far.[40]

2.3.2. Salt impact on vitrimers

Most studies on vitrimer materials investigate the mechanical properties in the absence of additives. However, for electrochemical applications, the incorporation of lithium salt is essential. Although salts may appear chemically inert, they can significantly influence the rheological behavior of vitrimers, particularly through Lewis acid–base interactions.

Several studies have reported an acceleration of network dynamics in vitrimer electrolytes based on vinylogous urethane and imine chemistry in the presence of lithium salts. This effect is commonly attributed to the coordination of Li^+ ions with carbonyl and/or nitrogen parts, which enhances bond exchange processes.[42, 43]

In boronic ester–based vitrimers, coordination between the anion and the boron center has also been shown to accelerate network reactivity (Figure 12).[40, 44] To date, however, no studies have specifically addressed the impact of salts on dioxazaborocane-based systems, where the boron atom is already partially coordinated through an intramolecular nitrogen–boron interaction.

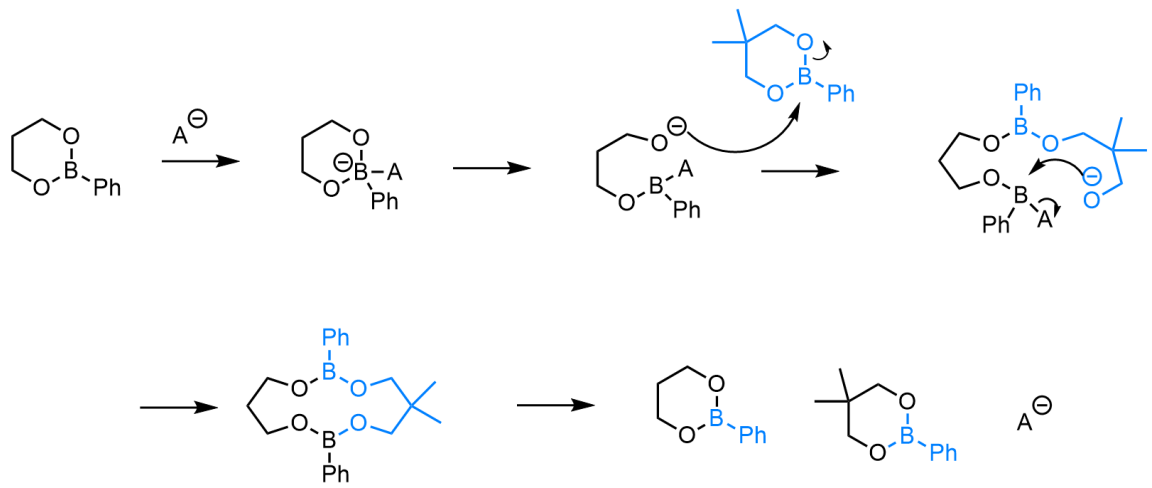

Figure 12 Boronic ester metathesis mechanism catalyzed by a nucleophile.[35]

2.3.3. Examples of Vitrimer Electrolytes

In this section, three representative vitrimer electrolyte systems based on different dynamic chemistries are presented. Figure 13 A shows a boronic ester network obtained by crosslinking hydroxyl-terminated PEO chains with boric acid. The resulting electrolyte exhibited ionic conductivities up to 3.5×10^{-4} S.cm^{-1} at 90 °C. In addition, the material displayed efficient self-healing, reaching 98% recovery after 34 h at 60 °C, while the addition of lithium salt significantly accelerated the network dynamics. The network was fully reversible, dissolving in water to regenerate the original monomers, highlighting its potential as a sustainable electrolyte.[44]

Figure 13 B presents an imine-based vitrimer formed by the condensation of PEG diamine and 1,3,5-triformylbenzene. This system combined high flexibility, with an elongation at break exceeding 500%, and an ionic conductivity of 7.48 × 10^{-4} S.cm^{-1} at 25 °C. The electrolyte also exhibited a wide electrochemical stability window of 5.0 V vs. Li/Li^+, room-temperature self-healing capability, and good battery cycling performance.[45]

Figure 13 C illustrates a disulfide-based vitrimer consisting of an epoxy network containing flexible PEG diglycidyl ether segments and dynamic disulfide crosslinks. This material exhibited a tensile strength above 20 MPa together with a self-healing efficiency exceeding 95% after 2 h at room temperature. Depending on the composition, ionic conductivities above 10^{-3} S.cm^{-1} at room temperature were achieved.[46]

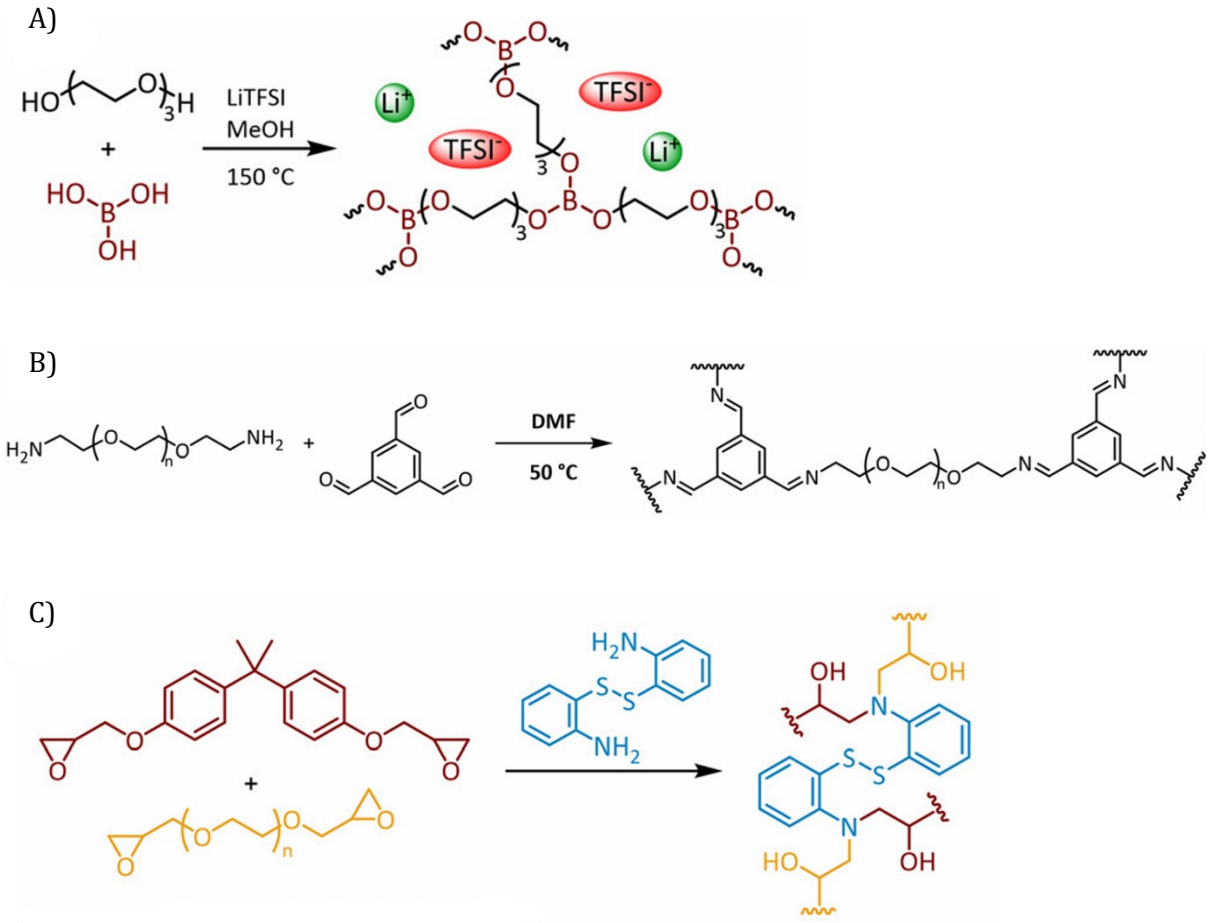

Figure 13 A) Synthesis of PEO-based dynamic boronic ester networks.[44] B) Condensation polymerization of PEG diamine with 1,3,5-triformylbenzene.[45] C) Synthesis of a vitrimeric electrolyte with a rigid and flexible epoxy resin as a backbone and disulfide bonds as reversible crosslinking points.[46]

2.4. Characterization

2.4.1. Conductivity

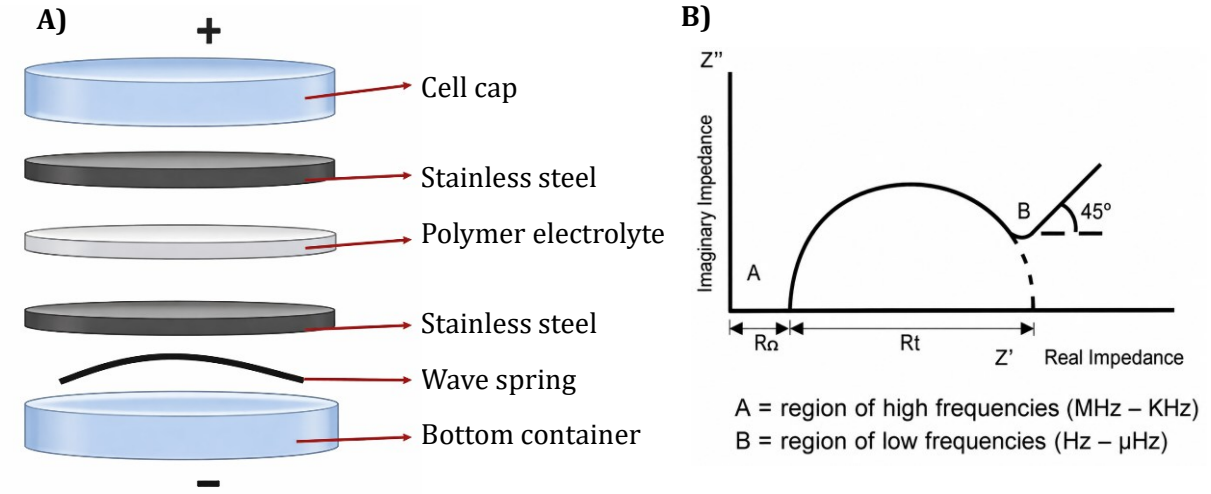

Figure 14 A) Cell setup for electrochemical impedance spectroscopy (EIS).[47] B) Nyquist diagram.[48]

The ionic conductivity of solid electrolytes constitutes a key parameter for the overall performance of solid-state batteries, as it reflects the material's ability to transport ions efficiently. It is therefore widely employed as a primary criterion for evaluating and comparing novel electrolyte candidates. In practice, ionic conductivity is commonly determined by electrochemical impedance spectroscopy (EIS), a technique that measures the opposition of a system to an alternating electrical signal. This technique involves applying a small-amplitude alternating potential across the system while sweeping the frequency over a broad range, typically from MHz to mHz, and recording the corresponding impedance response.

Impedance is a complex quantity that accounts for both resistive effects (real part) and capacitive or inductive effects (imaginary part), thereby providing a comprehensive description of charge transport and storage phenomena within the material. The impedance response is commonly represented using a Nyquist plot, in which the imaginary component of the impedance is plotted against the real component (Figure 14 B). This representation is particularly useful in electrochemistry as it enables the identification of distinct contributions within the system, such as bulk resistance and interfacial processes, through characteristic features in the plot.

The electrolyte is typically incorporated into a symmetric blocking electrode setup, in which it is placed between two electronically conductive but ion-blocking electrodes (stainless steel) (Figure 14 A). This geometry ensures that ionic transport occurs exclusively through the electrolyte layer, while preventing charge transfer reactions at the interfaces. The ionic conductivity is calculated based on the following formula:

$$\sigma = \frac{L}{R_b A}$$

Equation 3 Relationship between bulk resistance and conductivity.

Where R_b is the bulk resistance obtained via the Nyquist plot, L (in cm) is the thickness of the sample, A (in cm^2) is the electrode contact area and σ (in $S.cm^{-1}$) is the conductivity. This approach provides a reliable and widely adopted method for quantifying ionic transport in solid electrolyte materials.[47]

2.4.2. Rheology

Rheology is the study of how materials deform and flow, with a particular focus on viscoelastic systems that exhibit both solid-like and liquid-like behaviors. It involves the application of different deformations (stress or strain), and the measurement of the material's reaction over time. By analyzing this response, it is possible to determine whether the material behaves more elastically (storing energy) or more viscously (dissipating energy), and how this balance evolves under different conditions. In this work we will focus on two different experiments: frequency sweep and stress relaxation.

Frequency sweep experiments are commonly used to characterize the viscoelastic behavior of vitrimers over different timescales. In these measurements, the material is subjected to oscillatory deformation with different frequencies. Their objective is to determine the viscoelastic profile of the material, schematically represented in Figure 15, by measuring the evolution of the storage modulus (G′), associated with the elastic response, and the loss modulus (G″), associated with viscous dissipation.

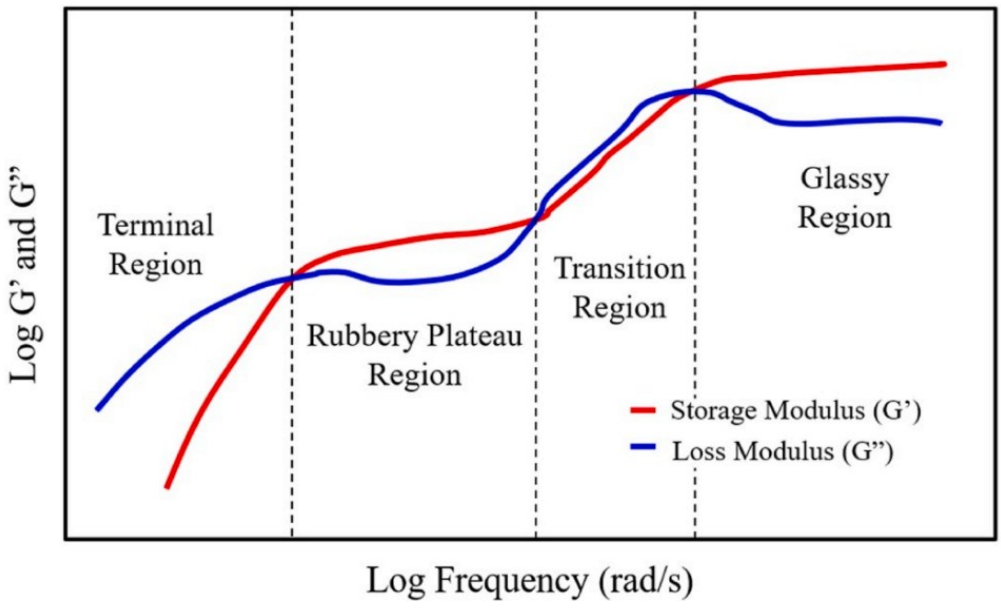

Figure 15 Typical viscoelastic patterns for a flowing polymer system.[49]

For the vitrimer systems investigated in this work, particular attention will be given to the rubbery plateau, the terminal regime, and the G'-G'' crossover that separates these two domains. The rubbery plateau, observed at high frequencies, reflects the crosslinked density. At lower frequencies, the material has sufficient time to undergo network rearrangements through dynamic bond exchange reactions, leading to the terminal regime. The transition between these two behaviors is marked by the G′-G″ crossover, which is related to the characteristic relaxation time of the network. A crossover occurring at higher frequencies indicates a faster relaxation process and a more dynamic vitrimer network.

Frequency sweep measurements are inherently limited by experimental time constraints, meaning that only a portion of the viscoelastic response of a polymer can be accessed at a given temperature. To extend the accessible timescale and obtain a more complete description of the material dynamics, the time–temperature superposition (TTS) principle is commonly employed. Frequency sweeps are performed at different temperatures and superimposed by applying a horizontal shift factor (a_T) along the frequency axis, allowing the construction of a master curve spanning several decades in frequency (Figure 16). For vitrimers, TTS is particularly informative because the temperature dependence of the shift factors reflects the kinetics of dynamic bond exchange reactions within the network. The shift factors often exhibit an Arrhenius behavior (when the system is well above T_g), from which an activation energy can be extracted.

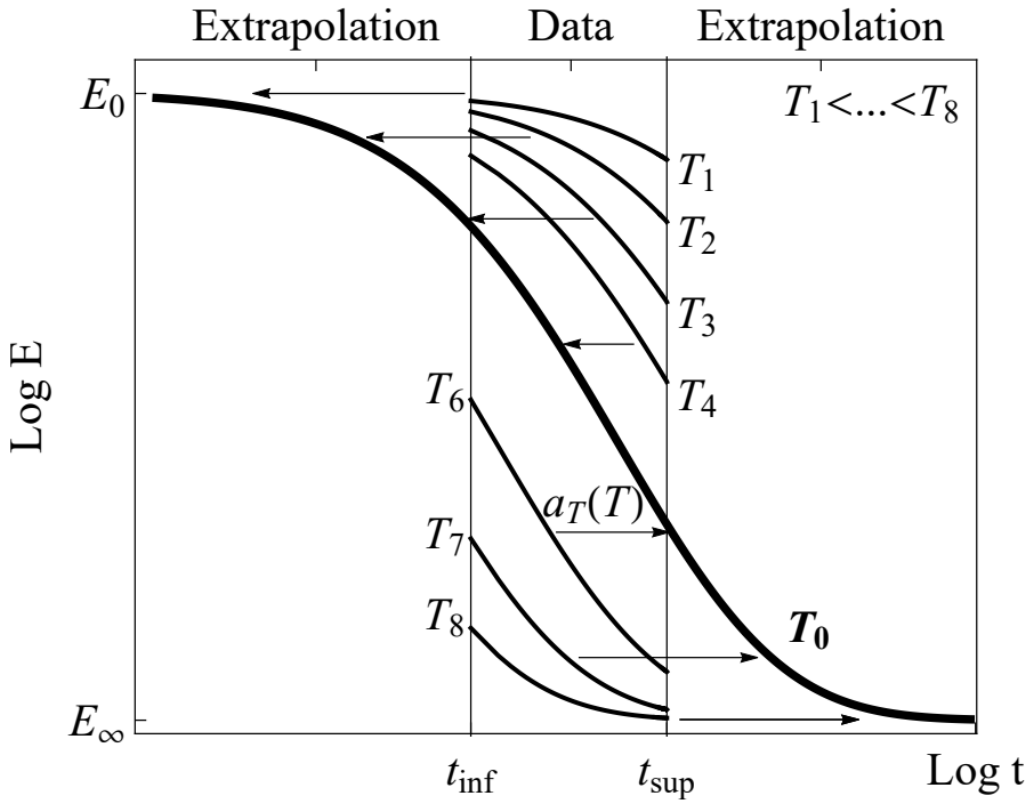

Figure 16 Scheme of the Time–Temperature Superposition (TTS) principle for the building master curve from short-time tests at different temperatures.[50]

Stress relaxation experiments are used to study the ability of a viscoelastic material to dissipate stress over time after deformation. In this test, a constant strain is rapidly applied to the sample and maintained while the decrease in stress is monitored as a function of time. For highly elastic materials, the stress remains relatively constant, whereas for more viscous or dynamic systems, the stress progressively decreases due to molecular rearrangements within the network. In vitrimers, stress relaxation is mainly governed by dynamic covalent bond exchange reactions, which allow the polymer network to reorganize and release internal stresses. The relaxation profile provides important information about the mobility of the polymer chains, the kinetics of bond exchange, and the characteristic relaxation time of the material. Faster stress decay generally indicates a more dynamic network.[51, 52]

3. Previous work and objectives

This work is part of a PhD project dedicated to the development of vitrimer electrolytes based on boronic ester chemistry. The overall objective is to understand the relationship between the dynamic properties of vitrimer networks and their ionic conductivity as well as other vitrimer properties, including self-healing, reprocessability, recyclability, and thermal stability.

The studied polymer electrolytes are based on PEGMA and boronic ester derivatives. PEGMA is incorporated to promote lithium-ion transport, while the boronic esters are used as crosslinkers to give vitrimer behavior. Initial studies within the group focused on networks composed of PEGMA and a dioxaborolane (DB) crosslinker (Figure 17 A). These materials exhibited promising ionic conductivity (10^{-3} S.cm^{-1} at 60°C) but slow dynamic properties. Network dynamics were improved by adding dioxazaborocane (DZ) dangling groups alongside the DB crosslinker (Figure 17B).

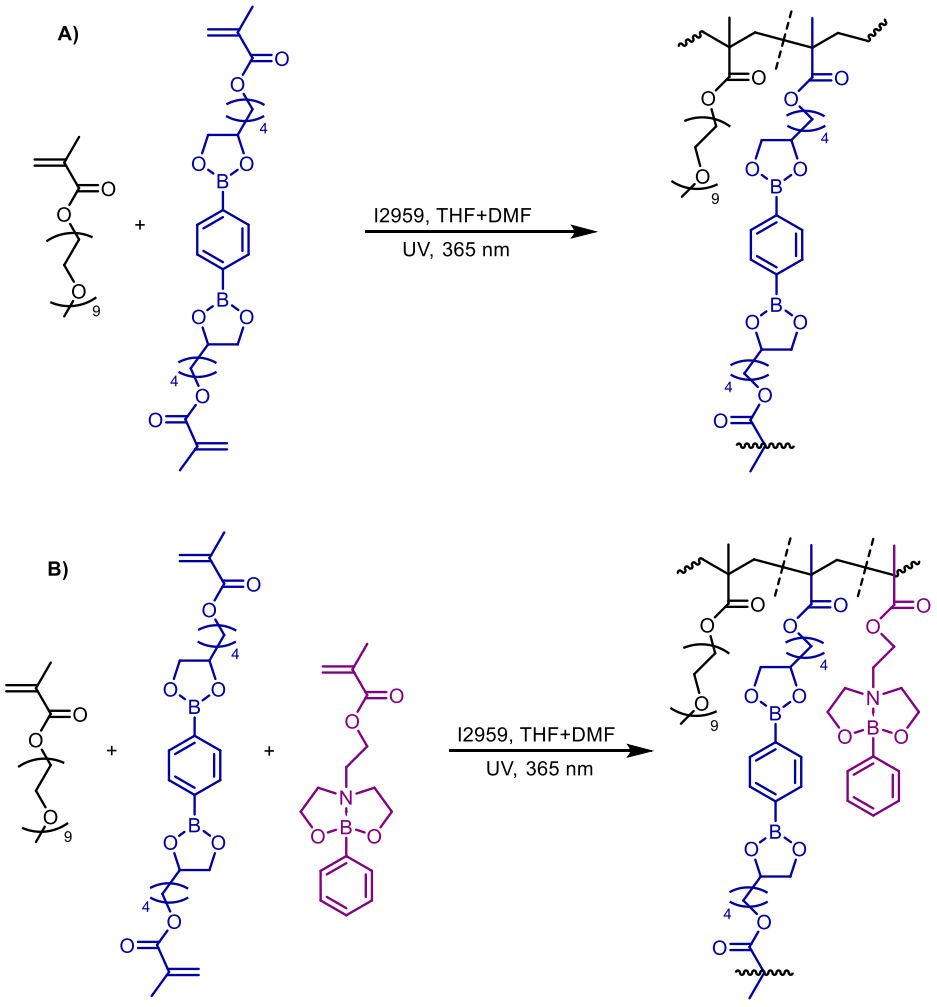

Figure 17 A) Photopolymerization of the DB system (PEGMA + DB crosslinker). B) Photopolymerization of the DBDZ system (PEGMA + DB crosslinker + DZ dangling group)

The objective of this work is to continue the research described above by replacing the DB crosslinker with a dioxazaborocane crosslinker to further enhance the dynamic properties. Two systems will be studied, one with PEGMA and the DZ crosslinker (DZ system), the other with PEGMA, the DZ crosslinker and the DZ dangling group (DZDZ system) (Figure 18).

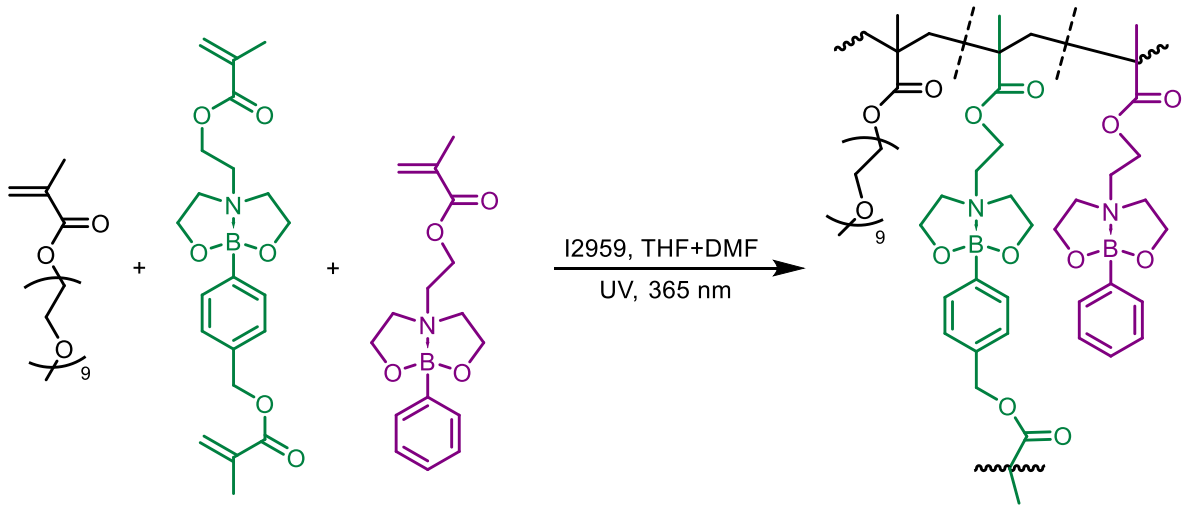

Figure 18 Photopolymerization of the DZDZ system (PEGMA + DZ crosslinker + DZ dangling group).

This study covers both the synthesis and characterization of the dioxazaborocane-based vitrimer electrolytes. The dioxazaborocane monomers and crosslinkers will be synthesized and incorporated into polymer networks through UV-initiated free-radical photopolymerization. The influence of network composition and the presence of lithium salt ($LiClO_4$) on the properties of the materials will be investigated.

The synthesized materials will be characterized using polymer characterization techniques: Fourier-transform infrared spectroscopy (FTIR) will be used to confirm the successful conversion of the monomers into polymer networks, while differential scanning calorimetry (DSC) and thermogravimetric analysis (TGA) will be performed to evaluate the thermal properties and thermal stability of the materials. These analyses will be carried out on systems both with and without $LiClO_4$ to assess the effect of lithium salt incorporation.

Characterization methods specific to vitrimer electrolytes will be employed. Rheological measurements (frequency sweep and stress relaxation experiments) will be used to investigate the viscoelastic properties and network dynamics of the materials. Electrochemical impedance spectroscopy (EIS) will be performed to determine the ionic conductivity of the networks.

Compared to the previously studied DB systems, the DZ networks are expected to exhibit faster bond-exchange dynamics. The main objective of this work is therefore to determine how these accelerated network dynamics influence the rheological behavior of the materials and if they can lead to improved ionic conductivity.

4. Results and discussion

4.1. Instruments and methods

4.1.1. Nuclear magnetic resonance (NMR)

The ^{1}H-NMR spectra were measured with a 400 MHz Jeol JNM-ECZL spectrometer. NMR tubes were prepared by dissolving 10 mg of sample in 500 µL of $CDCl_3$ or DMSO as solvent.

4.1.2. Differential scanning calorimetry (DSC)

DSC analysis was carried out on Mettler Toledo DSC 1 STAR System Thermal Analysis instrument. Approximately 10 mg of compound was introduced into a 40 µL aluminum crucible and the corresponding lid was pressed on top to seal the container using the Mettler Toledo press. The DSC performed a 3 scans analysis: heating the sample from RT to 100°C, isothermal step at 100°C for 10 minutes, cooling the sample from 100°C to -80°C, isothermal step at -80°C for 10 minutes, heating the sample from -80°C to 100°C, with heating and cooling rate of 10°C.min^{-1}.

All samples are amorphous and remained well above their T_g throughout the rheological and conductivity measurements.

4.1.3. Thermogravimetric analysis (TGA)

TGA was carried out on Mettler Toledo's TGA/SDTA 851e instrument. Approximately 10 mg of sample was introduced into an alumina crucible, which was heated (10°C.min^{-1}) from 30°C to 700°C under nitrogen flow (50 mL.min^{-1}).

4.1.4. Fourier-transform infrared spectroscopy (FTIR)

Fourier-transform infrared spectra were recorded using a PerkinElmer Spectrum Two spectrometer in ATR mode. Small pieces of the polymer samples were analyzed directly in solid state. Spectra were collected over the range of 4000–400 cm^{-1} with intervals of 0.25 cm^{-1}. For each spectrum, four scans were accumulated and averaged.

4.1.5. Electrochemical impedance spectroscopy (EIS)

EIS measurements were performed using a VMP-300 Potentiostat from BioLogic over a frequency range of 7 MHz to 100 mHz and with an amplitude AC excitation voltage of 10 mV. The electrochemical cells were placed into a climate chamber. The electrochemical impedance spectra

were collected for a temperature range from 90 °C to 20 °C by gradually decreasing the temperature by steps of 10 °C with an equilibration time of 30 min between each measurement.

Coin cells were assembled using the following configuration: positive case, 1 mm stainless steel spacer, vitrimer electrolyte disk (8 mm diameter, thickness between 0.5 and 0.7 mm), 1 mm stainless steel spacer, spring and negative case. To prevent electrolyte flow during the measurements, the electrolyte disk was inserted into a silicone ring with a central hole of 8 mm diameter (thickness of 0.3 mm). All cells were assembled inside an argon glove box to minimize moisture and oxygen contamination, then sealed using a pressure press at 60 $kg.cm^{-2}$. After electrochemical testing, the coin cells were opened, and the thickness of the sample (electrolyte and the two stainless steel spacers) was measured using a micrometer. Conductivity values were obtained by averaging measurements performed on three samples for each composition.

4.1.6. Rheology: frequency sweep and stress relaxation

Rheological measurements were performed using an Anton Paar MCR 302e rheometer equipped with an 8 mm parallel plate geometry under a nitrogen atmosphere. Disk-shaped samples (8 mm diameter, thickness between 0.5 and 0.7 mm) were equilibrated in the rheometer at 80°C for 1h prior to measurement. Before each measurement, the sample was equilibrated at the selected temperature for 30 min to ensure thermal stability. Measurements were then carried out sequentially from low to high temperature. A final room-temperature measurement was carried out to assess the stability of the sample throughout the experimental sequence.

The linear viscoelastic region was first determined by strain sweep experiments performed at 10 rad/s with shear strains ranging from 0.01 to 15%. For all samples, a strain of 5% was found to remain within the linear viscoelastic regime. Frequency sweep measurements were then conducted at 25, 40, 60, 80, 90, and 120 °C over an angular frequency range from 100 to 0.01 rad/s, using a constant strain of 5% and a normal force of 0.1 N. Stress relaxation experiments were performed at 25, 60, 90, and 120 °C by applying a constant deformation of 3%. Each relaxation experiment was recorded for 1 h 30 min.

4.1.7. Chemicals and reagents

All reagents used are commercially available.

PEGMA n=9 (average MW=475 g/mol) and Irgacure 2959 (I2959) were bought from TCI chemical. LiCLO4 (>95.0%), was supplied by Sigma Aldrich. All other chemicals and solvents were bought from TCI chemical or Sigma Aldrich.

Solvents were bubbled with argon prior to use and PEGMA was passed through an aluminum oxide column before use. All chemicals are stored in a fridge.

4.2. Monomers synthesis

In this study, three different monomers will be used: PEGMA, DZ crosslinker and DZ monomer. PEGMA is commercially available, but the two other DZ compounds must be prepared prior to polymerization. The DZ crosslinker synthesis pathway was developed within our group and the DZ dangling group synthesis pathways was found in the literature.[38]

For the synthesis of both monomers, the formation of the dioxazaborocane group was performed by using the condensation reaction between boronic acid and triethanolamine. This reaction is well known in the literature for the formation of dioxazaborocane.[53]

4.2.1. DZ crosslinker synthesis

The objective of this synthesis is to prepare a bifunctional dynamic crosslinker containing a dioxazaborocane unit for dynamic bond exchange and two methacrylate groups for incorporation into the polymer network through radical photopolymerization.

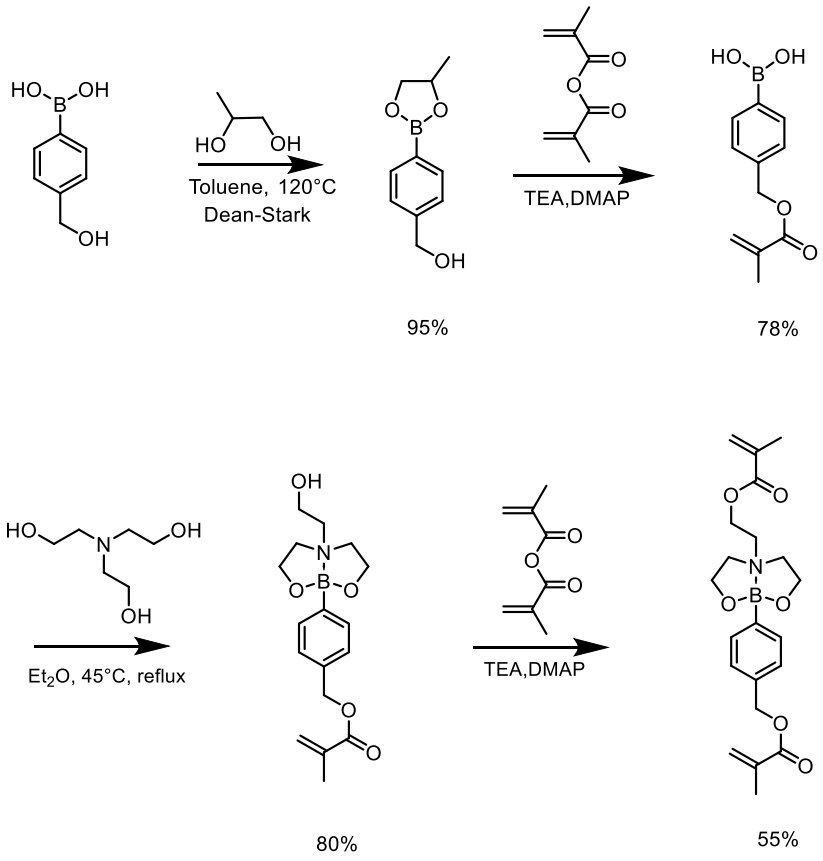

Figure 19 Crosslinker synthesis and yields.

As the synthesis path has already been developed within the group, no problem was encountered. All reactions gave satisfactory yields.

Further experimental details about the synthesis are available in the supplementary information.

4.2.2. DZ monomer synthesis

The objective of this synthesis is to prepare a dangling group containing a dioxazaborocane unit and a single methacrylate group. Unlike the crosslinker, it is attached to the network at only one point and therefore does not increase the crosslink density. Its role is to introduce additional dynamic moieties that may enhance the network dynamics.

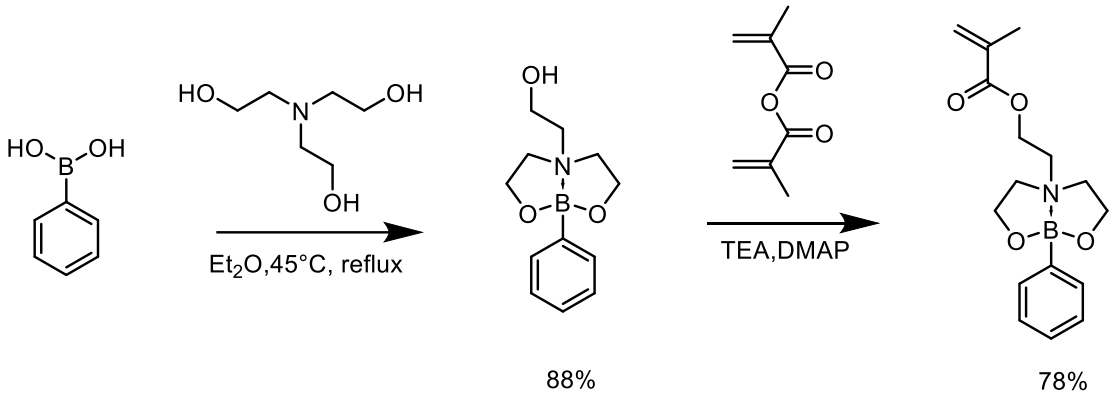

Figure 20 DZ monomer synthesis and yields.

As the synthesis was available in the literature, no problem was encountered and all reactions gave satisfactory yields.[38]

Further experimental details about the synthesis are available in the supplementary information.

4.3. Photopolymerization procedure

DZ crosslinker (18 mg, 5 mol%) and DZ dangling group (13.6 mg, 5 mol%) are dissolved in 80µL of an initiator solution (2 mg, 0.5 wt% of initiator (I2959), 60µL of DMF and 20µL of THF) in an oil bath at 35°C. 400 mg of PEGMA n=9 (400 mg, 90 mol%) are then added. The solution is stirred at 35°C for few minutes, giving a cloudy solution. This solution is placed between 2 glass plates separated by a silicon sheet with the desired shape (0.8 mm thickness). This setup is placed in an oven at 35°C and polymerized with a UV light (365 nm, 2 mW/cm^2) for 20 minutes. The obtained polymer network in unmold and dried in a vacuum oven (80°C, 10 mbar) overnight before characterization.

This procedure (shown in Figure 21) describes the DZDZ network synthesis. For the DZ network, the dangling group (purple monomer) is not added and the amount of PEGMA is increased to 95 mol% (Table 1).

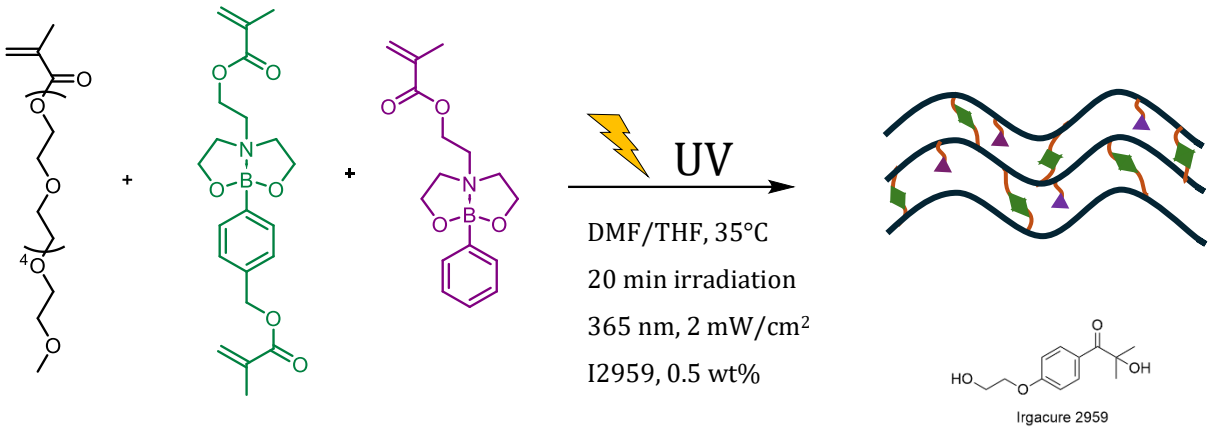

Figure 21 Photopolymerization procedure.

Network	PEGMA (mol%)	DZ Crosslinker (mol%)	DZ monomer (mol%)
DZ	95	5	0
DZDZ	90	5	5

Table 1 Composition of the two studied systems.

Previous studies within the group showed that a crosslinker concentration of 5 mol% offers an optimal balance between mechanical strength and ionic conductivity.

4.4. Study of reaction time

The reaction time was investigated to determine the duration required to achieve complete conversion in our system. This study was performed using FTIR spectroscopy by monitoring the disappearance of the C=C stretching band of the methacrylate monomers at 1640 cm^{-1}, which serves as a marker of the polymerization progress.

Samples were irradiated for varying durations, and their corresponding infrared spectra were recorded. The results shown in Figure 22 indicate that an irradiation time of 20 minutes is sufficient to ensure complete polymerization of the systems.

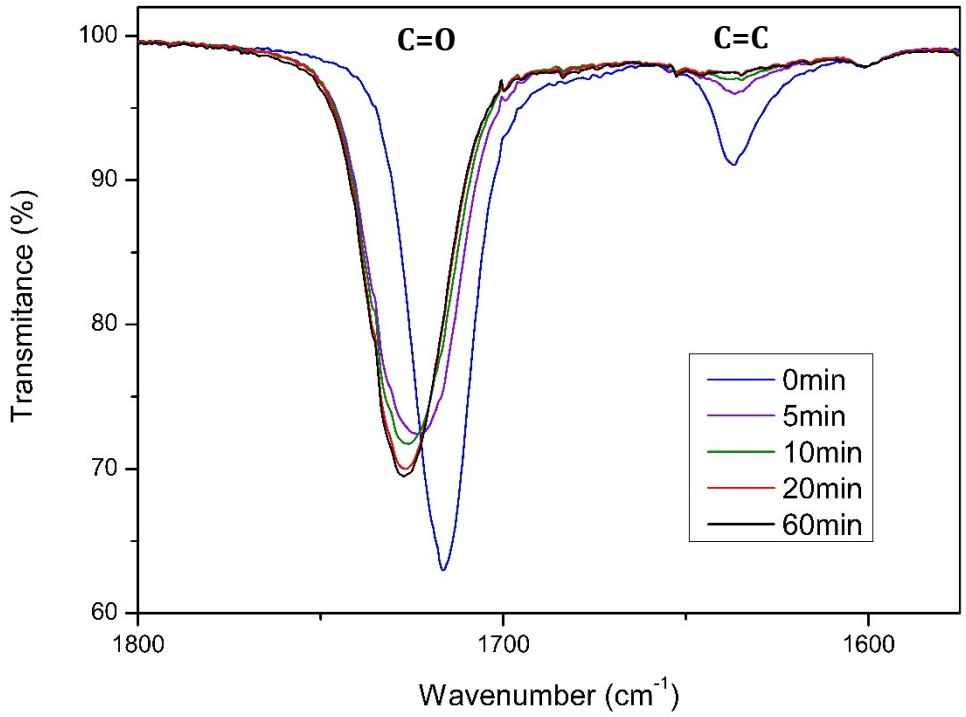

Figure 22 FTIR spectrum (zoomed between 1800cm^{-1} and 1575 cm^{-1}) showing the evolution of the methacrylate C=O and C=C bond for DZDZ samples with different irradiation times.

A shift in the C=O stretching band is also observed. The initial methacrylate carbonyl peak appears at 1716 cm^{-1}, whereas after polymerization it is located at 1727 cm^{-1}. This shift can be attributed to the change in vibrational behavior of the carbonyl group, changing from a C=O bond conjugated with the methacrylate C=C double bond to a non-conjugated C=O bond.

4.5. Presence of residual solvent

The polymerization reaction is carried out in the presence of solvents (THF and DMF). To ensure reliable measurements in both rheology and conductivity experiments, the samples must be thoroughly dried, as residual solvent can significantly influence the observed properties. Within the polymer network, residual solvents can act as a plasticizer, increasing polymer chain mobility and consequently impacting the rheological behavior. In conductivity measurements, the presence of remaining solvent may lead to an overestimation of the ionic conductivity. Rather than ion transport occurring through inter- and intra-chain hopping mechanisms, Li^+ ions may instead be partially solvated and transported via mobile solvent molecules. Finally, the presence of solvent can also affect the electrochemical stability window of the electrolyte.[54, 55]

The potential presence of DMF within the network prior to measurement therefore needs to be carefully evaluated. Residual DMF was investigated by FTIR spectroscopy, focusing on the characteristic C=O stretching band at 1675 cm^{-1}. As shown in Figure 23, this band is no longer detectable after drying overnight in a vacuum oven (<10 mbar) at 80 °C, indicating the complete removal of DMF. Since the boiling point of THF (66 °C) is significantly lower than that of DMF (153 °C), it is assumed that THF is also completely removed during the oven-drying step.

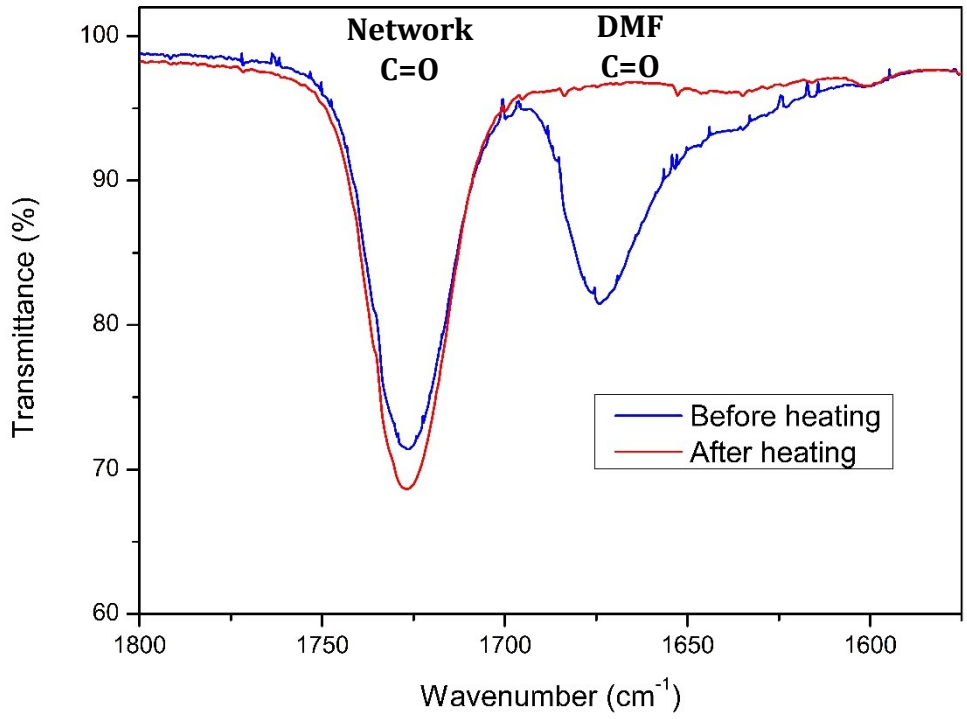

Figure 23 FTIR spectrum (zoomed between 1800cm^{-1} and 1575 cm^{-1}) showing the absence of DMF after heating for a DZDZ sample.

4.6. Rheology

As mentioned earlier, vitrimer properties will be investigated by rheological measurements, particularly through frequency sweep and stress relaxation experiments. These techniques provide information on the material behavior over different temperatures and time scales.

4.6.1. Frequency sweeps

Figure 24 presents a series of frequency sweeps performed between 25°C and 120°C for a DZDZ sample. At low temperatures (≤60°C), the material exhibits a rubbery plateau with a storage modulus of approximately 65 kPa at high frequencies. At lower frequencies, a decrease in the storage modulus accompanied by an increase in the loss modulus is observed, which is characteristic for vitrimers and flowing materials.

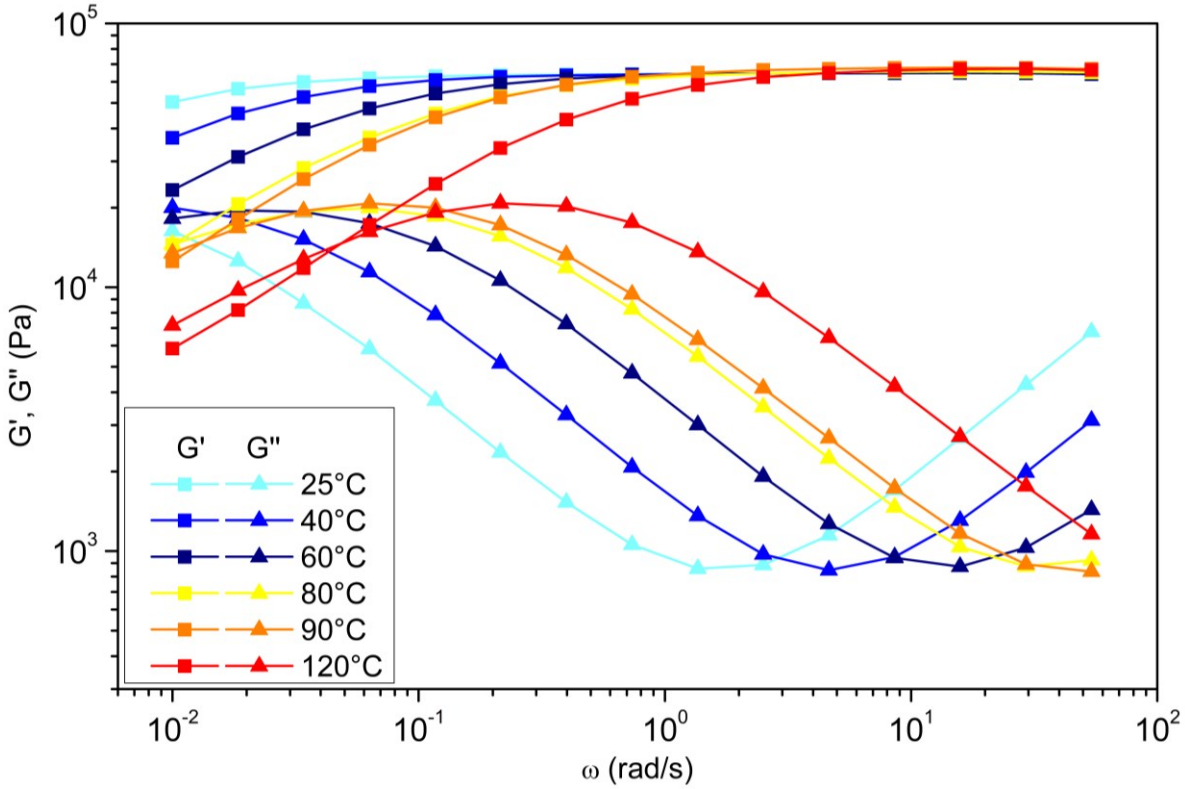

Figure 24 Frequency sweeps at different temperatures of a DZDZ sample.

At higher temperature (≥ 80°C), a similar behavior is observed, with a plateau followed by a decrease of G' and an increase of G''. In addition, a crossover between G' and G'' appears at low frequencies, indicating the transition toward terminal flow behavior, typical of vitrimer materials. The relaxation times (τ) was estimated from the crossover frequency between $G'$and G'', using Equation 4, where ω_{rel}corresponds to the angular frequency at the crossover point.

$$\tau = \frac{1}{\omega_{rel}}$$

Equation 4 Relationship between the relaxation time and the relaxation angular frequency.

Temperature (°C)	Crossover (rad/s)	Relaxation time, τ (s)
80	0.01	100
90	0.014	70
120	0.05	20

Table 2 Relaxation time at different temperatures of a DZDZ sample.

As shown in Table 2, the DZDZ sample exhibits a relaxation time of 20 s at 120°C. This result confirms the dynamic nature of the network and demonstrates an efficient relaxation behavior. However, for battery-related applications, faster relaxation at lower temperatures, closer to the operating conditions of electric vehicles (around 60°C), would be preferable.

4.6.2. Time temperature superposition and activation energy

Figure 25 presents the time–temperature superposition (TTS) master curve obtained from the frequency sweeps shown in Figure 24. A good overlap between the different curves is observed, and no vertical shift was required to construct the master curve. The resulting curve highlights the viscoelastic behavior of the material, showing most of the rubbery plateau as well as the beginning of the terminal regime after the crossover between G' and G''.

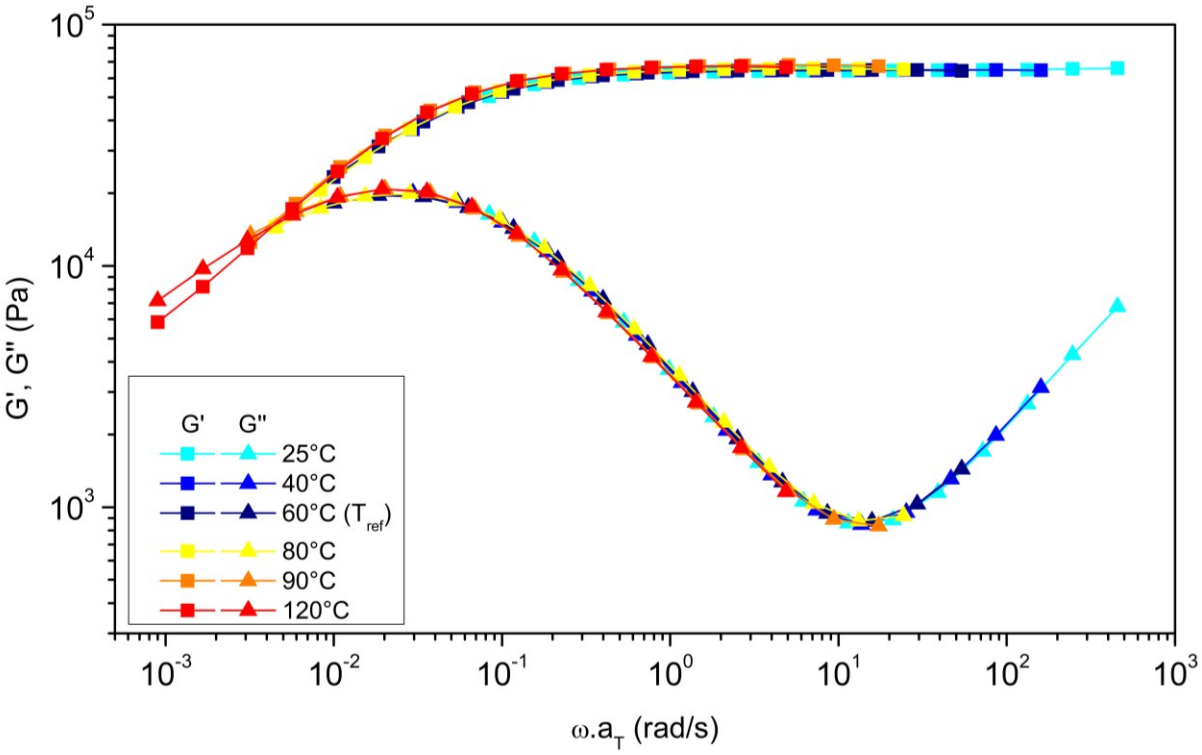

Figure 25 Time temperature superposition of the frequency sweeps of Figure 24. Reference temperature is 60°C.

Based on the horizontal shift factor (a_T) used to build the TTS curve, the activation energy was determined using the Arrhenius relationship (Equation 5). An Arrhenius approach was preferred over the Williams–Landel–Ferry (WLF) model because the measurements were performed well above the glass transition temperature(from T_g + 85°C to T_g + 180°C), where vitrimer relaxation is typically governed by thermally activated bond exchange reactions.[56] In addition, the Arrhenius model provided an excellent fit of the experimental data. An Arrhenius plot (Figure 26) of ln(a_T) as a function of 1000/T was constructed, and the activation energy was calculated by multiplying the slope of the linear fit by the gas constant R.

$$a_T = exp\left[\frac{E_a}{R}\left(\frac{1}{T}-\frac{1}{T_{ref}}\right)\right]$$

Equation 5 Arrhenius relationship for time temperature superposition.

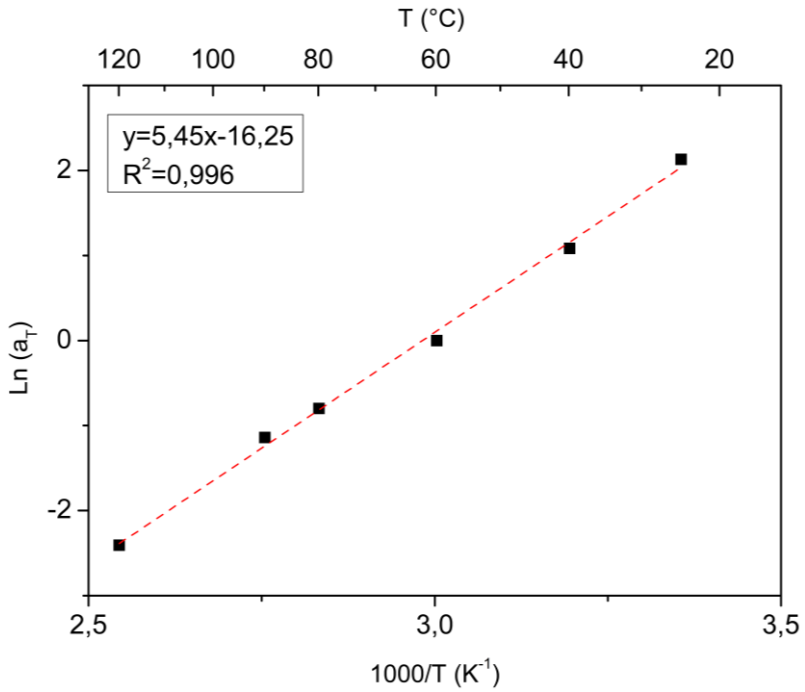

Figure 26 Arrhenius plot of the shift factor of the TTS curve shown in Figure 25.

As shown in Figure 26, the Arrhenius plot exhibits a good linear correlation over the studied temperature range, with no significant deviation between the different measurements. An activation energy of 45 kJ/mol is calculated for this system. This value is also consistent with those reported in the literature for similar systems.[37] However, comparisons with the literature data should be made carefully, as the activation energy strongly depends on both the analysis method and the polymer architecture.

Compared to classical boronic ester (dioxaborolane) systems previously studied within the group, which typically exhibited activation energies in the range of 50–55 kJ/mol, the dioxazaborocane networks synthesized in this work appear to display slightly lower activation energies. This behavior suggests a more dynamic exchange mechanism in the dioxazaborocane-based networks.

4.6.3. Stress relaxation

Figure 27 presents the stress relaxation experiment performed on a DZDZ sample over 1.5 h at different temperatures. The initial modulus is consistent with the G' values observed in the frequency sweep measurements shown in Figure 24.

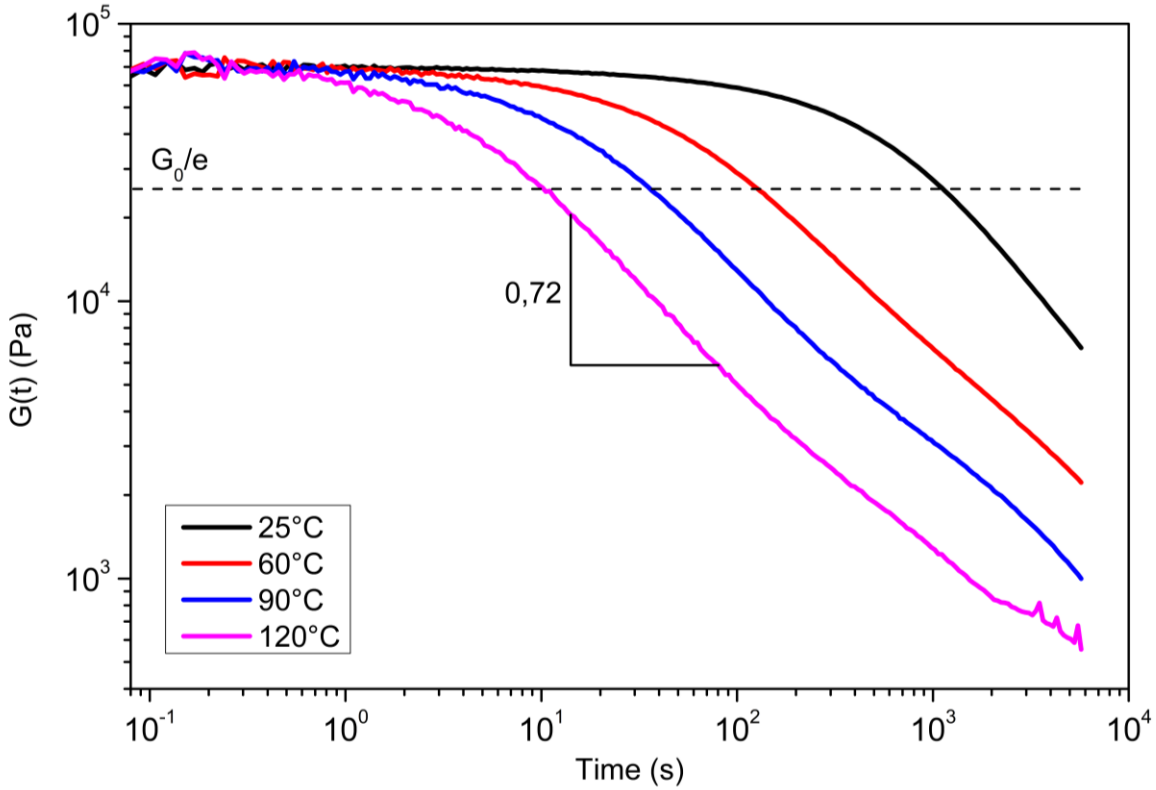

Figure 27 Stress relaxation at different temperatures of a DZDZ sample.

The stress relaxation curves exhibit a slope of −0.72 in the terminal regime. This deviation from the ideal Maxwell behavior, characterized by a slope of −1, suggests that the relaxation process is governed by multiple relaxation modes rather than a single relaxation mechanism. Such behavior is commonly observed in vitrimer systems and can be attributed to the combined effects of associative bond exchange reactions, chain entanglements, and network heterogeneities, leading to slower and more complex stress dissipation dynamics.[57, 58]

In stress relaxation experiments, the characteristic relaxation time (τ) is commonly defined as the time required for the relaxation modulus to decrease to 1/e (≈ 37%) of its initial value. By determining τ at different temperatures and plotting ln(τ) as a function of 1000/T, the activation energy can be extracted using the Arrhenius relationship (Equation 6).

Temperature (°C)	Relaxation time, τ (s)
25	1120
60	127
90	35.8
120	10.25

Table 3 Relaxation time of stress relaxation at different temperatures.

$$\tau = \tau_0 exp\left(\frac{E_a}{RT}\right)$$

Equation 6 Arrhenius relation for relaxation time in stress relaxation.

The 1/e method is frequently criticized because the chosen threshold is arbitrary and may underestimate the activation energy of the system. Nevertheless, this method is used in the present study due to its simplicity and widespread use in the vitrimer literature. [52, 59] The obtained activation energy will then be compared with the value determined by TTS measurements.

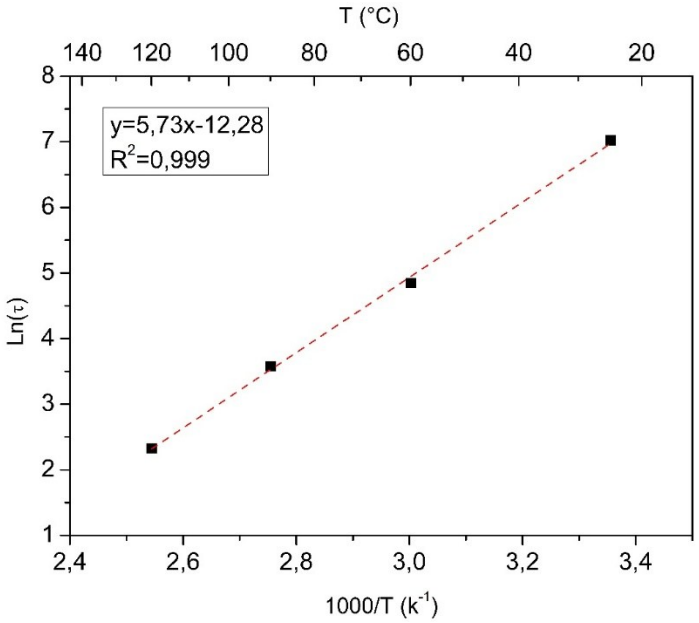

Figure 28 Arrhenius plot of the relaxation time of the stress relaxation curves shown in Figure 27.

Based on Figure 28, an activation energy of 46 kJ/mol is determined from the stress relaxation experiments. This value is close to the one obtained from TTS measurements (45 kJ/mol), indicating a good agreement between both methods.

4.6.4. Systems with and without dangling group

In this section, the effect of the dangling group is investigated by comparing samples containing both the crosslinker and the dangling groups (as shown above) with samples containing only the crosslinker. Only the rheological behavior is discussed here, while the influence on ionic conductivity will be addressed in a later section.

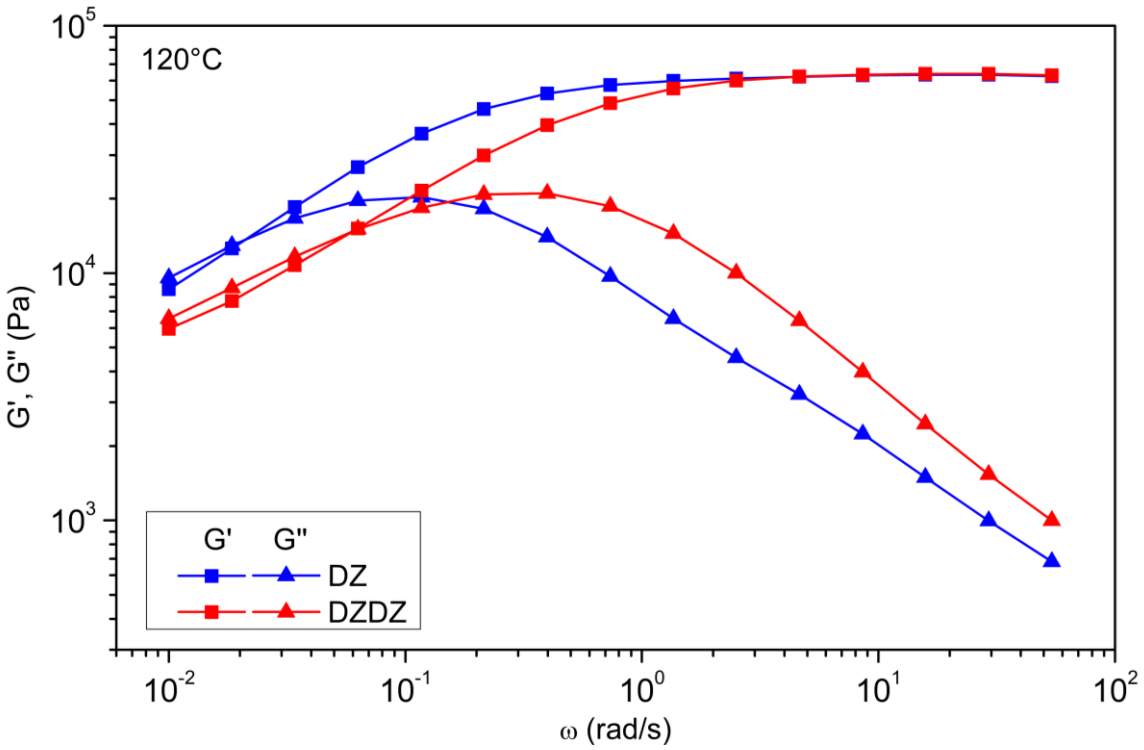

Figure 29 Frequency sweep at 120°C of 2 samples: a DZDZ and a DZ.

Figure 29 presents the frequency sweep curves of two different samples, one containing 5% of crosslinker (DZ) and the other containing 5% of crosslinker and 5% of dangling group (DZDZ). At high frequencies, both materials exhibit a similar storage modulus of approximately 63 kPa. This observation is consistent with the fact that both samples contain the same crosslinker content (5%), leading to a comparable crosslink density and elastic response in the rubbery plateau.

The main difference between the two samples is observed at lower frequencies. The sample containing the dangling group exhibits faster relaxation dynamics, as shown by the earlier decrease of G' and increase of G''. The crossover frequency is shifted by approximately 0.5 decades toward higher frequencies, corresponding to a decrease in the characteristic relaxation time by a factor of 3. This observation is consistent with previous studies showing that dangling groups can enhance the dynamicity of boronic ester vitrimers by facilitating exchange reactions within the network.[38, 60]

The parallel behavior of G' and G'' in the terminal regime will be discussed in a further section.

4.6.5. Variability of rheological behavior

Apart from the terminal regime, which will be discussed in a following section, all experiments and figures presented above exhibited the expected rheological behavior of the vitrimer system and show good consistency between repeated measurements. However, similar experiments performed on independently prepared samples did not always lead to identical rheological responses, highlighting a limited reproducibility between samples.

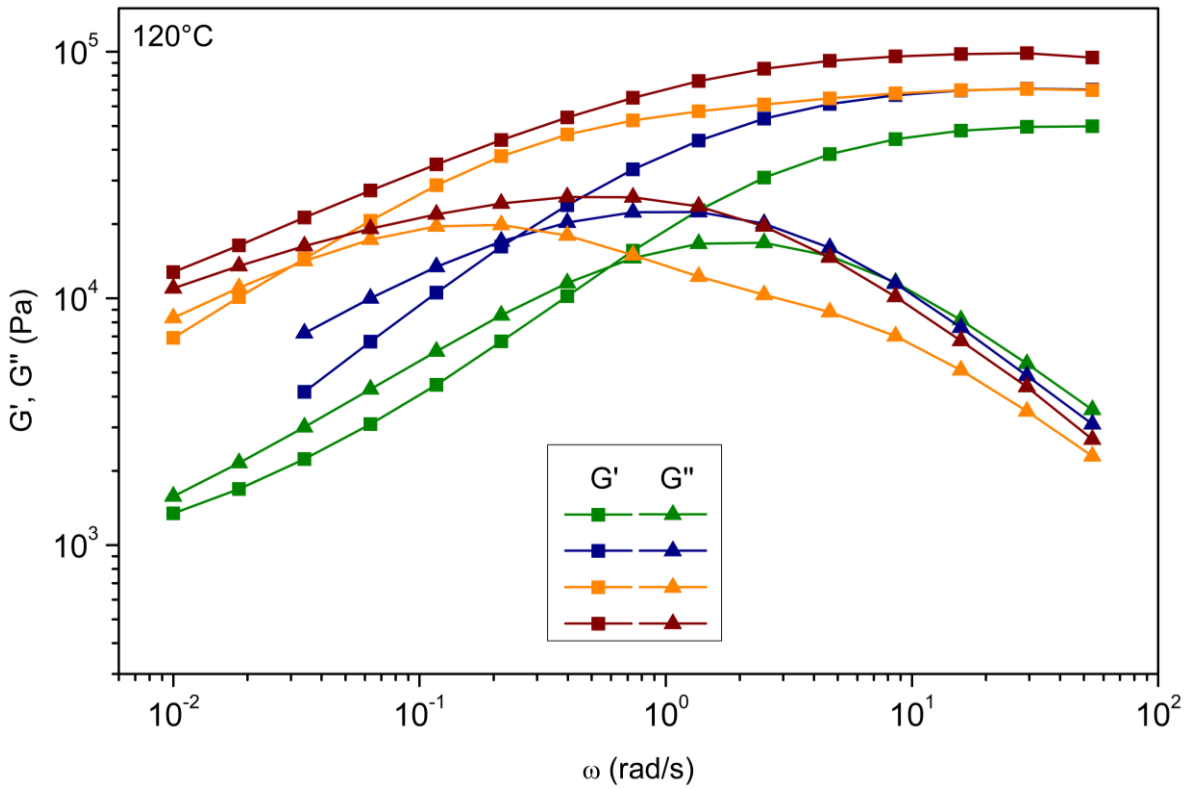

Figure 30 Frequency sweep of different DZDZ samples of the same composition at 120°C.

Figure 30 presents four frequency sweeps measured at 120°C on four DZDZ samples synthesized under identical conditions. Despite the identical preparation protocol, significant differences in the rheological behavior are observed. The plateau modulus varies from 50 kPa to 95 kPa, while the crossover frequency differs by two decades, indicating large variations in network dynamics. Differences in the terminal regime behavior are also observed between samples.

As these variations are obtained from samples expected to be equivalent, the rheological results discussed in the previous sections should be interpreted with caution. The observed variability suggests that small differences during synthesis or network formation can significantly affect the final material properties.

To better understand the origin of this limited reproducibility and potentially reduce the variability, several modifications of the photopolymerization conditions were investigated. Changing the solvent nature or solvent quantity did not significantly improve the reproducibility.

Increasing the temperature during the photopolymerization only helps with the dissolution of the monomers, but still exhibits a limited reproducibility. Similarly, the addition of a radical inhibitor after polymerization, intended to limit possible side reactions during heating, did not lead to noticeable improvements. Interestingly, variations in the initiator concentration appeared to have a more significant influence on the rheological behavior of the samples.

4.6.6. Impact of initiator amount

To better understand the origin of the rheological variability observed between samples, the influence of the initiator concentration on the polymer network was investigated. In radical polymerization systems, the initiator concentration directly affects the concentration of propagating radicals, which can influence both the polymer chain length and the dispersity of the network. These parameters are known to strongly affect the mechanical and rheological properties of vitrimer materials. [61, 62]

However, due to the synthetic route used in this work, the polymer network is systematically crosslinked during polymerization. As a result, it is not possible to isolate soluble non-crosslinked polymer chains for characterization by conventional techniques such as GPC or NMR. The effect of the initiator concentration therefore had to be studied indirectly through the rheological behavior of the resulting materials.

Figure 31 presents the rheological behavior of samples prepared with different initiator concentrations. The reference sample containing 0.5 wt% initiator exhibits a plateau modulus comparable to that of the system previously described in Figure 24 and starts to relax at a similar frequency. However, unlike the previous system, no G′-G″ crossover is observed.

Increasing the initiator concentration leads to higher network dynamicity, accompanied by a decrease in the modulus. These variations are likely related to changes in the polymer chain length. A higher initiator concentration increases the number of chain initiation events during polymerization, resulting in a larger number of shorter polymer chains. For the systems containing 1.5 and 2.5 wt% initiator, the stress relaxation behavior appears to be mainly governed by the boronic ester exchange reactions. In contrast, at lower initiator concentrations (0.05 and 0.5 wt%), the longer polymer chains are more susceptible to chain entanglements, which slows down the relaxation process.

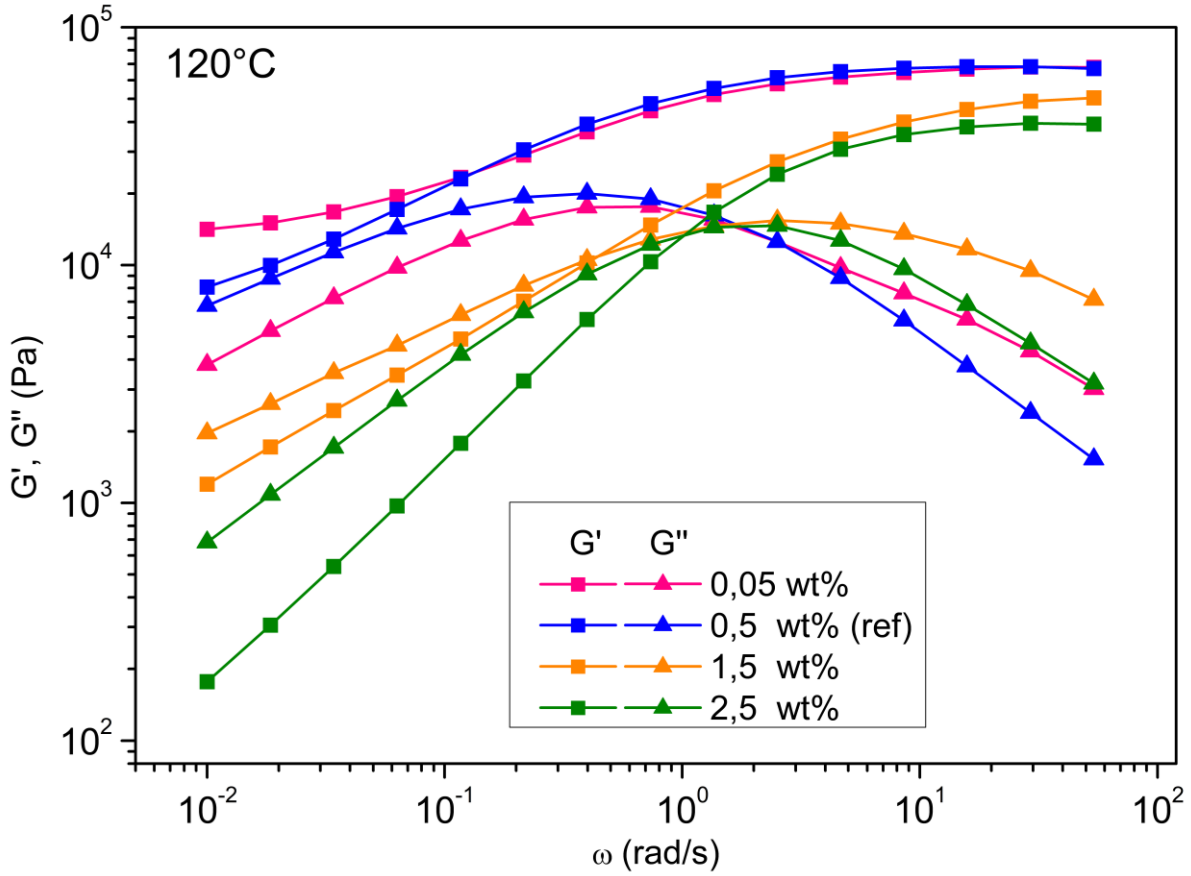

Figure 31 Frequency sweeps of different samples polymerized with various amounts of initiator at 120°C.

The objective of this experiment was not to determine the optimal initiator concentration. The goal was to show that the rheological variability does not mainly depend on the amount of initiator added to the formulation, but rather on the number of radicals effectively generated and involved during the polymerization. Because polymerization is carried out through a random radical mechanism under non-inert conditions, the effective radical concentration can easily vary from one synthesis to the other. Parameters such as oxygen, moisture, temperature variations, or small contaminations can influence the polymerization kinetics and modify the final network structure.

The terminal regime observed for samples containing 0.05 wt% and 0.5 wt% initiator will be discussed in the next section.

4.6.7. Terminal regime

During the rheological characterization, two distinct terminal behaviors were observed in the frequency sweep measurements.

Figure 32 shows the frequency sweep of a sample exhibiting a "classical" vitrimer behavior. At high frequencies, the material displays a rubbery plateau, followed by a crossover between G′ and G″ and the start of a terminal regime at low frequencies. Although the slopes in the terminal region do not perfectly correspond to the theoretical values expected for an ideal terminal regime (2 for G′ and 1 for G″), the overall viscoelastic behavior remains characteristic of a relaxation process. The slope deviations could result from incomplete network relaxation, chain entanglements or network heterogeneity leading to a broad distribution of relaxation times.

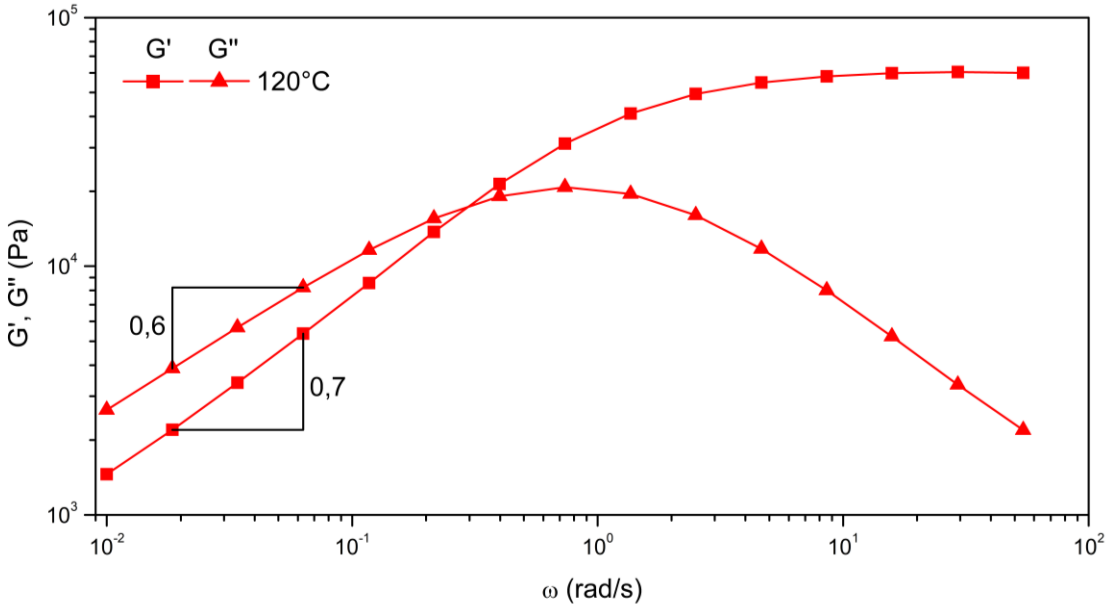

Figure 32 Frequency sweep of a DZDZ sample with a terminal regime.

In contrast, Figure 33 presents a sample with a different rheological response. After the rubbery plateau at high frequencies, no crossover between G′ and G″ is observed. Instead, both moduli decrease almost parallel to each other with slopes close to 0,5. At lower frequencies, the emergence of a second plateau can be observed.

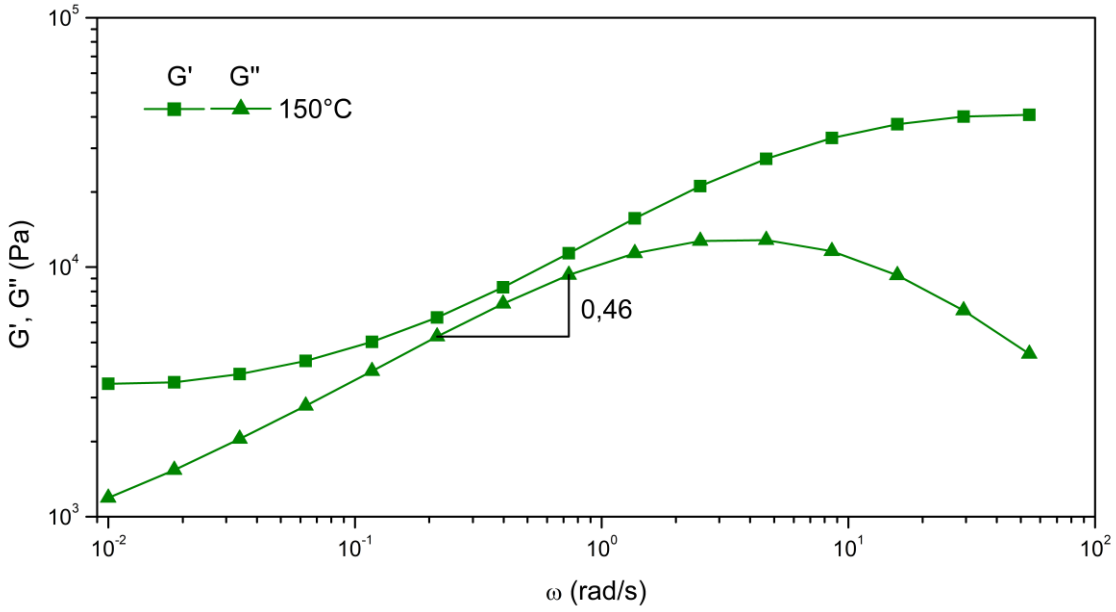

Figure 33 Frequency sweep of a DZDZ sample without terminal regime.

The origin of this second plateau remains unclear, but two main hypotheses can be proposed. The first is the presence of chain entanglements which could slow down chain relaxation and maintain an elastic contribution at low frequencies. The second hypothesis is the formation of permanent covalent bonds between polymer chains. Such irreversible crosslinks may originate either from radical side reactions occurring during photopolymerization or from thermally induced reactions during prolonged heating. Previous experiments performed within the research group have already shown the formation of permanent crosslinks after extended heating of PEGMA homopolymers.

All samples studied by rheological measurements exhibited terminal behavior comparable to either Figure 32 or Figure 33. However, no clear correlation could be established between the observed rheological behavior and parameters such as sample composition, salt concentration, initiator content, modulus, or apparent network dynamics.

Once a sample exhibited one of the two rheological behaviors, it retained the same behavior through all measurements. Changing experimental conditions, such as temperature, did not induce any transition between the two behaviors. This suggests that the observed rheological response is likely determined during photopolymerization. Further investigations will therefore be required to identify the origin of these different behaviors.

4.6.8. Addition of Li salt

All previous results were obtained without lithium salt, but for battery purposes the addition of Li salt is necessary. Before analyzing the conductivity of the samples, the rheology of the samples containing Li salt will be evaluated.

For the addition of the Li salt, two methods will be used: the swelling of a Li salt solution after the polymerization (Figure 34 A) or the dissolution of the salt in the bulk monomer solution before polymerization (Figure 34 B).

$LiClO_4$ was selected due to its good solubility in PEG-based matrices and common organic solvents, its relatively easy handling compared to moisture-sensitive salts such as LiTFSI, and its ability to provide sufficient ionic dissociation in polymer electrolytes.

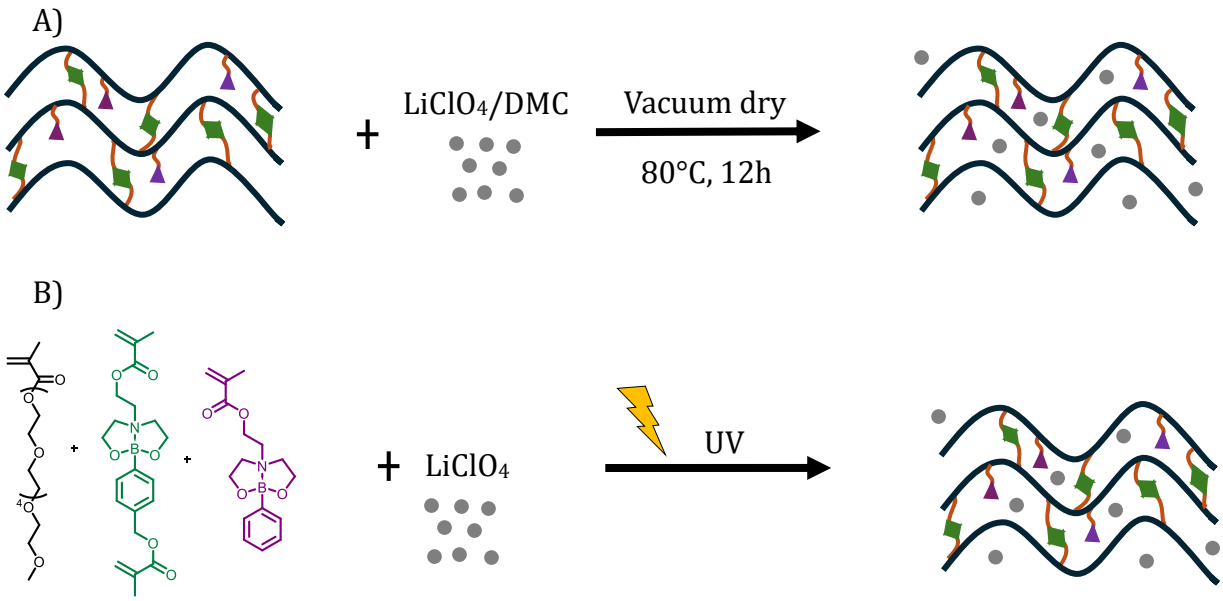

Figure 34 Addition of lithium salt. A) Swelling after polymerization. B) Addition before polymerization.

The mass of $LiClO_4$ was determined from the number of EO units in the polymer, using an EO:Li^+ molar ratio of 35:1. Such ratios are commonly reported for PEG/PEO-based polymer electrolytes and are generally associated with high ionic conductivities.[63]

Figure 35 shows different frequency sweep measurements on different samples. Compared to the salt-free systems, the incorporation of $LiClO_4$ shifts the G′-G″ crossover toward higher frequencies and accelerates the relaxation process, indicating an increase in the dynamicity of the vitrimer network. This effect has been discussed in the introduction (2.3.2 Salt impact on vitrimers). The Lewis acid-base interaction between the boron and the anion favors the opening of the dioxazaborocane cycle, which accelerates the boronic ester exchange.

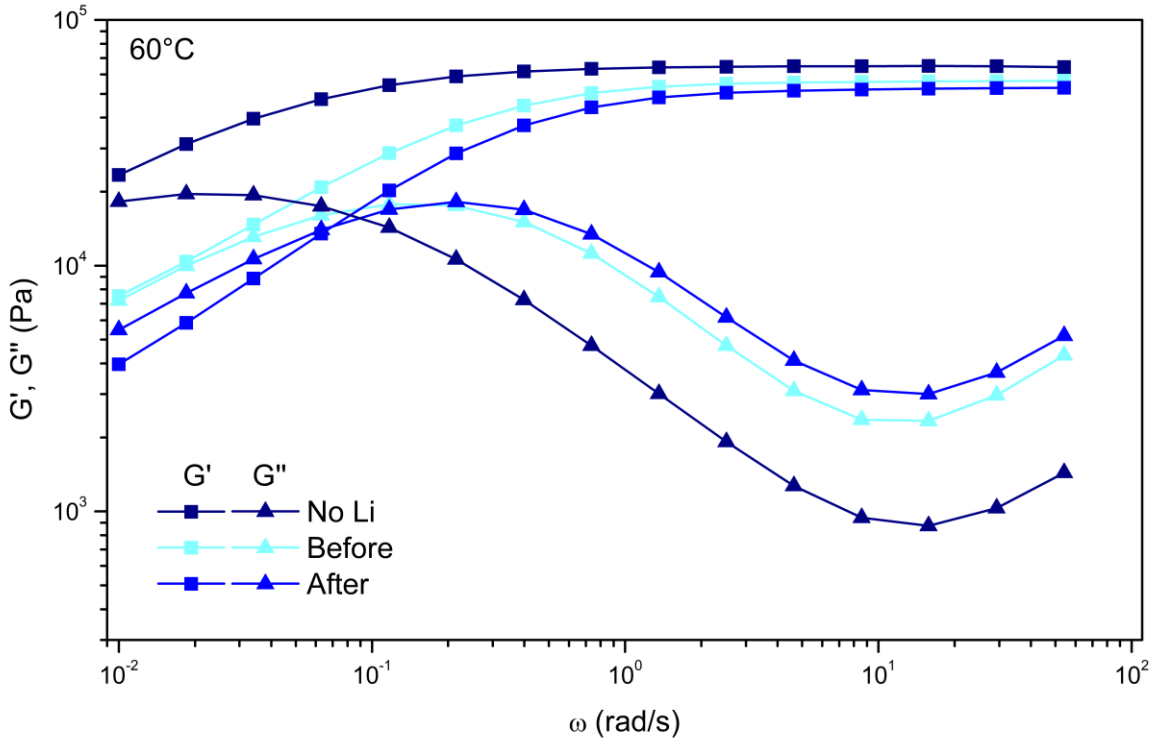

Figure 35 Frequency sweep at 60°C of different DZDZ samples with and without lithium, and with different lithium addition processes.

Data also shows a different behavior depending on the way of adding Li salt, with slower dynamics when the salt is present during the photopolymerization. This slower behavior could be attributed to the impact of the ions on the propagating radicals. Literature shows that Li^+ can coordinate with the propagating methacrylate radical (C=O - Li^+ interactions), giving a stabilized radical. This leads to a slower reaction, lower termination and longer chains.[64] As discussed earlier, chain length impacts the rheological behavior of the network, with longer chains having lower dynamics. [61]

The observed differences between the two salt incorporation methods may also be influenced by the limited reproducibility of the polymerization process. As discussed previously, independently prepared samples can exhibit significant variations in their rheological behavior. Consequently, the faster relaxation observed for the sample in which $LiClO_4$ was added after polymerization may not be solely related to the incorporation method itself. Similarly, the differences in plateau modulus could also originate from the variability between samples. Due to this limited reproducibility, the observed trends should be considered as indications rather than definitive conclusions, and the results should not be overinterpreted.

4.7. Conductivity

Rheological measurements provided information on the dynamic behavior of the vitrimer networks. The next step was therefore to evaluate their ionic conductivity, which is a key parameter for their potential application as solid polymer electrolytes.

Figure 36 shows the conductivity of two systems prepared using different $LiClO_4$ incorporation methods. No significant difference in conductivity is observed between the two approaches. Although differences were detected in the rheological behavior, they do not appear to affect the ionic conductivity of the materials.

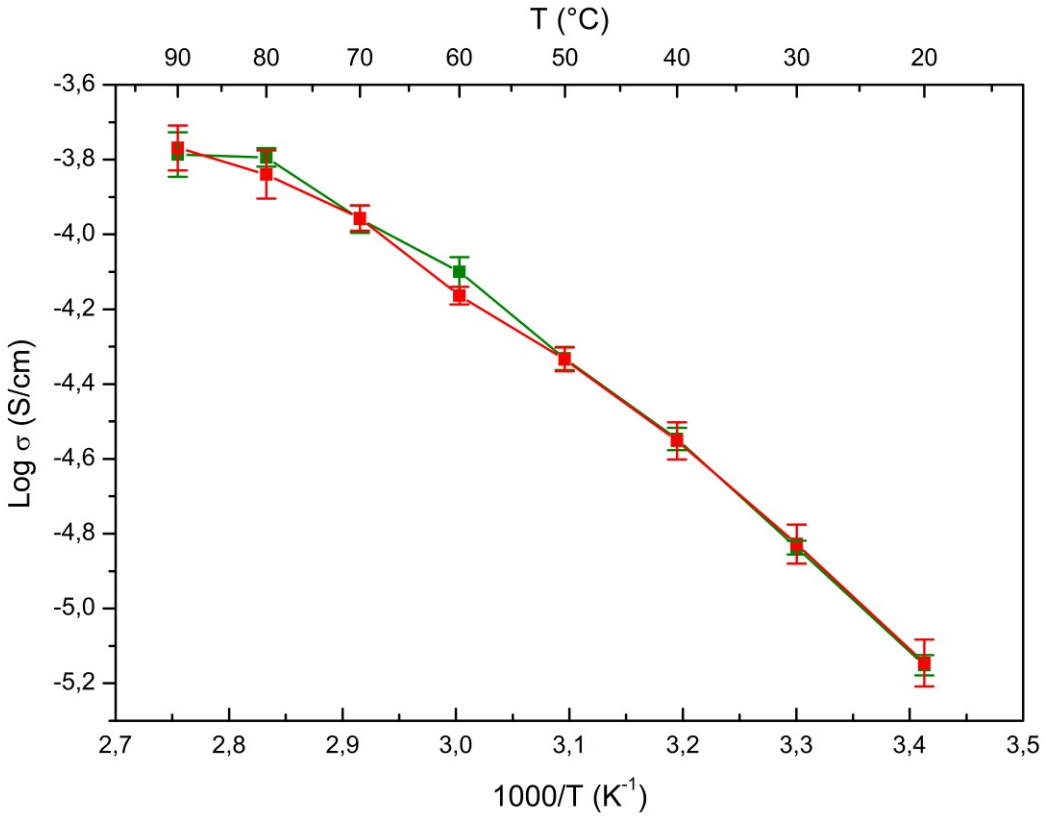

Figure 36 Arrhenius plot of the conductivity of DZ sample with the addition of lithium salt before or after polymerization. Error bars correspond to the standard deviation of three samples.

Figure 37 and Table 4 compare the ionic conductivity of the DZDZ network with that of the two DZ systems. A clear difference in conductivity is observed between the two network architectures. At 20 °C, the conductivity of the DZDZ system is approximately five times lower than that of the DZ systems, although this difference becomes less pronounced as the temperature increases.

The difference observed at low temperatures can be attributed to the different EO content of the networks. The DZ system contains 95 mol% of PEGMA, whereas the DZDZ system contains only

90 mol% of PEGMA. Since EO units play a major role in lithium-ion solvation and transport, the lower EO content of the DZDZ network likely contributes to its reduced conductivity.

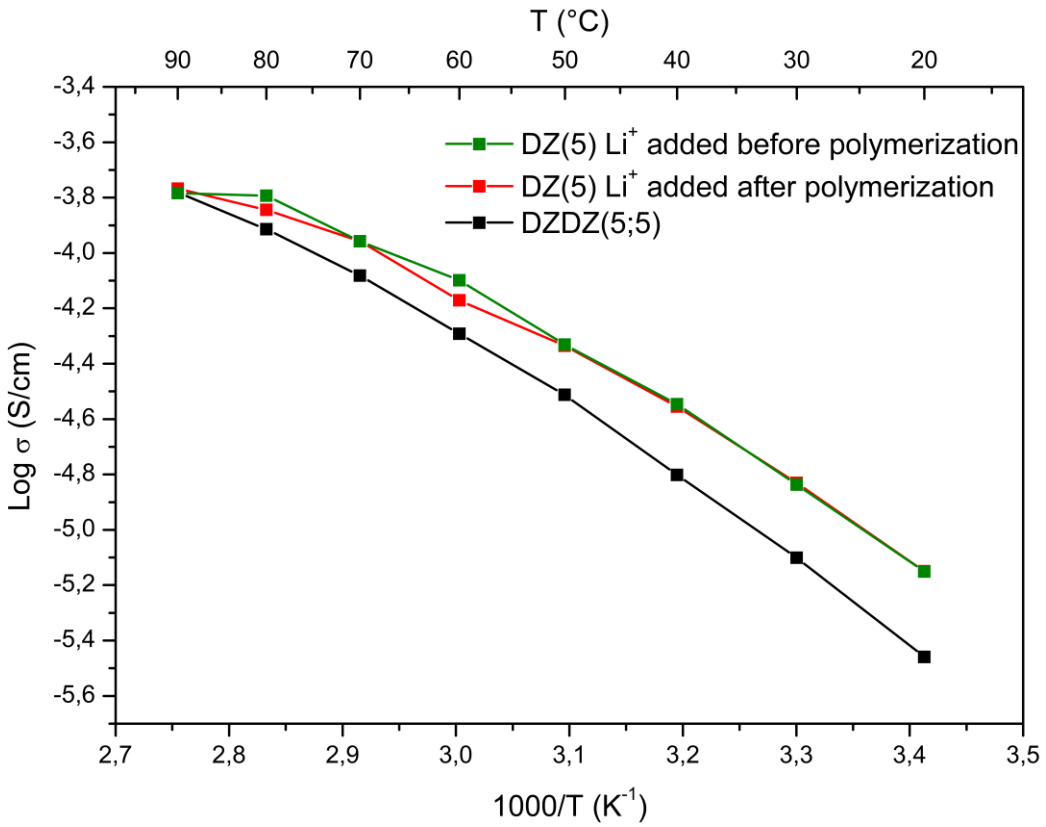

Figure 37 Arrhenius plot of the conductivity of DZ and DZDZ samples.

Network	Ionic conductivity at 20°C (S.cm^{-1})	Ionic conductivity at 60°C (S.cm^{-1})	Activation energy (kJ.mol^{-1})
DZ: Li$^+$ added before polym.	7.1*10^{-6}	8.1*10^{-5}	50
DZ: Li$^+$ added after polym.	7.2*10^{-6}	6.8*10^{-5}	48
DZDZ	3.5*10^{-6}	5.1*10^{-5}	57

Table 4 Ionic conductivities at 20°C and 60°C and activation energy (Arrhenius fit between 20°C and 60°C) for DZDZ and DZ samples.

Although the conductivities remain below those of liquid electrolytes, they are comparable to values reported for vitrimer electrolytes (10^{-3} to 10^{-5} S.cm^{-1} at 60°C)[40], highlighting the potential of these networks for solid polymer electrolyte applications.

All samples exhibit an Arrhenius behavior between 20 and 50–60 °C. At higher temperatures, the conductivity curves progressively deviate from linearity and tend to follow a Vogel–Fulcher–Tammann (VFT) behavior. This deviation suggests that segmental mobility is no longer the main limiting factor for ion transport. As a result, the influence of the EO content becomes less pronounced, leading to a progressive convergence of the conductivity curves for the DZ and DZDZ systems. At these temperatures, ion transport becomes increasingly influenced by the concentration of mobile charge carriers and the availability of coordination sites, which may also explain the reduced temperature dependence of the conductivity.[65]

In the linear Arrhenius region (20–60 °C), the activation energy was calculated from the slope of the linear fit. As shown in Table 4, values ranging from 48 to 57 $kJ.mol^{-1}$ were obtained, which is consistent with the literature values for similar PEG-based polymer electrolytes.[66]

4.8. Self-healing

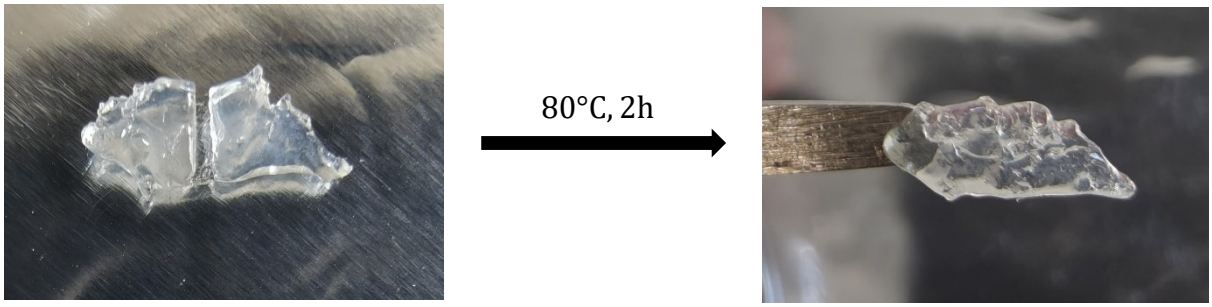

Figure 38 Pictures of a cut and healed DZDZ polymer.

Figure 38 illustrates the self-healing behavior of a DZDZ polymer network. The sample was first cut into two separate pieces and then brought back into contact. After being kept at 80 °C for 2 h, the two pieces merged into a single sample that could be handled without separating. Similar healing behavior was observed for all systems, both DZDZ and DZ networks, with and without $LiClO_4$.

It should be noted that this evaluation is purely qualitative and based on visual observations. No mechanical characterization, such as tensile testing, was performed to quantify the healing efficiency. Therefore, the self-healing properties of these materials should be interpreted with caution.

4.9. DSC

After conductivity measurements, the thermal properties of the materials were investigated by DSC and TGA. These analyses were performed to assess their suitability for battery applications in terms of thermal transitions and thermal stability.

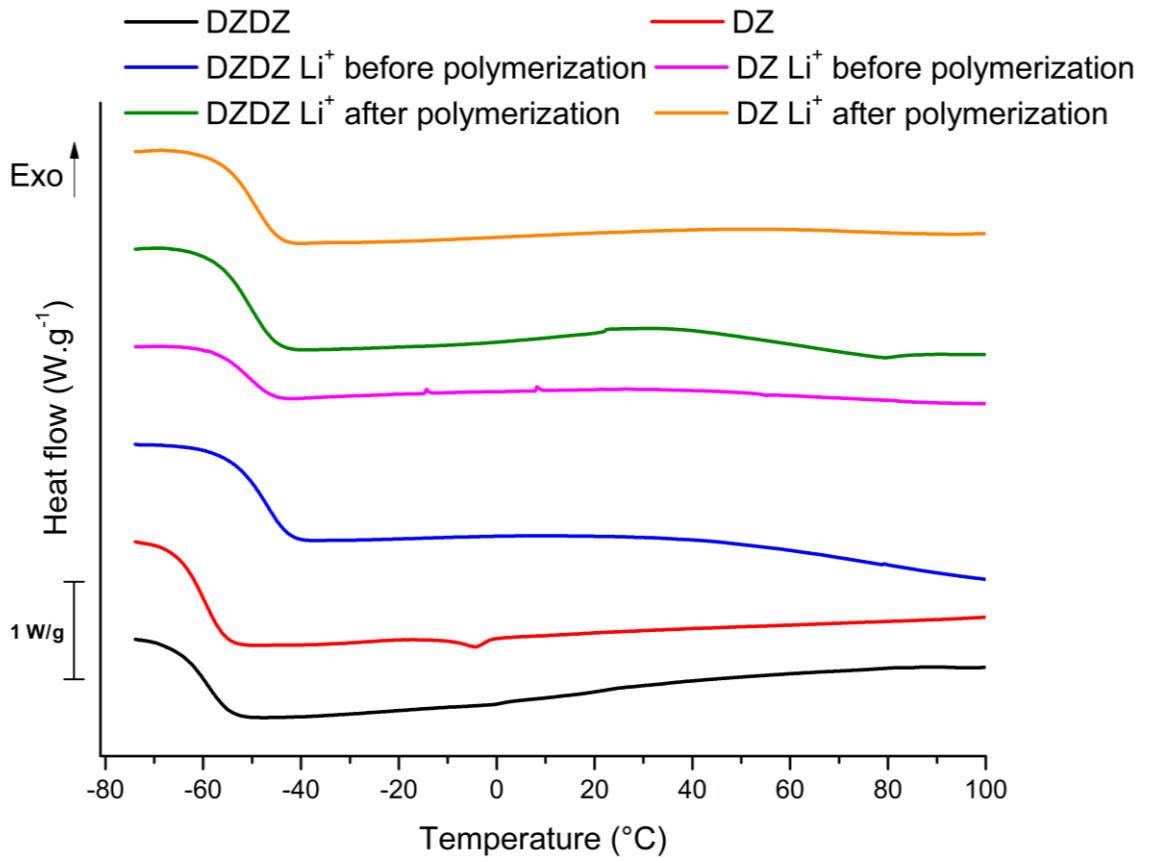

Figure 39 DSC thermogram (2nd heating scan) of the DZDZ and DZ networks with and without lithium salt.

Network	Addition of Li	T_g (°C)
DZ	After	-49
DZDZ	After	-50
DZ	Before	-50
DZDZ	Before	-48
DZ	No Li	-59
DZDZ	No Li	-59

Table 5 T_g of the DZDZ and DZ networks with and without lithium salt.

Figure 39 shows that all samples remain well above their glass transition temperature and in the amorphous state throughout the temperature ranges used for both rheological and conductivity measurements. Therefore, neither network dynamics nor ionic transport are expected to be limited by glassy behavior or crystallinity.

In Table 5, it can be observed that both samples without lithium salt have a lower glass transition (-59°C) compared to samples containing $LiClO_4$ (-50°C). This behavior is commonly observed in PEG-based polymer electrolytes and is attributed to the coordination of Li^+ cations with the ether oxygen atoms of the PEGMA chains. These ion–ether interactions restrict the segmental mobility of the polymer chains, leading to a stiffer polymer network and therefore to a higher T_g.[42, 67]

The other minor variations observed in the DSC thermograms are considered negligible and will therefore not be further discussed in this work, as they may originate from experimental or instrumental fluctuations.

4.10. TGA

The TGA curves and their corresponding first derivatives are presented in Figure 40 and Figure 41, respectively. The main thermal degradation parameters are summarized in Table 6, including the degradation temperature at 5% weight loss (T_d 5%) and the temperature corresponding to the maximum degradation rate, which reflects where most of the polymer network degrades.

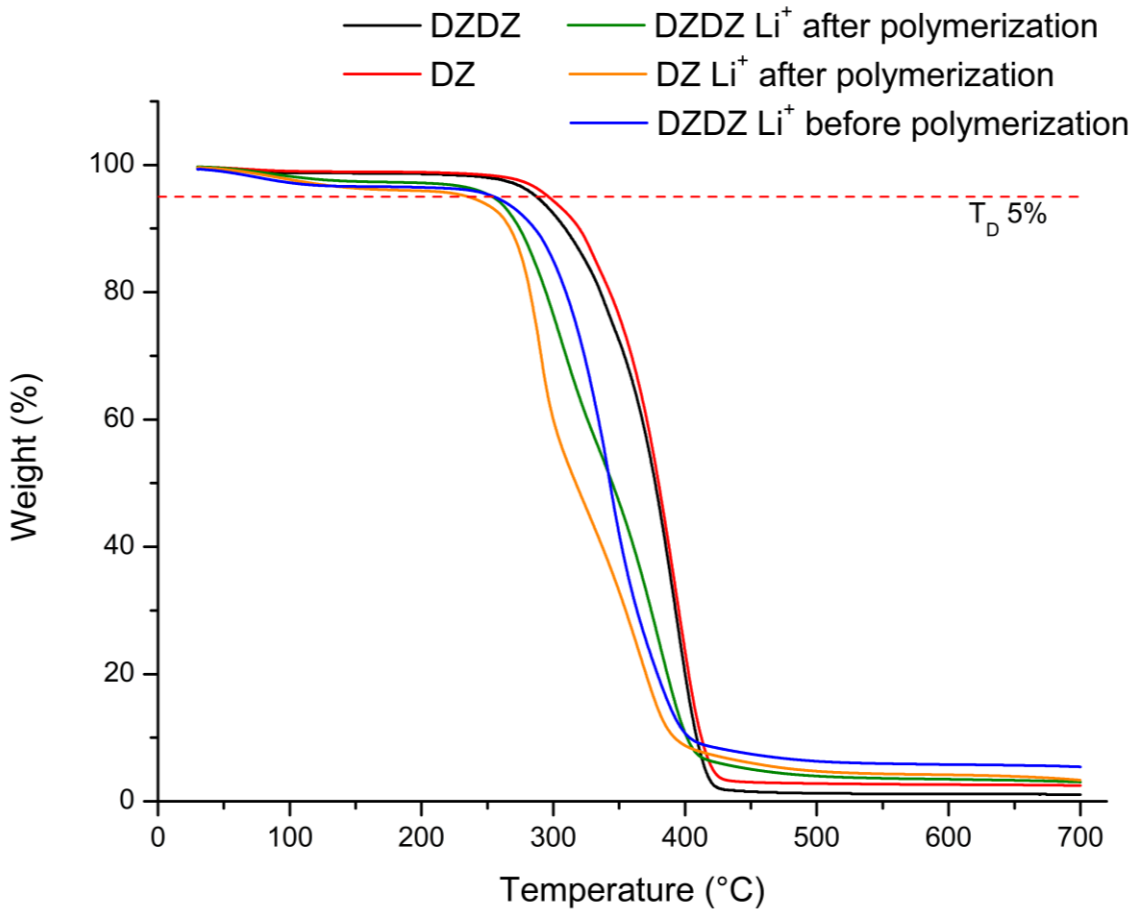

Figure 40 TGA curves of DZDZ and DZ networks with and without lithium salt.

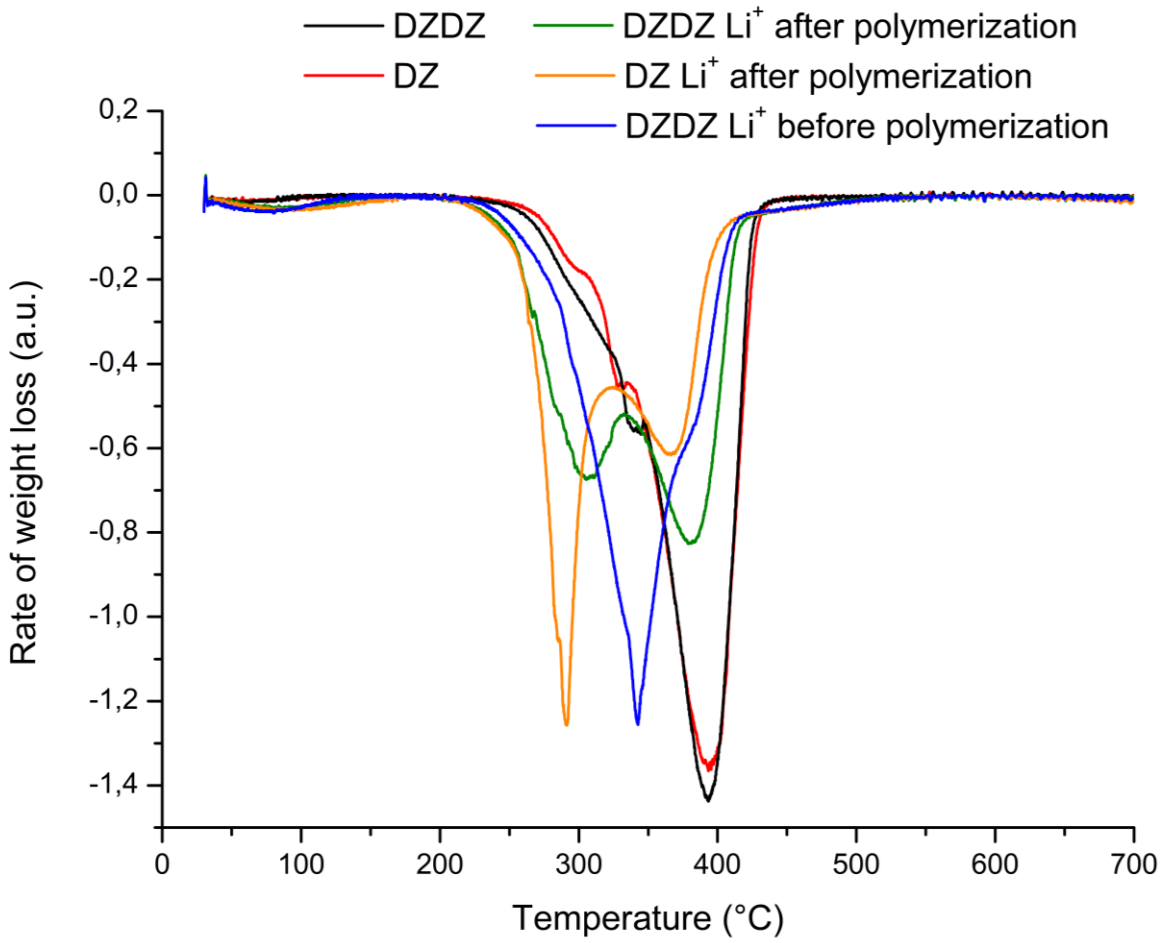

Figure 41 TGA first derivative, showing the maximum rate of weight loss as function of temperature for DZDZ and DZ networks with and without lithium salt.

Network	Addition of Li	T_D 5% (°C)	T at maximum rate loss (°C)
DZDZ	No Li	287	394
DZ	No Li	296	395
DZDZ	Before	255	342 375
DZDZ	After	253	305 380
DZ	After	245	291 363

Table 6 T_D 5% and temperature at maximum rate loss of the DZDZ and DZ networks with and without lithium salt.

The results indicate that the thermal stability of the DZDZ and DZ networks without lithium salt is very similar, with no significant differences observed in either the degradation temperatures or the degradation profiles.

For the lithiated samples, a small initial mass loss of approximately 2–3% is observed between 80 °C and 120 °C. This is attributed to the evaporation of absorbed water. Although the samples were dried before measurement, $LiClO_4$ is hygroscopic and can easily reabsorb moisture during sample preparation and handling before the TGA measurements.

The addition of $LiClO_4$ significantly modifies the degradation behavior of the networks (Figure 41). While the salt-free samples exhibit a single degradation step around 400 °C, all lithiated samples show two distinct degradation events, one between 300 °C and 350 °C and a second between 360 °C and 380 °C. The literature attributes this earlier decomposition to the coordination of Li^+ ions with ethylene oxide units, which promotes degradation at lower temperatures. The oxidizing nature of the perchlorate anion may also contribute to this effect. [68, 69] Small differences in the degradation profiles are observed depending on the salt incorporation method. The origin of these variations remains unclear and cannot be explained based on the available experimental data.

Despite these changes in the degradation profile, all samples exhibit a T_d 5% above 240 °C, which is sufficient thermal stability for their intended application as SPEs in batteries.

5. Outlook and conclusion

The objective of this work was to synthesize and characterize boronic ester vitrimer electrolytes combining dynamic properties and good ionic conductivity. Two vitrimer systems based on PEGMA and dioxazaborocane crosslinkers were investigated, with and without the incorporation of dangling groups and $LiClO_4$.

Overall, the studied materials showed promising properties. Rheological analyses confirmed the vitrimer nature of all networks. The incorporation of both the dangling group and $LiClO_4$ led to faster network dynamics, indicating that these modifications facilitate bond exchange and enhance chain mobility. The networks also exhibited self-healing behavior, further confirming the presence of an efficient dynamic covalent network.

From the electrolyte perspective, the materials displayed encouraging ionic conductivities. The highest conductivity reached $8.1*10^{-5}$ $S.cm^{-1}$ at 60 °C, placing these materials in the upper range of conductivities typically reported for solid polymer electrolytes.

Despite these promising results, the employed synthetic approach presents important limitations. The direct photopolymerization of multifunctional monomers under non-inert conditions leads to networks with limited reproducibility. Small variations during polymerization can result in significant differences in the final material properties. In addition, the direct formation of a crosslinked network restricts the use of several characterization techniques such as GPC and NMR.

Future work should therefore focus on improving the synthetic methodology. One possible strategy would be to first prepare well-defined linear polymers using a controlled polymerization technique and then introduce the boronic ester crosslinks. Such approach could improve reproducibility, facilitate structural characterization, and provide better control over network architecture.

Finally, although both rheological and conductivity properties were investigated, no clear correlation could be established between network dynamics and ionic conductivity. The limited reproducibility of the rheological behavior currently prevents a systematic study of this relationship. A better understanding of the factors controlling network dynamics could allow the preparation of vitrimer networks exhibiting different dynamicity. These materials could then be used to study how network dynamicity affects ionic conductivity. Establishing this relationship would provide valuable insights into the transport mechanisms operating in vitrimer electrolytes and could support the development of more efficient electrolyte materials.

6. References

(1) Rehman, S.; Al-Hadhrami, L. M.; Alam, M. M. Pumped hydro energy storage system: A technological review. *Renew. Sustain. Energy Rev.* **2015**, *44*, 586–598. DOI: 10.1016/j.rser.2014.12.040.

(2) Badwal, S. P.; Giddey, S. S.; Munnings, C.; Bhatt, A. I.; Hollenkamp, A. F. Emerging electrochemical energy conversion and storage technologies. *Front Chem* **2014**, *2*, 79. DOI: 10.3389/fchem.2014.00079.

(3) Stampatori, D.; Raimondi, P. P.; Noussan, M. Li-Ion Batteries: A Review of a Key Technology for Transport Decarbonization. *Energies* **2020**, *13* (10), 2638. DOI: 10.3390/en13102638.

(4) Requia, W. J.; Mohamed, M.; Higgins, C. D.; Arain, A.; Ferguson, M. How clean are electric vehicles? Evidence-based review of the effects of electric mobility on air pollutants, greenhouse gas emissions and human health. *Atmos. Environ.* **2018**, *185*, 64–77. DOI: 10.1016/j.atmosenv.2018.04.040.

(5) Ngoy, K. R.; Lukong, V. T.; Yoro, K. O.; Makambo, J. B.; Chukwuati, N. C.; Ibegbulam, C.; Eterigho-Ikelegbe, O.; Ukoba, K.; Jen, T.-C. Lithium-ion batteries and the future of sustainable energy: A comprehensive review. *Renew. Sustain. Energy Rev.* **2025**, *223*, 115971. DOI: 10.1016/j.rser.2025.115971.

(6) Goodenough, J. B.; Park, K. S. The Li-ion rechargeable battery: a perspective. *J. Am. Chem. Soc.* **2013**, *135* (4), 1167–1176. DOI: 10.1021/ja3091438.

(7) Wulandari, T.; Fawcett, D.; Majumder, S. B.; Poinern, G. E. J. Lithium-based batteries, history, current status, challenges, and future perspectives. *Battery Energy* **2023**, *2* (6). DOI: 10.1002/bte2.20230030.

(8) Younesi, R.; Veith, G. M.; Johansson, P.; Edström, K.; Vegge, T. Lithium salts for advanced lithium batteries: Li–metal, Li–O2, and Li–S. *Energy Environ. Sci.* **2015**, *8* (7), 1905–1922. DOI: 10.1039/c5ee01215e.

(9) Asenbauer, J.; Eisenmann, T.; Kuenzel, M.; Kazzazi, A.; Chen, Z.; Bresser, D. The success story of graphite as a lithium-ion anode material – fundamentals, remaining challenges, and recent developments including silicon (oxide) composites. *Sustain. Energy Fuels* **2020**, *4* (11), 5387–5416. DOI: 10.1039/d0se00175a.

(10) Koech, A. K.; Mwandila, G.; Mulolani, F.; Mwaanga, P. Exploring the anode materials for lithium-ion batteries: A review. *Next Res.* **2025**, *2* (3), 100442. DOI: 10.1016/j.nexres.2025.100442.

(11) Koech, A. K.; Mwandila, G.; Mulolani, F.; Mwaanga, P. Lithium-ion battery fundamentals and exploration of cathode materials: A review. *S. Afr. J. Chem. Eng.* **2024**, *50*, 321–339. DOI: 10.1016/j.sajce.2024.09.008.

(12) Tarascon, J.-M.; Armand, M. Issues and challenges facing rechargeable lithium batteries. *Nature* **2001**, *414*, 359–367. DOI: 10.1038/35104644.

(13) Finkelstein, S. H.; Ricci, M.; Botticher, T.; Schmidt-Rohr, K. How lithium-ion batteries work conceptually: thermodynamics of Li bonding in idealized electrodes. *Phys. Chem. Chem. Phys.* **2024**, *26* (36), 24157–24171. DOI: 10.1039/d4cp00818a.

(14) Itani, K.; De Bernardinis, A. Review on New-Generation Batteries Technologies: Trends and Future Directions. *Energies* **2023**, *16* (22), 7530. DOI: 10.3390/en16227530.

(15) Gao, X. G.; Zhou, Y.-N.; Han, D.; Zhou, J.; Zhou, D.; Tang, W.; Goodenough, J. B. Thermodynamic Understanding of Li-Dendrite Formation. *Joule* **2020**, *4* (20), 1864–1879. DOI: 10.1016/j.joule.2020.06.016.
(16) Wang, Q.; Liu, B.; Shen, Y.; Wu, J.; Zhao, Z.; Zhong, C.; Hu, W. Confronting the Challenges in Lithium Anodes for LithiumMetal Batteries. *Adv. Sci.* **2021**, *8* (17), 2101111. DOI: 10.1002/advs.202101111.
(17) Cheng, X.-B.; Zhang, R.; Zhao, C.-Z.; Zhang, Q. Toward Safe Lithium Metal Anode in Rechargeable Batteries: A Review. *Chem. Rev.* **2017**, *117* (15), 10403–10473. DOI: 10.1021/acs.chemrev.7b00115.
(18) Su, L.; Manthiram, A. Lithium-Metal Batteries via Suppressing Li Dendrite Growth and Improving Coulombic Efficiency. *Small Struct.* **2022**, *3* (10), 2200114. DOI: 10.1002/sstr.202200114.
(19) Liu, C.; Wang, T.; Yu, J.; Li, S.; Ma, H.; Liu, X. Review of the Developments and Difficulties in Inorganic Solid-State Electrolytes. *Materials* **2023**, *16* (6), 2510. DOI: 10.3390/ma16062510.
(20) Xue, Z.; He, D.; Xie, X. Poly(ethylene oxide)-based electrolytes for lithium-ion batteries. *J. Mater. Chem. A* **2015**, *3*, 19218–19253. DOI: 10.1039/C5TA03471J.
(21) Bannister, D.; Davies, G.; Ward, I.; McIntyre, J. Ionic conductivities of poly(methoxy polyethylene glycol monomethacrylate) complexes with LiSO3CH3. *Polymer* **1984**, *25* (11), 1600–1602. DOI: 10.1016/0032-3861(84)90152-6.
(22) Wang, X.; Song, Z.; Wu, H.; Nie, J.; Feng, W.; Yu, H.; Huang, X.; Armand, M.; Zhou, Z.; Zhang, H. Unprecedented Impact of Main Chain on Comb Polymer Electrolytes Performances. *ChemElectroChem* **2022**, *9* (4). DOI: 10.1002/celc.202101590.
(23) Casas-Cabanas, M.; Palacín, R. Challenges ahead in the development of solid-state batteries. *J. Power Sources* **2025**, *659*, 238355. DOI: 10.1016/j.jpowsour.2025.238355.
(24) Blue Solutions. https://www.blue-solutions.com/about-us/ (accessed 12/02/2026).
(25) BlueBus. https://www.bluebus.fr/bluebus-12-m (accessed 12/02/2026).
(26) Deschamps, M.; Lecuyer, M.; Bouchet, R.; Pavlenko, E.; Lassagne, A.; Gigmes, D.; Ferrand, A.; Trang, P. Polymer electrolyte for a lithium metal battery having improved performance. WO/2020/109711, 2019.
(27) Chen, T.; Reddy, N. P.; Li, M. Enhancing Solid-State Li-Ion Batteries with MOF-Polymer Composite Electrolytes-Effect Mechanisms and Interface Engineering. *Gels* **2025**, *11* (12), 946. DOI: 10.3390/gels11120946.
(28) Niu, C.; Liu, J.; Chen, G.; Liu, C.; Qian, T.; Zhang, J.; Cao, B.; Shang, W.; Chen, Y.; Han, J.; et al. Anion-regulated solid polymer electrolyte enhances the stable deposition of lithium ion for lithium metal batteries. *J. Power Sources* **2019**, *417*, 70–75. DOI: 10.1016/j.jpowsour.2019.02.004.
(29) Bouchet, R.; Deschamps, M. Lithium metal polymer battery having a high energy density. WO 2017/158310 A1, 2017.
(30) Zheng, J.; Png, Z. M.; Ng, S. H.; Tham, G. X.; Ye, E.; Goh, S. S.; Loh, X. J.; Li, Z. Vitrimers: Current research trends and their emerging applications. *Mater. Today* **2021**, *51*, 586–625. DOI: 10.1016/j.mattod.2021.07.003.
(31) Morici, E.; Dintcheva, N. T. Recycling of Thermoset Materials and Thermoset-Based Composites: Challenge and Opportunity. *Polymers* **2022**, *14* (19), 4153. DOI: 10.3390/polym14194153.

(32) Sun, M.; Felsenthal, L. M.; Kim, S.; Choi, E. Y.; Reed, L. J.; Elling, B. R.; Dichtel, W. R. Covalent Adaptable Networks: Reprocessable Cross-Linked Polymers. *Chem. Rev.* **2026**, *126* (3), 1829–1948. DOI: 10.1021/acs.chemrev.4c00994.
(33) Denissen, W.; Winne, J. M.; Du Prez, F. E. Vitrimers: permanent organic networks with glass-like fluidity. *Chem. Sci.* **2016**, *7* (1), 30–38. DOI: 10.1039/c5sc02223a.
(34) Van Zee, N. J.; Nicolaÿ, R. Vitrimers: Permanently crosslinked polymers with dynamic network topology. *Prog. Polym. Sci.* **2020**, *104*, 101233. DOI: 10.1016/j.progpolymsci.2020.101233.
(35) Teotonico, J.; Mantione, D.; Ballester-Bayarri, L.; Ximenis, M.; Sardon, H.; Ballard, N.; Ruipérez, F. A combined computational and experimental study of metathesis and nucleophile-mediated exchange mechanisms in boronic ester-containing vitrimers. *Polym. Chem.* **2024**, *15* (3), 181–192. DOI: 10.1039/d3py01047c.
(36) Röttger, M.; Domenech, T.; van der Weegen, R.; Breuillac, A.; Nicolaÿ, R.; Leibler, L. High-performance vitrimers from commodity thermoplastics through dioxaborolane metathesis. *Science* **2017**, *356, 6333*, 62–65. DOI: 10.1126/science.aah5281.
(37) Zhang, X.; Wang, S.; Jiang, Z.; Li, Y.; Jing, X. Boronic Ester Based Vitrimers with Enhanced Stability via Internal Boron–Nitrogen Coordination. *J. Am. Chem. Soc.* **2020**, *142* (52), 21852–21860. DOI: 10.1021/jacs.0c10244.
(38) Quinteros-Sedano, A.; Le Besnerais, B.; Van Zee, N.; Nicolaÿ, R. Exploiting Dioxazaborocane Chemistry for Preparing Elastomeric Vitrimers with Enhanced Processability and Mechanical Properties. *Chem. Mater.* **2025**, *37* (5), 2058–2070. DOI: 10.1021/acs.chemmater.5c00154.
(39) Rezayani, M.; Sharif, F.; Makki, H. Dynamic bonds transform ion transport mechanisms in polymeric covalent adaptable networks. *Mater. Horiz.* **2025**, *12* (22), 9643–9652. DOI: 10.1039/d5mh00433k.
(40) Katcharava, Z.; Marinow, A.; Binder, W. H. Vitrimeric electrolytes - overview and perspectives. *Chem. Commun.* **2025**, *61* (16), 3250–3270. DOI: 10.1039/d4cc05428h.
(41) Wang, X.; Wang, M.; Chen, H.; Zhang, Y.; Niu, B.; Tian, L.; Long, D. Dynamically reversible cross-linked polymer electrolytes with highly ionic conductivity for dendrite-free lithium metal batteries. *Chem. Eng. J.* **2024**, *496*. DOI: 10.1016/j.cej.2024.153830.
(42) Jang, S.; Hernandez Alvarez, E. I.; Chen, C.; Jing, B. B.; Shen, C.; Braun, P. V.; Schleife, A.; Schroeder, C. M.; Evans, C. M. Control of Lithium Salt Partitioning, Coordination, and Solvation in Vitrimer Electrolytes. *Chem. Mater.* **2023**, *35* (19), 8039–8049. DOI: 10.1021/acs.chemmater.3c01353.
(43) Jang, S.; Tsai, R.-B.; Schroeder, C. M.; Evans, C. M. Anion and Cation Size Effects on Viscoelasticity and Ion Transport of Imine Vitrimer Electrolytes. *Chem. Mater.* **2025**, *37* (18), 7037–7048. DOI: 10.1021/acs.chemmater.5c00991.
(44) Jing, B. B.; Evans, C. M. Catalyst-Free Dynamic Networks for Recyclable, Self-Healing Solid Polymer Electrolytes. *J. Am. Chem. Soc.* **2019**, *141* (48), 18932–18937. DOI: 10.1021/jacs.9b09811.
(45) Zhang, L.; Zhang, P.; Chang, C.; Guo, W.; Guo, Z. H.; Pu, X. Self-Healing Solid Polymer Electrolyte for Room-Temperature Solid-State Lithium Metal Batteries. *ACS Appl. Mater. Interfaces* **2021**, *13* (39), 46794–46802. DOI: 10.1021/acsami.1c14462.
(46) Sun, Z.; Wu, J.; Yuan, H.; Lan, J.; Yu, Y.; Zhu, Y.; Yang, X. Self-healing polymer electrolyte for long-life and recyclable lithium-metal batteries. *Mater. Today Energy* **2022**, *24*, 100939. DOI: 10.1016/j.mtener.2021.100939.

(47) Deivanayagam, R.; Shahbazian-Yassar, R. Electrochemical Methods and Protocols for Characterization of Ceramic and Polymer Electrolytes for Rechargeable Batteries. *Batteries Supercaps* **2021**, *4* (4), 596–606. DOI: 10.1002/batt.202000221.
(48) Ribeiro, D. V.; Abrantes, J. C. C. Application of electrochemical impedance spectroscopy (EIS) to monitor the corrosion of reinforced concrete: A new approach. *Constr. Build. Mater.* **2016**, *111*, 98–104. DOI: 10.1016/j.conbuildmat.2016.02.047.
(49) Tseng, Y.-C.; Hsieh, Y.-C.; Chin, N.-Y.; Huang, W.-Y.; Hou, S.-S.; Jan, J.-S. Synthesis, thermal properties and rheological behaviors of novel Poly(ethylene glycol) segmented Poly(arylene ether)s. *Polymer* **2020**, *196*. DOI: 10.1016/j.polymer.2020.122426.
(50) Alvarez-Vazquez, A.; Fernandez-Canteli, A.; Castillo, E.; Pelayo, F.; Muniz-Calvente, M.; Lamela, M. J. A Novel Approach to Describe the Time-Temperature Conversion among Relaxation Curves of Viscoelastic Materials. *Materials (Basel)* **2020**, *13* (8). DOI: 10.3390/ma13081809.
(51) Ricarte, R. G.; Shanbhag, S. A tutorial review of linear rheology for polymer chemists: basics and best practices for covalent adaptable networks. *Polym. Chem.* **2024**, *15* (9), 815–846. DOI: 10.1039/d3py01367g.
(52) Meng, F.; Saed, M. O.; Terentjev, E. M. Rheology of vitrimers. *Nat. Commun.* **2022**, *13* (1), 5753. DOI: 10.1038/s41467-022-33321-w.
(53) Bonin, H.; Delacroix, T.; Gras, E. Dioxazaborocanes: old adducts, new tricks. *Org. Biomol. Chem.* **2011**, *9*, 4714–4724. DOI: 10.1039/C1OB05330B.
(54) Zhou, Z.; Zou, R.; Liu, Z.; Zhang, P. Deciphering the role of tetrahydrofuran residue in the poly(ethylene oxide)/LiTFSI hybrid used for secondary battery electrolyte. *Giant* **2021**, *6*. DOI: 10.1016/j.giant.2021.100056.
(55) Liu, C.; Sacci, R. L.; Sahore, R.; Veith, G. M.; Dudney, N. J.; Chen, X. C. Polyacrylonitrile-based electrolytes: How processing and residual solvent affect ion transport and stability. *Journal of Power Sources* **2022**, *527*, 231165. DOI: 10.1016/j.jpowsour.2022.231165.
(56) Liu, C.-Y.; He, J.; Keunings, R.; Bailly, C. New linearized relation for the universal viscosity temperature behavior of polymer melts. *Macromolecules* **2006**, *39* (25), 8867–8869. DOI: 10.1021/ma061969w.
(57) Ciarella, S.; Sciortino, F.; Ellenbroek, W. G. Dynamics of Vitrimers: Defects as a Highway to Stress Relaxation. *Phys. Rev. Lett.* **2018**, *121* (5). DOI: 10.1103/PhysRevLett.121.058003.
(58) Ricarte, R. G.; Shanbhag, S. Unentangled Vitrimer Melts: Interplay between Chain Relaxation and Cross-link Exchange Controls Linear Rheology. *Macromolecules* **2021**, *54* (7), 3304–3320. DOI: 10.1021/acs.macromol.0c02530.
(59) Cho, N.; El-Zaatari, B.; Gokarn, R.; Van Zee, N.; Chapman, S.; Craig, S.; Kalow, J.; Richards, J. Evaluating the Linear Viscoelasticity of Vitrimers Using Start-up and Cessation Tests. *ChemRxiv* **2024**. DOI: 10.26434/chemrxiv-2023-hb4v1-v2.
(60) Quinteros-Sedano, A.; van Ruymbeke, E. Tuning the Viscoelastic Properties of Dioxazaborocane Vitrimers via Chemical Design of the Functional Groups. *Macromolecules* **2026**, *59* (3), 1781–1788. DOI: 10.1021/acs.macromol.5c03243.
(61) Lessard, J. J.; Stewart, K. A.; Sumerlin, B. S. Controlling Dynamics of Associative Networks through Primary Chain Length. *Macromolecules* **2022**, *55* (22), 10052–10061. DOI: 10.1021/acs.macromol.2c01909.
(62) Raji, I. O.; Dodo, O. J.; Saha, N. K.; Eisenhart, M.; Miller, K. M.; Whitfield, R.; Anastasaki, A.; Konkolewicz, D. Network Polymer Properties Engineered Through Polymer Backbone Dispersity and Structure. *Angew. Chem. Int. Ed.* **2024**, *63* (21), e202315200. DOI: 10.1002/anie.202315200.

(63) Lai, W. C.; Liu, L. J.; Tseng, S. J. Green Polymer Electrolytes Prepared by a Cost-Effective Approach. *Langmuir* **2024**, *40* (31), 16492–16501. DOI: 10.1021/acs.langmuir.4c01853.
(64) Hirano, T.; Saito, T.; Kurano, Y.; Miwa, Y.; Oshimura, M.; Ute, K. Dual role for alkali metal cations in enhancing the low-temperature radical polymerization of N,N-dimethylacrylamide. *Polym. Chem.* **2015**, *6* (11), 2054–2064. DOI: 10.1039/c4py01662a.
(65) Li, Z.; Fu, J.; Zhou, X.; Gui, S.; Wei, L.; Yang, H.; Li, H.; Guo, X. Ionic Conduction in Polymer-Based Solid Electrolytes. *Adv. Sci.* **2023**, *10* (10), e2201718. DOI: 10.1002/advs.202201718.
(66) Park, H.-J.; Lee, J.-H.; Lee, C.; Kim, T.-H.; Kang, M.-S. Thermally cured PEGMA-co-PEGDMA/PVAc electrolytes with synergistically enhanced mechanical and electrochemical properties for flexible electrochromic devices. *Electrochimica Acta* **2025**, *543*, 147634. DOI: 10.1016/j.electacta.2025.147634.
(67) Stolwijk, N. A.; Heddier, C.; Reschke, M.; Wiencierz, M.; Bokeloh, J.; Wilde, G. Salt-Concentration Dependence of the Glass Transition Temperature in PEO–NaI and PEO–LiTFSI Polymer Electrolytes. *Macromolecules* **2013**, *46* (21), 8580–8588. DOI: 10.1021/ma401686r.
(68) Dung, N. T. K.; Linh, N. T. D.; Tham, D. Q.; Chinh, N. T.; Tan, M. M.; Mai, T. T.; Trang, N. T. T.; Thanh, D. M.; Tung, N. Q.; Hoang, T.; et al. Effect Of Magnesium Perchlorate Content on the Mechanical, Thermal Stability, and Dielectric Properties of Plasticized PMMA/PVC-g-PMMA Electrolytes. *Adv. Polym. Technol.* **2020**, *2020*, 1–9. DOI: 10.1155/2020/2806242.
(69) Li, Y.; Xia, Z.-x.; Ma, L.-k.; He, Z.-c. Study on the thermal decomposition behavior and products of poly(vinyl alcohol) and its LiClO4 composites via Py/GC/MS. *J. Therm. Anal. Calorim.* **2021**, *147* (12), 7031–7042. DOI: 10.1007/s10973-021-11019-3.

Use of artificial intelligence

Artificial intelligence tools (ChatGPT, OpenAI) were used during the writing of this thesis to assist with language editing, sentence reformulation, and proofreading. All experimental procedures, data analyses, scientific discussions, and conclusions were performed and validated by the author.

7. Supplementary information

7.1. Dangling group synthesis

Synthesis of 2-(2-Phenyl-1,3,6,2-dioxazaborocan-6-yl)ethan-1-ol (DZA)

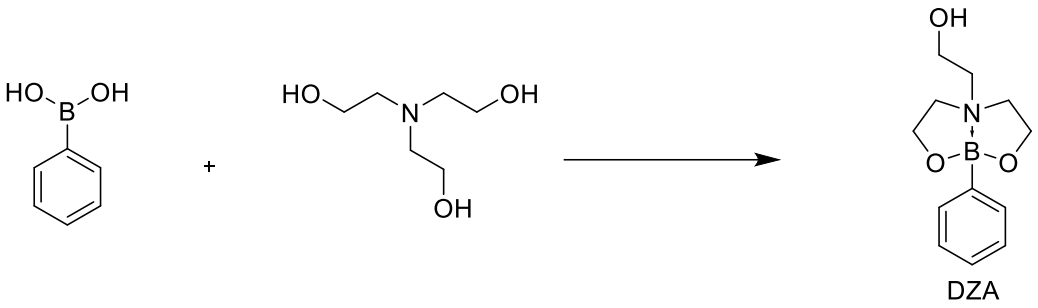

Benzene boronic acid (5g, 1eq) is dissolved in 160 mL of Et_2O in a 250 mL round bottom flask. A few drops of MeOH are added. The solution is stirred until a clear solution is obtained. The solution is refluxed. Triethanolamine (4.01g, 1eq) is dissolved in 2 mL of acetone and added dropwise to the solution. The solution is stirred and refluxed for 1h. Solvent is removed under reduced pressure. 100 mL of Et_2O is added. The solution is filtered, and the white solid is dried under vacuum. Mass of the solid = 6.94 g

Yield = 88%

^{1}H NMR (400 MHz, DMSO-D_6)

δ 7.54 – 7.43 (m, 2H), 7.20 (m, 3H), 4.75 (t, J = 5.2 Hz, 1H), 4.04 – 3.83 (m, 4H), 3.58 (q, J = 5.7 Hz, 2H), 3.19 (m, 4H), 3.10 (m, 4H), 2.27 (t, J = 5.9 Hz, 2H).

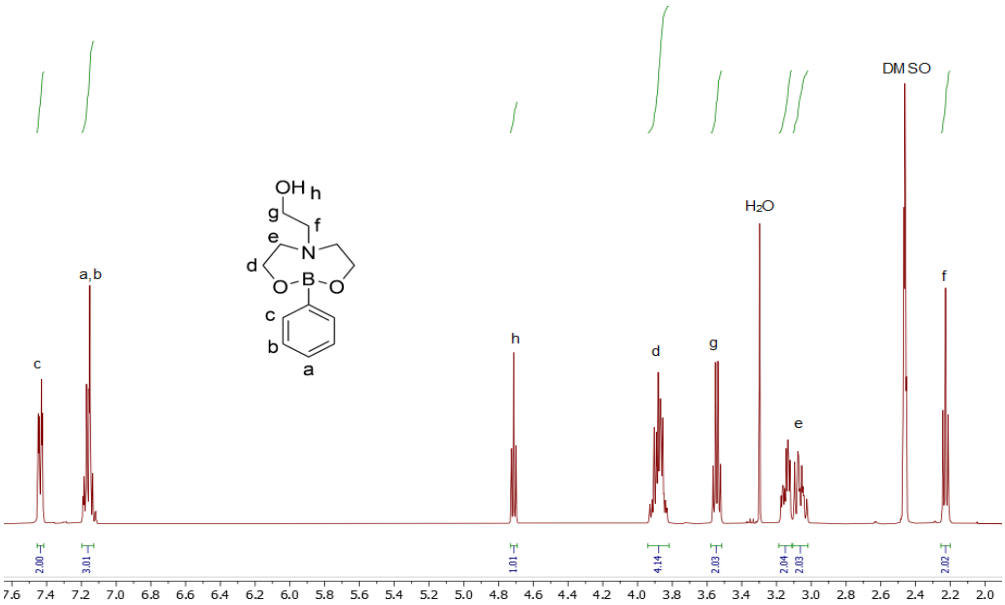

Figure 42 NMR of DZA

Synthesis of 2-(2-Phenyl-1,3,6,2-dioxazaborocan-6-yl)ethyl methacrylate (DBM)

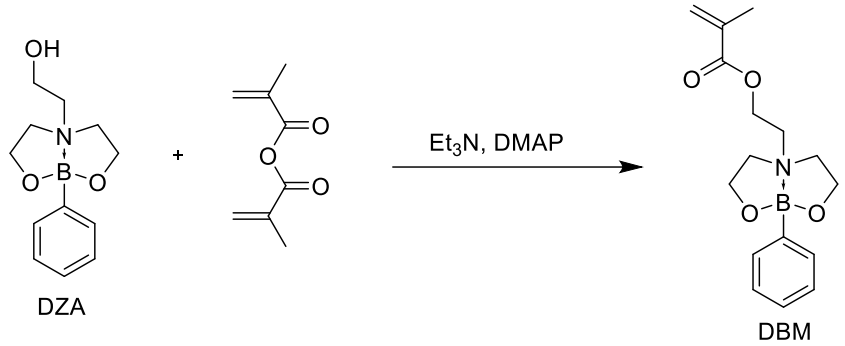

DZA (6.94g, 1eq), DMAP (36mg, 0.01eq) and Et_3N (4 mL, 1eq) are dissolved in 70 mL of acetonitrile in a 100 mL flask. The solution is stirred for 15 minutes. The reaction is kept under argon atmosphere. Methacrylate anhydride (5.3 mL, 1.2eq) is added dropwise. The reaction is stirred at rt overnight. 7 mL of MeOH are added. The solution is stirred at rt for 3h. Solvent is removed under reduced pressure. A white-yellow solid is obtained. The solid is added in 70 mL of $NaHCO_{3\,sat}$. The solution is extracted with 3x70 mL of AcOEt. Organic layers are combined and dried with $MgSO_4$. Solvent is evaporated, giving a white-yellow solid. The solid is suspended in 150 mL of Et_2O. The suspension is stirred for 15 min and then filtered. The solid is washed with Et_2O and dried under high vacuum. Mass of the solid = 7.099 g

Yield = 78%

^{1}H NMR (400 MHz, $CDCl_3$)

δ 7.68 – 7.59 (m, 2H), 7.35 – 7.26 (m, 3H), 6.06 (p, *J* = 1.0 Hz, 1H), 5.62 (p, *J* = 1.5 Hz, 1H), 4.35 – 4.28 (m, 2H), 4.19 (s, 4H), 3.13 (t, *J* = 6.1 Hz, 4H), 2.77 – 2.57 (m, 2H), 1.92 (dd, *J* = 1.6, 1.0 Hz, 3H).

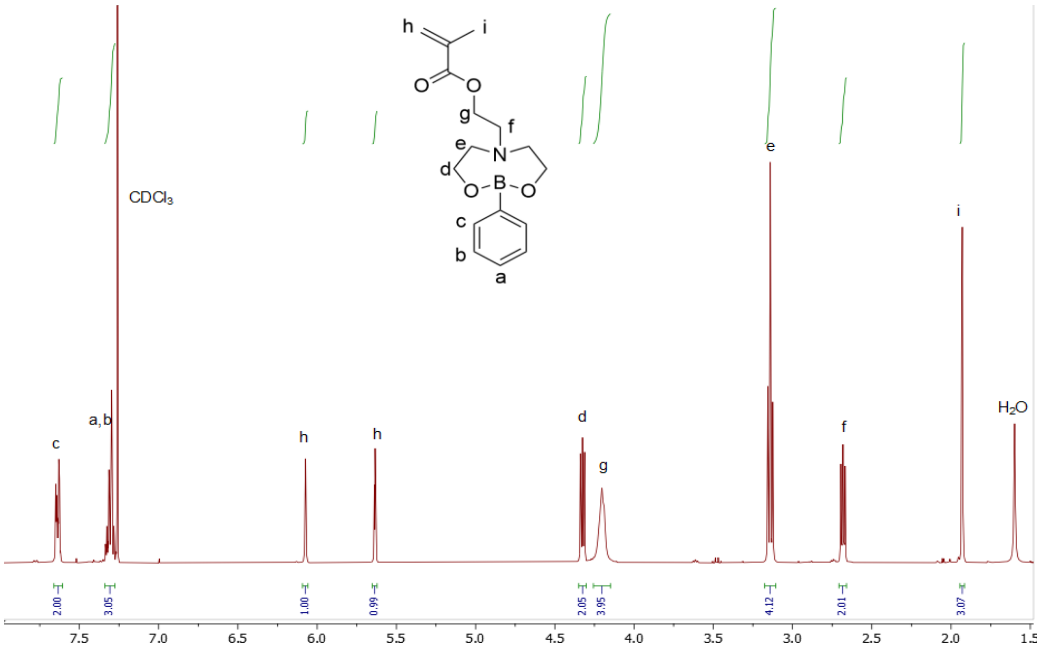

Figure 43 NMR of dangling group (DBM)

7.2. Crosslinker synthesis

Synthesis of (4-(4-methyl-1,3,2-dioxaborolan-2-yl)phenyl)methanol (MDB)

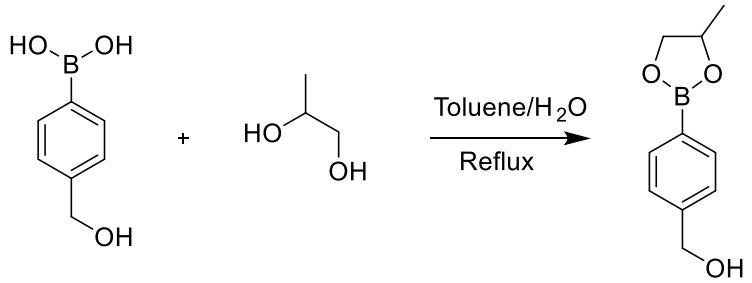

MDB

(4-(hydroxymethyl)phenyl)boronic acid (5g, 1eq) and propane-1,2-diol (2.5g, 1eq) are added in a 100 mL flask with 50 mL of toluene and 1 mL of water in a Dean-Stark apparatus. 8 mL of toluene is added in the apparatus. The flask is heated at 120°C for 3h. Solvent is evaporated, giving a yellow oil. Mass = 6.27 g

Yield = 98%

^{1}H NMR (400 MHz, $CDCl_3$)

δ 7.81 (d, *J* = 8.0 Hz, 2H), 7.39 (d, *J* = 8.2, 2H), 4.73 (d, *J* = 6.0 Hz, 3H), 4.46 (dd, *J* = 8.8, 7.7 Hz, 1H), 3.90 (dd, *J* = 8.9, 7.2 Hz, 1H), 1.68 (t, *J* = 6.0 Hz, 1H), 1.42 (d, *J* = 6.2 Hz, 3H).

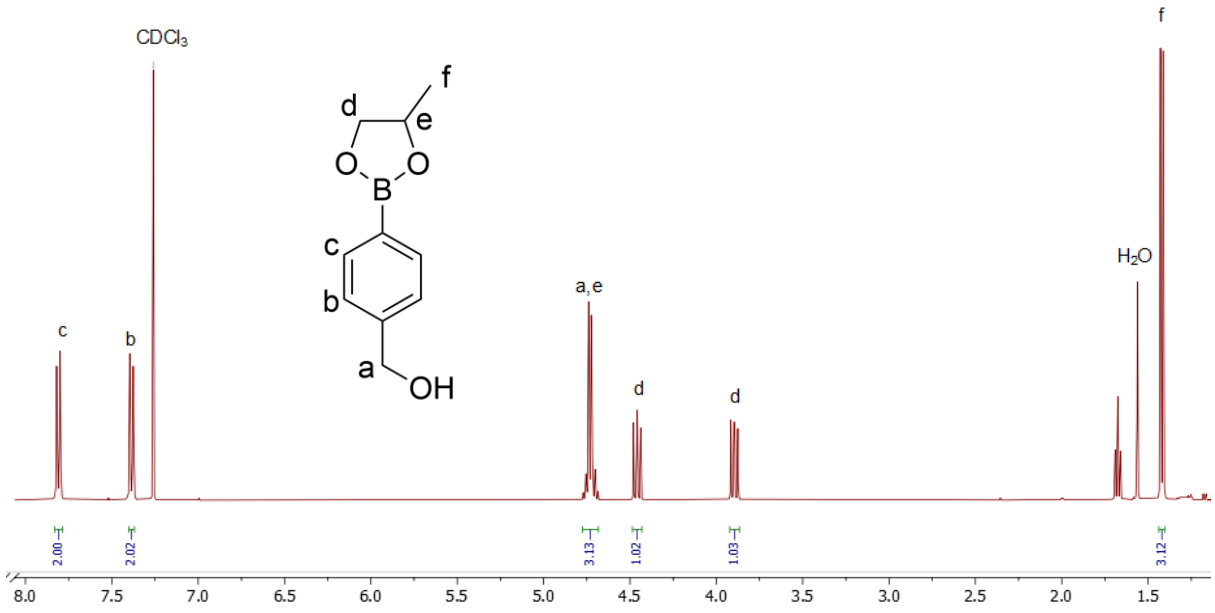

Figure 44 NMR of MDB

Synthesis of (4-((methacryloyloxy)methyl)phenyl)boronic acid (BAM)

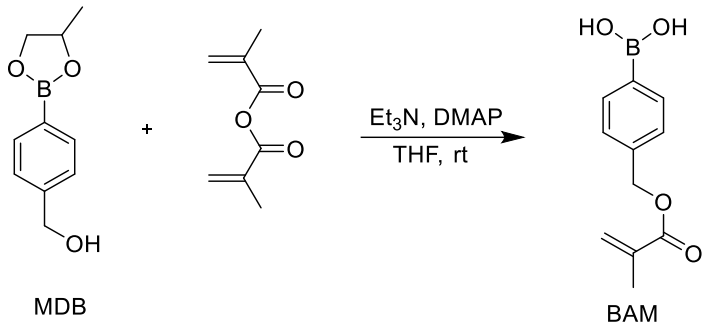

MDB (6.27g, 1eq) is dissolved in 45 mL of THF in a 100 mL flask. Et_3N (5.7 mL, 1.2eq) and DMAP (43 mg, 0.01eq) are added and the solution is stirred for 15 minutes. Argon atmosphere is introduced. Methacrylate anhydride (6.3 mL, 1.2eq) is added dropwise. The solution is stirred for 24h at rt. 6.5 mL of MeOH are added. The solution is stirred for 4h. The solution is added dropwise to a solution of HCl 0.05M (600 mL). A white solid precipitated. The suspension is filtered. The white solid is washed with water and dried under high vacuum. Mass of the solid = 6.964 g

Yield = 78%

^{1}H NMR (400 MHz, DMSO-D_6)

δ 8.06 (s, 2H), 7.78 (d, J = 8.0 Hz, 2H), 7.33 (d, J = 8.0 Hz, 2H), 6.07 (dq, J = 1.9, 1.0 Hz, 1H), 5.71 (p, J = 1.6 Hz, 1H), 5.17 (s, 2H), 1.90 (dd, J = 1.6, 1.0 Hz, 3H).

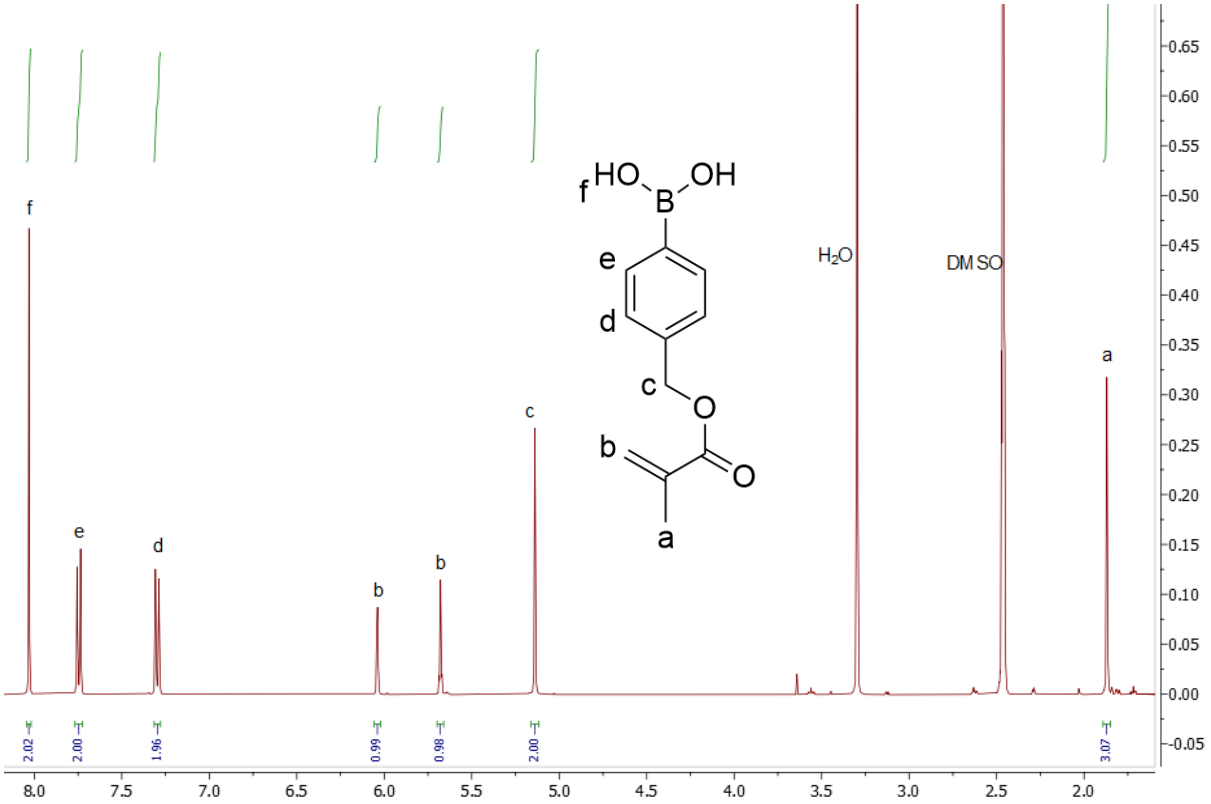

Figure 45 NMR of BAM

Synthesis of 4-(1-(2-hydroxyethyl)-1,5-azaborocan-5-yl)benzyl methacrylate (HDZM)

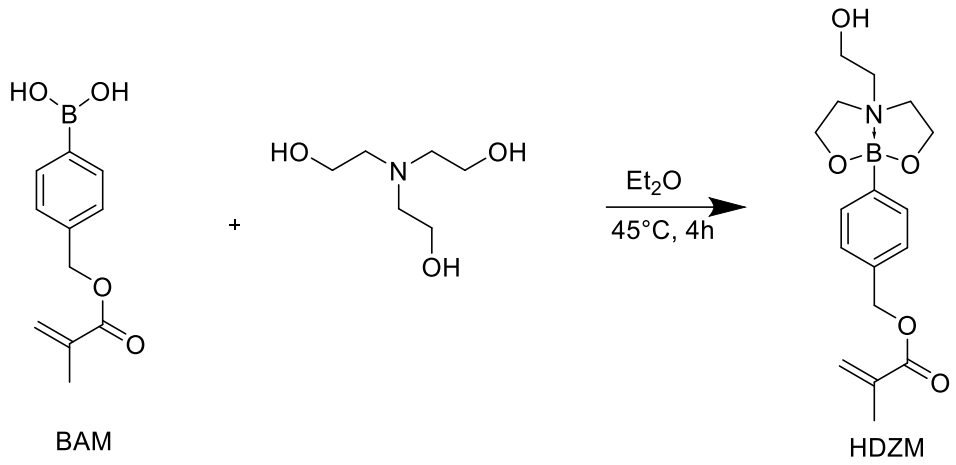

BAM (3.456g, 1eq) is suspended in 70 mL of Et_2O. Triethanolamine (2.134g, 1.05eq) is dissolved in 0.5 mL of acetone. This solution is added to the suspension of BAM. 0.5 mL of MeOH are added. The solution is stirred and refluxed at 45°C for 4h. The solution is cooled to rt and filtered. The white solid is dried under high vacuum. Mass = 3.61 g

Yield = 80%

^{1}H NMR (400 MHz, DMSO-D_6) δ 7.48 (d, J = 7.9 Hz, 2H), 7.23 (d, J = 8.1 Hz, 2H), 6.06 (dq, J = 1.9, 1.0 Hz, 1H), 5.70 (p, J = 1.6 Hz, 1H), 5.14 (s, 2H), 4.75 (t, J = 5.3 Hz, 1H), 3.99 – 3.84 (m, 4H), 3.59 (q, J = 5.7 Hz, 2H), 3.24 – 3.05 (m, 4H), 2.27 (t, J = 5.9 Hz, 2H), 1.90 (dd, J = 1.6, 1.0 Hz, 3H).

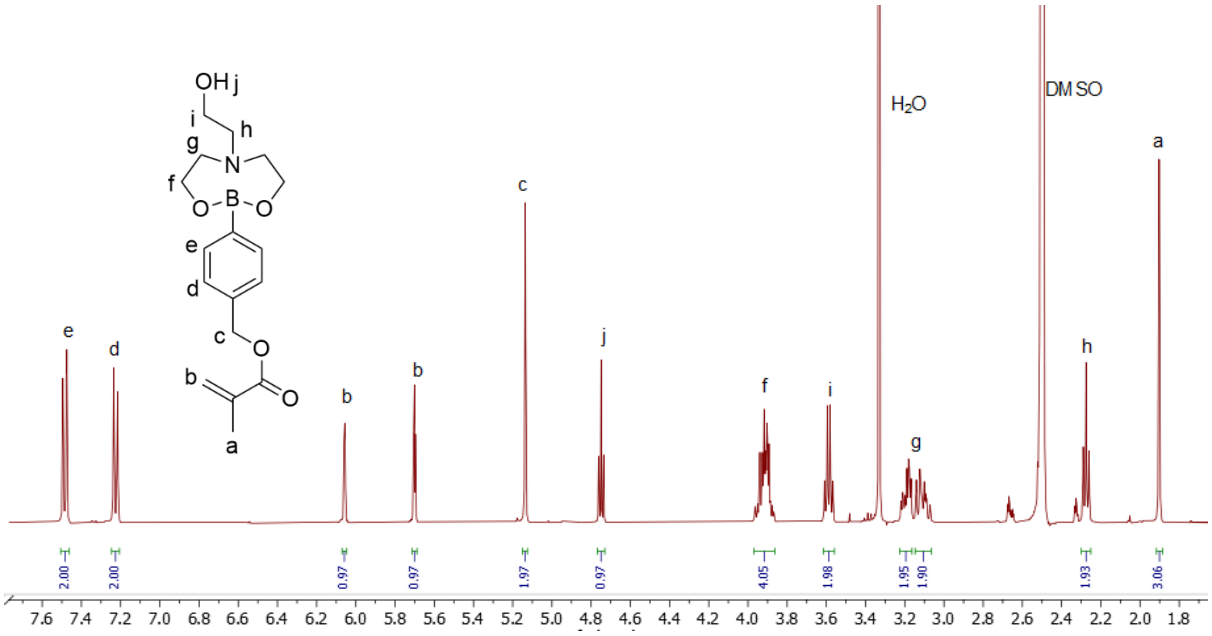

Figure 46 NMR of HDZM

Synthesis of 4-(6-(2-(methacryloyloxy)ethyl)-1,3,6,2-dioxazaborocan-2-yl)benzyl methacrylate (MDZM)

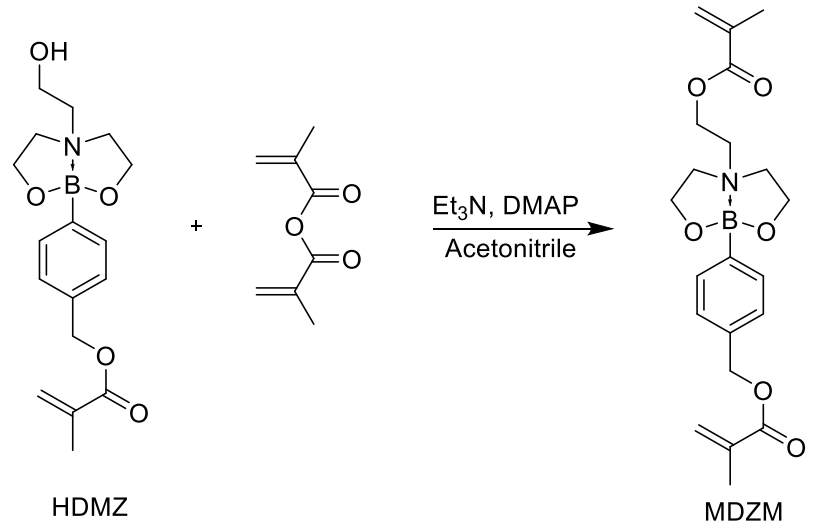

HDZM (3.61g, 1eq), DMAP (13.4mg, 0.01eq) and Et_3N (1.5 mL, 1eq) are dissolved in a 100 mL flask with 35 mL of acetonitrile. 5 mL of DMF are added. The solution is heated to 30°C. Argon atmosphere is introduced. Methacrylate anhydride is added dropwise. The solution is stirred overnight. The solution turned from a white suspension to a yellow solution. 5 mL of MeOH are added. The solution is stirred for 3h. The solution is filtered and concentrated under reduced pressure, giving a yellow liquid. 50 mL of $NaHCO_3$ is added. The solution is extracted with 3x60 mL of AcOEt. The organic layers are dried with $MgSO_4$, filtered and concentrated under reduced pressure, giving a white powder. The powder is suspended in 100 mL of Et_2O and stirred for 15 minutes. The suspension is filtered, and a white powder is obtained.

Mass = 2.498 g

Yield = 55%

^{1}H NMR (400 MHz, $CDCl_3$) δ 7.64 (d, *J* = 8.0 Hz, 2H), 7.31 (d, *J* = 7.9 Hz, 2H), 6.15 (dd, *J* = 1.7, 0.9 Hz, 1H), 6.08 (t, *J* = 1.2 Hz, 1H), 5.64 (p, *J* = 1.5 Hz, 1H), 5.57 (p, *J* = 1.6 Hz, 1H), 5.19 (s, 2H), 4.37 – 4.30 (m, 2H), 4.20 (s, 4H), 3.14 (t, *J* = 6.1 Hz, 4H), 2.68 (dd, *J* = 5.8, 4.8 Hz, 2H), 1.97 (dd, *J* = 1.6, 1.0 Hz, 3H), 1.93 (dd, *J* = 1.7, 1.0 Hz, 3H).

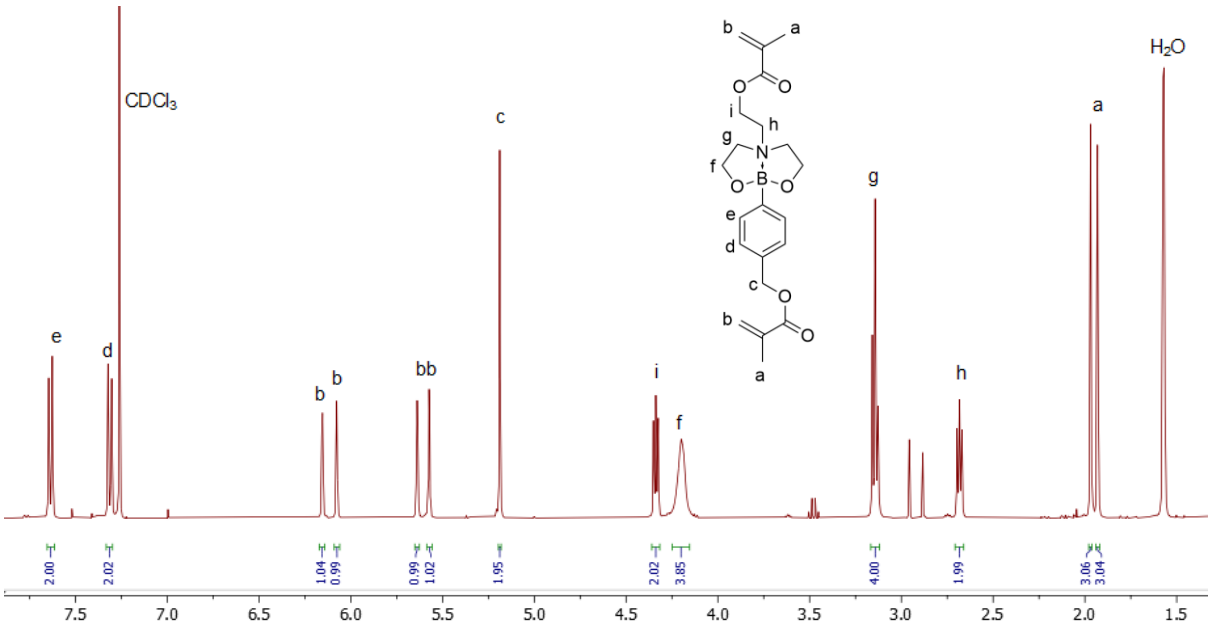

Figure 47 NMR of the crosslinker (MDZM)

UNIVERSITÉ CATHOLIQUE DE LOUVAIN
Faculté des sciences
Place des sciences, 2 bte L6.06.01, 1348 Louvain-la-Neuve, Belgique | **www.uclouvain.be/sc**